Università degli Studi di Ferrara

DOTTORATO DI RICERCA IN
"FISICA"

CICLO XXIV

COORDINATORE Prof. Filippo Frontera

A NUMERICAL APPROACH TO OHMIC LOSSES ASSESSMENT IN CONCENTRATING PHOTOVOLTAIC SYSTEMS

Settore Scientifico Disciplinare FIS/01

Dottorando
Dott. Pasquini Matteo

_____
(firma)

Tutore
Prof. Guidi Vincenzo

_____
(firma)

Anni 2009/2011

ACKNOLEDGEMENTS

I would like to acknowledge my supervisors, Dr. Donato Vincenzi and Prof. Vincenzo Guidi, for providing me the guidance to carry through this research.

I am also grateful to Prof. Giuliano Martinelli for the trust he put in me three years ago, when I joined this research group.

I wish to express my sincere gratitude to Dr. Stefano Baricordi, for his precious advices in many situations.

I would like to thank my colleague Dr. Federico Gualdi; he shared with me an important part of our research activity. Our challenging discussions helped me a lot in gaining a deeper insight into our field of research.

I would also like to thank my referees, Dr. Gianlucà Timò and Prof. Alfonso Damiano.

Finally, I must acknowledge my parents for their constant support.

This research activity has been funded by EU project Apollon (grant agreement n. 213514), FIRB national project Fotoenergia (RBIP06N57B), Sardinia regional law 7/2007 (CUP F71J09000270002), STMicroelectronics and Angelantoni Industries.

Table of Contents

Table of Figures

List of Tables

1 INTRODUCTION TO CONCENTRATING PHOTOVOLTAIC (CPV) SYSTEMS

The main problem connected to the use of solar electricity is that it is too expensive. The traditional single-crystal silicon cells require expensive purification limiting harmful impurities to less than 10ppb and expensive crystal growth and cell fabrication steps. Silicon cell efficiencies as high as 23% are achieved when these steps are taken. Unfortunately, these silicon cells and modules and the resultant electricity are then expensive. Meanwhile, when thin-film cells are used with less expensive amorphous or small grain-size materials, the result is low conversion efficiency. While the thin-film modules are then less expensive, the larger installed systems and resultant electricity are still expensive.

The problem is that both low-cost solar collectors and high-efficiency solar converters are needed. Concentrating the sunlight onto efficient single-crystal cells can potentially produce lower-cost electricity by providing a second component. Low-cost plastic or glass lenses or sheet metal mirrors can collect the sunlight and concentrate it onto the expensive high-efficiency single-crystal cells, thereby diluting their cost.

The concentration approach was sponsored for the first time by Sandia National Laboratories. Figure 1.1 shows an approach sponsored by Martin Marietta [3], constituted by an array of point-focus Fresnel lenses focusing sunlight 50 times on silicon cells and Figure 1.2 shows an ENTECH [4] linear arched plastic Fresnel lens focusing sunlight 20 times onto silicon cells. Both systems used aluminum finned extrusions for cell cooling, and both of these pioneering systems operated successfully for several years.

The output power from the point-focus module design shown in Figure 1.1 can be easily improved by replacing the silicon cell with a more efficient multijunction cell. The idea was first developed by Varian [5] in the 1980s. Varian suggested increasing the concentration ratio by using a cell package with a secondary concentrator element. This solution is now implemented in many types of highly-concentrating photovoltaic systems (HCPV).

Under concentrated light, multijunction solar cells achieve efficiencies of over 40%. However, their area-related costs are close to two magnitudes higher than those of bulk silicon solar cells, which clearly dominate the solar cell market today. For terrestrial applications, the high-efficiency multijunction solar cells, usually triple-junction solar cells are used in combination with cheap optics, which collect the sunlight over an area that is several hundred times larger than the solar cell area and focus it on the solar cell. There are four fundamental choices for concentrating optics: refractive (transparent lenses), reflective (mirrored) optical elements, dispersive (holographic, grating and

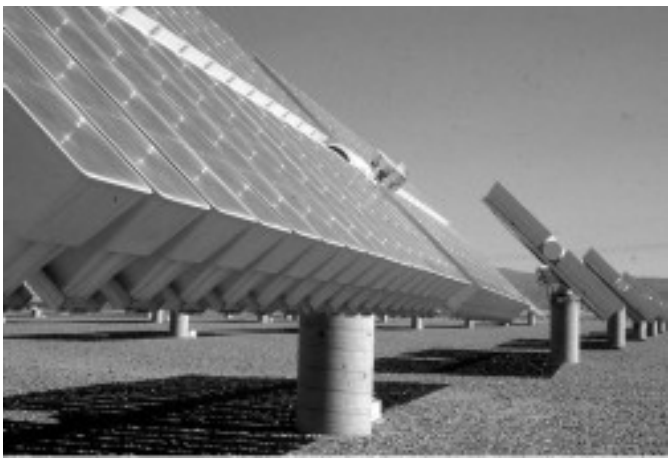

Figure 1.1 The 350-kWp SOLARAS project power plant built and deployed in Saudi Arabia by Martin Marietta using Sandia Labs technology [1].

Figure 1.2 ENTECH mid-concentration photovoltaic module design using arched linear Fresnel lens [2]

prismatic elements) and fluorescent (panels). Of these, refractive and reflective designs are the most interesting for commercial high-concentration large-scale systems. Several configurations and variations are possible for each of these.

1.1 REFLECTIVE CONCENTRATORS

In a reflective concentrator a light ray incident on a smooth mirror surface is reflected as shown in Figure 1.3. As can be seen from the figure, the light ray incident on the surface at angle θ to the surface normal reflects at angle θ'. According to the law of reflection, the angle of reflection is equal to the angle of incidence, θ' = θ.

Figure 1.4 shows the concentration of the sunlight by a curved mirror surface with radius of curvature R. As can be seen from the figure, the incident rays are concentrated at focal point F. The distance of

the focal point from the center of the mirror surface can be calculated from the mirror equation.

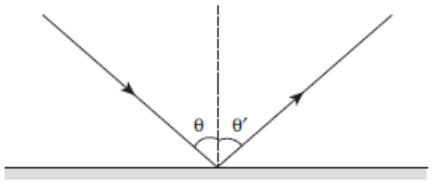

Figure 16.1. Schematic representation of reflection.

Figure 1.3 Schematic representation of reflection.

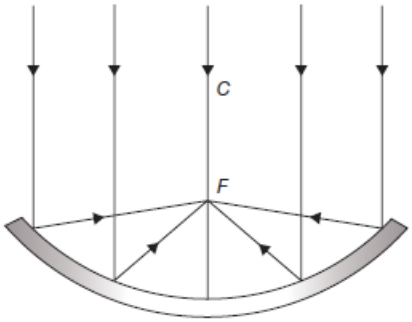

Figure 1.4 Reflective concentration from a curved surface.

The mirror equation is given as

$$\frac{1}{p}+\frac{1}{q}=\frac{2}{R} \tag{1.1}$$

where p is the distance of the light source from the center of the mirror, q is the distance of the concentrated image from the center of the mirror, and R is the radius of curvature of the mirrored surface.

In a concentrated solar system, the distance from the source of light (the Sun) is much greater than the radius of mirror R. It can be said that p is infinity; therefore, $1/p \approx 0$. This simplifies the mirror equation to

$$\frac{1}{q}=\frac{2}{R} \tag{1.2}$$

Now, the image distance or focal length $f = q = {}^{R}/_{2}$.

Actually, the above equation is an approximation. The mirror surface is really a parabola described by the equation

$$Y = x^2/4f \tag{1.3}$$

The equation for a circle is given by

$$(y-R)^2 + x^2 = R^2 \quad \text{or} \quad 2yR = x^2 + y^2 \tag{1.4}$$

This reduces to $y = x^2/2R$ when $y \ll R$ and x and $f = R/2$. Then, the sunlight incident on a curved mirror surface is concentrated at its focal point, which is equal to half of its radius of curvature R.

1.2 REFRACTVE CONCENTRATORS

In a refractive concentrator light traveling through a transparent medium is bent at the boundary of that medium leading to another medium as shown in Figure 1.5. This is called refraction. As can be seen from the figure, the light ray traveling through the air enters the glass at angle θ_1 (angle of incidence) to the surface normal and is refracted at the top surface to angle θ_2 (angle of refraction). The relation between the angle of incidence and the angle of refraction is given as

$$\frac{sin\theta_2}{sin\theta_1} = \frac{v_2}{v_1} \tag{1.5}$$

where v_1 and v_2 are the speed of light in air and glass, respectively.

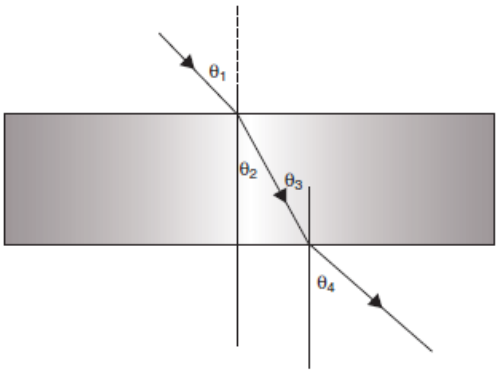

Figure 1.5 Refraction of a light ray passing through a transparent material.

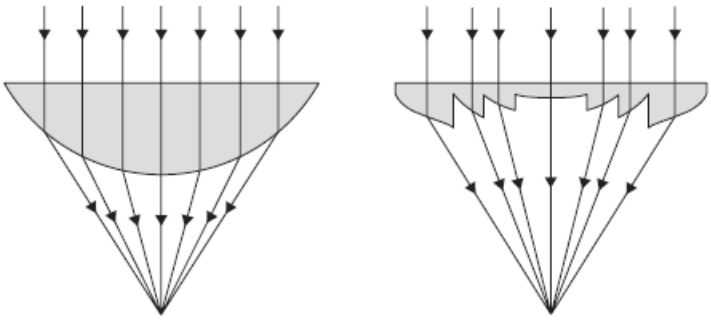

Figure 1.6 Refraction of light rays passing through a plano-convex lens (left) and a Fresnel lens (right).

Refractive index n, a property of any material, can be used to find v for any material. Refractive index n is the ratio of speed of light in vacuum c, and the speed of light in a medium v.

In a refractive concentrator, sunlight is concentrated as shown in Figure 1.6. As can be seen from the figure, the light traveling through a plano-convex lens is concentrated at its focal point. The focal length in this case can be calculated approximately from the basic lens equations as follows:

$$\frac{n_1}{p} + \frac{n_2}{q} = \frac{n_2 - n_1}{R} \tag{1.6}$$

where n_1 and n_2 are the refractive indexes of air and lens material, respectively. As discussed earlier, p, the light source (the Sun), is at an infinite distance, and $n_1 = 1$ for air. The equation simplifies to

$$\frac{n_2}{q} = \frac{n_2 - n_1}{R} \tag{1.7}$$

Now, the image distance or focal length $f = q = \frac{n}{1-n}R$, where $n = n_2$ is the refractive index of the lens material.

As noted above, the refraction occurs only at the surface of a lens. Taking advantage of this fact, a thin lens (called a Fresnel lens) was developed and serves the same purpose as a thick lens. Fresnel lenses are being used in many applications as a less expensive and weight-reducing alternative to thick lenses. Fresnel lenses made from acrylic polymers for nonimaging applications such as CPV systems can further reduce the cost of a refractive concentrator system. Concentration of sunlight through a Fresnel lens is shown in the right side of Figure 1.6.

1.3 FRESNEL LENS

Fresnel lenses are the principal choice for refractive systems due to the weight, low material content and low internal absorption compared to spherical or aplanatic lenses. A top view of a typical Fresnel lens is showed in Figure 1.7.

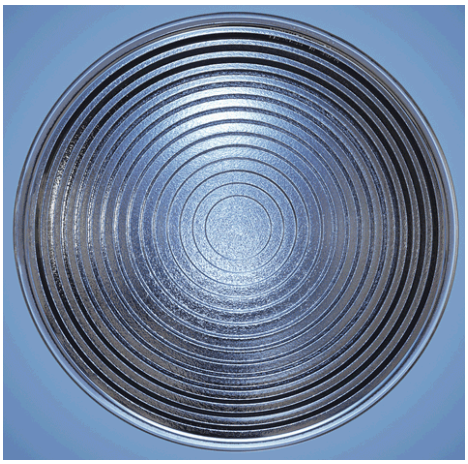

Figure 1.7 Top view of a typical Fresnel lens

Plastic materials are the choice for solar concentrators due to their low cost and the ready availability of mass-production molding or stamping technologies. Silicone molded on glass substrates to form the Fresnel lens is also an emerging approach. Fresnel lenses, however, suffer from chromatic aberrations, which become more pronounced for the larger aperture lenses needed at higher concentrations. Chromatic aberrations create a local mismatch between the currents of the subcells of a triple-junction solar cell pulling down the efficiency.

Basically, a Fresnel lens has optical properties similar to conventional lenses; however, they have lower material usages and therefore lower intrinsic cost. This is due to the fact that a Fresnel lens is obtained by breaking a conventional lens into a set of concentric segments. Figure 1.8 shows a sketch of a conventional and planar Fresnel lens with the same size and focal distance. As a result of the faceted structure, a Fresnel lens offers an additional dimension in design space. The angle of each facet can be varied in order to decrease spherical aberration or the homogeneity of the light distribution in the focal spot [6].

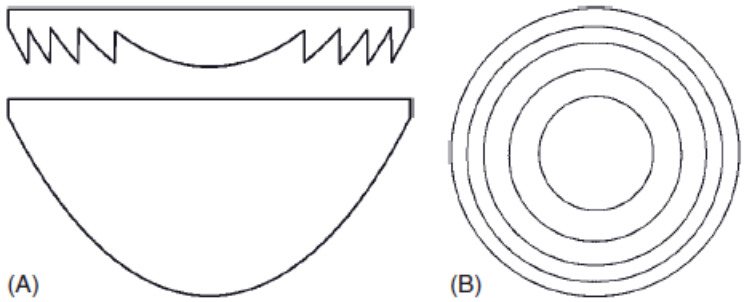

Figure 1.8 (A) A sketch of the cross section of a conventional lens and above a corresponding Fresnel lens with the same size and focal length. (B) The concentric segments of the Fresnel lens are sketched in a plan view.

The relatively low manufacturing and material costs makes Fresnel lenses one of the cheapest available concentrating optics. This is the reason why they have been used from the beginning of PV concentrator development and are the most widely used optical system in CPV today.

In comparison to a massive lens, however, a Fresnel lens has to pay some additional efficiency losses. A Fresnel lens consists of many prismatic facets that refract the light onto the focal spot. Ideally each facet has a sharp peak and valley, and the groove wall is oriented parallel to the sunrays. However, the real structure of a Fresnel lens shows deviations, for example, due to the manufacturing process, which lead to losses. These losses are sketched in Figure 1.9a and are summarized in the following points:

1. The light impinging on rounded facet peaks or valleys is not concentrated and lost. In order to minimize these losses, accurate manufacturing technique and large facet spacing relative to the total size of the lens are mandatory.
2. Beside the active side of a facet that refracts direct light onto the solar cell, every facet has a

groove wall. In practice, this wall must be slightly tilted in order to provide a reliable de-molding during the manufacturing. This tilting causes some rays to be misguided.

3. For simplicity and manufacturing reasons, the active side of a facet does not have the most ideal bent shape but is approximated linearly. The resulting losses are negligible when the facet spacing is small compared to the total size of the lens.

However, when closed facet spacing is used, diffraction effects can decrease the optical efficiency of the Fresnel lens. These losses can become significant at facet diameters around 100 μm.

In addition to the loss mechanisms specific to the Fresnel lens, the typical optical losses for lenses like aberration, absorption, scattering at surface imperfections and surface reflection must be considered. Reflection losses at surfaces can be reduced with appropriate antireflection coatings; however, these coatings increase the cost of the Fresnel lens.

For imaging optical elements, the maximum achievable concentration is determined by the ratio of focal length and diameter of the optics; this follows from the ètendue. A flat Fresnel lens designed for high concentrations must refract light rays impinging the corner of the lens in a steep angle. This increases the chromatic aberration of the lens, and in extreme cases rays from the lens corners are lost due to total internal reflection. Thus, the maximal concentration of a Fresnel lens is limited by the chromatic aberration and reflection losses. The exact limit depends on a number of parameters (e.g., the refractive index). Typically, the maximum concentration limit is quoted to be about 500X for flat Fresnel lenses [7]. For geometric concentrations < 500X, the optical efficiency of a Fresnel lens usually ranges between 70% and 90%, depending on the quality of the manufacturing process.

An additional design parameter for a Fresnel lens is the surface curvature. In Fresnel dome lenses, the light rays are refracted at two surfaces, as is shown in Figure 1.9B.

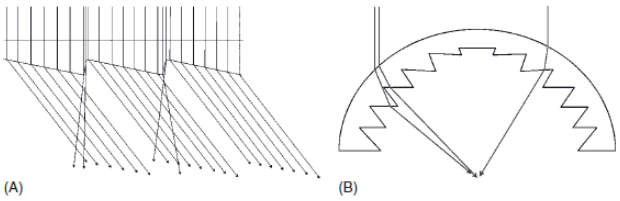

Figure 1.9 (A) A typical loss mechanism of a flat Fresnel lens are sketched. In practice, the active side of each facet refracts incoming light rays toward the focus. Ideally, the shape of a facet is hyperbolic; however, in practice, it is often approximated linearly. Typically, light rays are misguided at peaks and valleys of the facets, which cause a decrease of the optical efficiency. Furthermore, the groove wall of each facet is typically slightly tilted in order to provide a reliable de-molding during the manufacturing process. This also has a negative impact on the optical efficiency of the Fresnel lens. (B) A dome Fresnel lens is sketched. As a result of the bowed surface structure, the light rays are refracted at two surfaces. Thus, direct light rays can be refracted in a relative steep angle at comparable low reflection and aberration losses. Furthermore, when direct light is impinging perpendicularly on the dome Fresnel lens, the grooved side of the facets and the peaks does not impact the light rays. Consequently, these parts of the domed Fresnel lens do not decrease the optical efficiency .

Consequently, the required angles of refraction are smaller for a Fresnel dome lens than for a flat Fresnel lens with the same size and focal length. Using a Fresnel dome lens, short focal lengths and comparatively low chromatic aberration can be realized. This, in turn, allows higher concentration ratios to be achieved as compared with flat Fresnel lenses.

A problem connected to the use of Fresnel lenses is that the spatial distribution of light at the focal spot is inhomogeneous. This can have a negative impact on the solar cell performance, as we will see in this thesis. In Figure 1.10 the measured spatial intensity distribution in the focus of a flat Fresnel lens with a lens aperture of 16 cm^2 is shown [8]. The central peak intensity decays to 10% at a distance of 0.6 mm from the center. This Fresnel lens is used together with a circular 2 mm cell, leading to a geometric concentration ratio of 500X. However, the real central peak intensity can reach concentration ratios above 2500X.

For these reasons, in order to compensate for these disadvantages, secondary optical elements are often applied in CPV modules with flat Fresnel lenses.

1.4 SECONDARY OPTICS FOR FRESNEL LENSES

A second optic provides a second chance to influence the path of the light rays. Usually, secondary optical elements are located close above the solar cell. The task of a secondary can be manifold. In particular, it can increase the concentration ratio and/or the angular transmission. If required, it can homogenize the spatial distribution of concentrated sunlight on the solar cell. A simple secondary approach for Fresnel lens concentrators was already used in a 200X Fresnel lens concentrator of the Sandia National Laboratories [9]. There, a highly reflective cone was located around the cell in order to catch spilled sunrays. Also in more recent developments at Fraunhofer ISE, the potential of a reflective cone secondary was investigated. In particular, these elements are manufactured from Al, which are equipped with metallic reflector layers [10]. The reflective cone secondary has been designed that only misguided light rays from the primary optics are concerned. Thus, this type of secondary is expected to have only a positive impact on the optical performance of the concentrator. Figure 1.11A presents the short-circuit current of two FLATCON test modules versus the angle of misalignment. Each of the two modules consists of six 4.15 mm^2 triple-junction solar cells which are placed in the foci of 40 × 40 mm^2 Fresnel lenses. One of the modules was, in addition, equipped with reflective secondary optics. Obviously, the gain in optical performance increases with higher angles of misalignment.

It is important to note that the solar disk has an angular size of about ±0.25°. The direct irradiation incoming within an opening angle larger than ±0.25° is called circumsolar irradiation, and the intensity is typically 5-20% of the direct sunlight [11] (circumsolar ratio or CSR), depending on

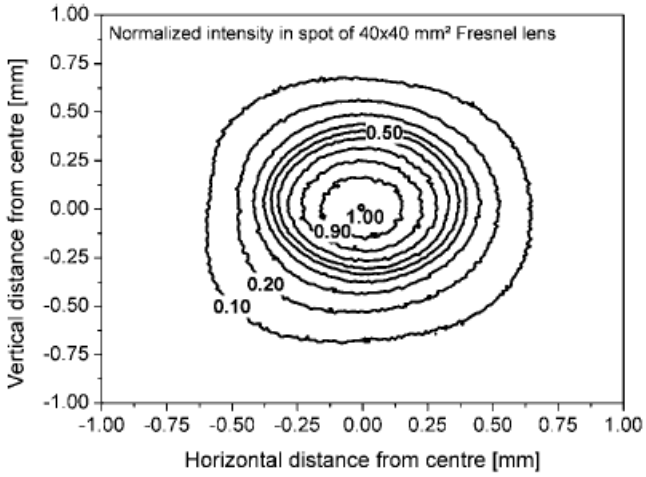

Figure 1.10 A profile of the measured intensity in the spot of a 40 × 40 mm^2 Fresnel lens is shown. The measurement was carried out with monochromatic light at a setup developed at the Fraunhofer ISE [18].

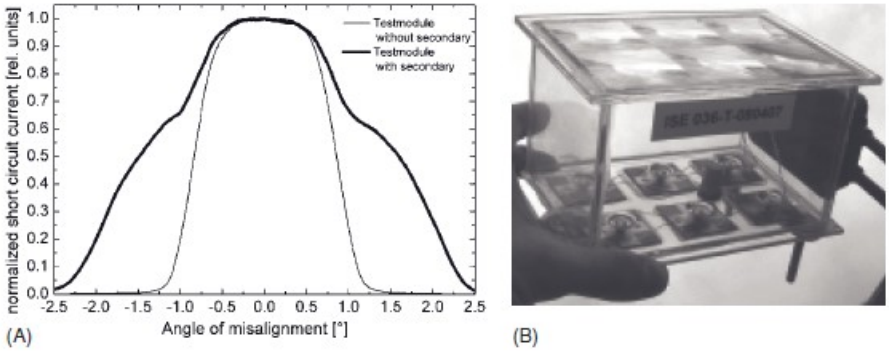

Figure 1.11 (A) The angular transmission of two test modules with six Fresnel lenses (40 × 40 mm^2) and six solar cells (4.15 mm^2) is shown. In principle, both modules have the same components, except for an additionally mounted reflective secondary optic on one of the modules. The short-circuit current of the modules was measured outdoors under a varying sun vector angle. (B) A photo of a test module equipped with reflective secondary elements is shown.

atmospheric conditions. As can be seen from Figure 1.7A the CSR is poorly utilized by the Fresnel lens. Obviously, the reflective cone secondary offsets this disadvantage and the direct sunlight and the CSR can be utilized more efficiently.

For small angles of misalignment, the gain in optical transmission is relatively small and the secondary does not avoid a significant drop in optical transmission at a misalignment angle of 1°. This is a result of light reflection losses in the secondary.

Alternatively to simple cone reflectors, secondary optics, which use total internal reflection, can be applied. These are dielectric optical elements that have to be placed in the concentrated beam of the Fresnel lens. At the entrance aperture, the light is refracted into the secondary and is total internally reflected at the side walls of the secondary. Finally, the light leaves the secondary at the exit aperture.

Usually, the exit aperture and the solar cell are connected with an optical coupling medium in order to decrease reflection losses at the surfaces. Depending on the surface quality, total internal values of up to 100% can be achieved and the angular transmission of the Fresnel lens concentrator can be increased significantly. The refraction of light at the entrance aperture provides an additional degree of freedom in optical design. However, losses occur due to surface reflection and absorption in the secondary dielectric material.

Typical representative of total internal reflection secondaries are Compound Parabolic Concentrators (CPCs) and light rods. The latter usually has a conical shape with an entrance aperture larger than the exit aperture and can be used for homogenizing purposes.

A CPC is a nonimaging concentrating optical element that can allow high concentration ratio and high angular transmission values [12]. The side of a CPC is shaped parabolically and the entrance aperture is larger than the exit aperture, as is shown in Figure 1.12. Beneath a Fresnel lens, it can be used to increase the concentration and the angular acceptance of the concentrator. Ray-tracing simulations show that with a Fresnel lens and a CPC secondary, a concentration of 1000X and an acceptance angle of 1° can be achieved.

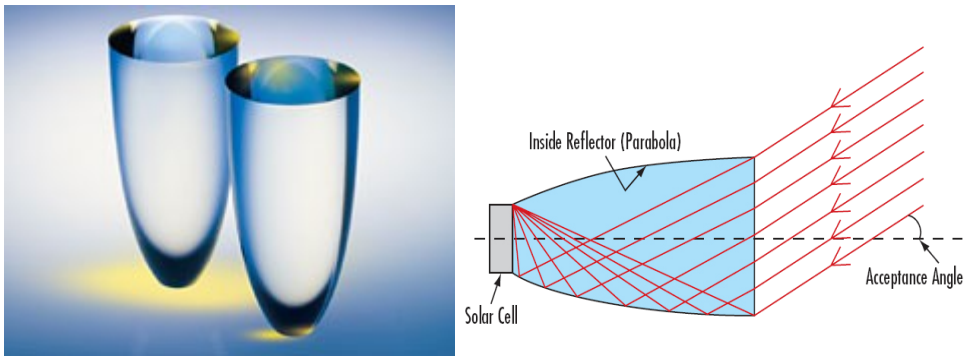

Figure 1.12 A typical CPC and its section view

Furthermore, already in the mid 1980s, the Varian Research Center used a conical glass element with a convex-shaped entrance aperture as secondary element. This provided a second refraction of the beam focused primarily by a Fresnel lens. In addition, a total internal reflection guided the light rays on the cell. Due to this advanced secondary concept, a Fresnel lens concentrator with a concentration factor of almost 1000X and an outstanding angular acceptance of more than 1° could be realized [13]. The modules used GaAs single-junction concentrator solar cells, achieving an efficiency of about 28% [14]. Furthermore, a module efficiency of 22.3% was reported, which was achieved with a Fresnel lens concentrator equipped with 12 GaAs solar cells and without applying a temperature correction [15]. Considering this concentrator would have been equipped with today's triple-junction solar cells instead of the single-junction cells, one could expect a module operating efficiency of about 30%.

1.5 CENTRAL RECEIVER REFLECTORS

Central receiver reflectors are another popular approach to concentrator systems [16]. These systems employ a single, large reflective dish, constructed from multiple mirror segments, to focus the sunlight on a dense array of solar cells. Central receiver optical systems have high efficiencies but very narrow acceptance angles and therefore require accurate tracking systems. Furthermore, the solar cells must be actively cooled, since the back-side area, which is to say the area available to conduct heat passively to the environment, is small compared to the entrance aperture. Active cooling consumes system power and adds an additional level of complexity to system construction and maintenance.
In recent years, the optical ad thermal difficulties of lens and dish concentrators have been overcome through the use of arrays of small-aperture mirrored concentrator systems. Although these systems are slightly less efficient than a single-mirror system, the Cassegrainian two-element lens system confers several advantages on a solar concentrator system: 1) the folded optical path is more compact than a single-element lens; 2) higher efficiency and concentration than a Fresnel lens; 3) absence of chromatic aberrations. Since the focal point is positioned between the two elements and can be positioned near the apex of the primary element, the cell with its heat sink can be placed at that point. With the cell heat sink proximate to the assembly backpan, efficient thermal dissipation to the air becomes simple. For these reasons at the Physics Department of the University of Ferrara an important part of the research activity is oriented to the creation of prototypes of Cassegrainian concentrator systems.

1.6 OPTICAL DESIGN OF A CASSEGRAINIAN CONCENTRATOR

Several practical design goals influence the detailed configuration of a Cassegrainian optic for use in concentrating panels. Ease and economy for automated manufacturing, module compactness, passive cooling, and reasonable optical tolerances that facilitate tracker design are foremost. Furthermore, minimizing secondary mirror shadowing and accurate alignment of the two mirrors during manufacturing form additional constraints. Usually secondary mirror shading is chosen to be < 4% to retain reasonable system efficiency; this leads to optical constrains that position the focal point between the primary mirror apex and the secondary mirror. However, it is advantageous to place the cell and heat sink at or below the apex of the primary mirror to facilitate heat transfer to the backpan. These conflicting constraints can be overcome by inserting a nonimaging TIR light guide between the focal point and the cell, permitting cell placement behind the focal point. Concurrently, tailoring the light guide design may either expand the acceptance angle or permit higher concentrations. Figure 1.13 compares the focal position at 0° and 1° pointing error at the entrance to the light guide [1].

The diagrams are taken from ray trace models of the incoming light through the full Cassegrainian optical system. The cell active area position is also indicated in relation to the light guide entrance, with the relative intensity of the light at the focal point indicated by concentric circles. It can be seen that at higher deviation angles, light that would otherwise fall off of the cell is guided back to the active area through TIR at the guide walls.

Without the guide, only a much larger cell would intercept off-track rays effectively. Alternatively, the same size cell could be employed but with far more stringent demands placed upon the tracking system. The use of a light guide as tertiary optical element results in lower cell costs, more efficient thermal management and less onerous tracker requirements. Since the optical focal point corresponds to the top of the light guide, any unintentional defocusing protects the optics by lowering, rather than raising, the optical flux on the guide. In the event of gross pointing errors, the focal point is well above the primary mirror, thereby averting severe damage to the mirror while maintaining the concentrated flux safely within the panel.

The resulting design is shown in Figure 1.14, while Figure 1.15 shows a Cassegrainian concentrator prototype, made of four modules, realized at the Physics Department of the University of Ferrara.

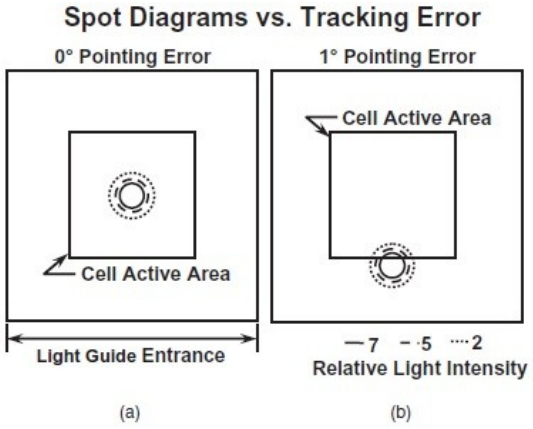

Figure 1.13 Modeling of focal point for 0° (a) and 1° (b) pointing error. At 0°, all the light strikes the cell; with no guide, a 1° pointing error moves nearly all the focused light fully off the cell; with the guide, all of the light is reflected back onto the cell active area.

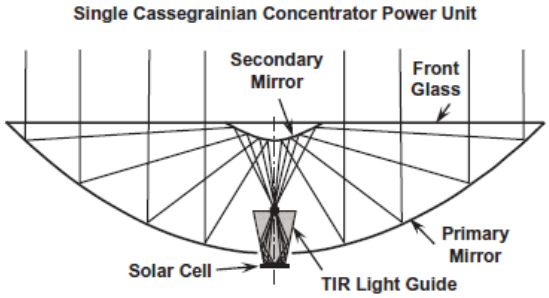

Figure 1.14 Cross section through the center of the optics for an aplanatic Cassegrainian optical system with tertiary element light guide. The light guide greatly expands the tolerable pointing error.

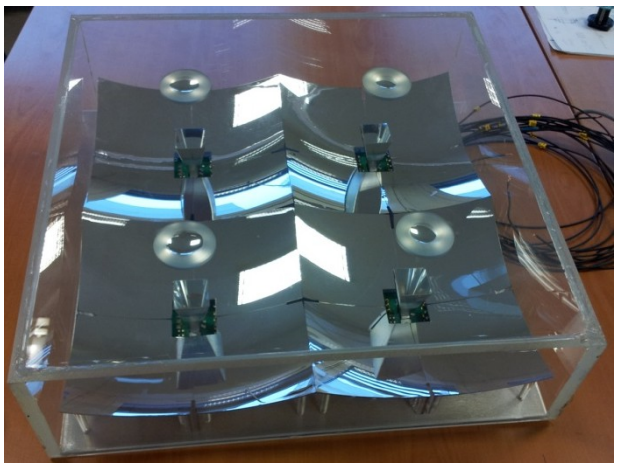

Figure 1.15 Cassegrainian concentrator prototype realized at the Physics Department of the University of Ferrara

1.7 CASSEGRAINIAN CONCENTRATOR SYSTEM FEATURING SPECTRAL SPLITTING

The HCPV Cassegrainian optical configuration offers an additional opportunity for increasing collection efficiency. Through the use of dichroic filters it's possible to split the solar spectrum into a number wavebands and to direct each filtered light beam towards suitable cells. For example the dual-focus Cassegrainian solar concentrator module concept, which was first described and developed by Fraas and Shifman et al. [17-18], uses a dichroic secondary mirror to split the solar spectrum into two parts and to direct the IR and near-visible portions of the spectrum to two separate cell locations. The second solar cell is located behind the dichroic secondary as shown in Figure 1.12. This is an important method for harvesting lost energy stemming from the current imbalance present in multijunction solar cells, or for utilizing materials and bandgap combinations not otherwise available.

As shown in Figure 1.16, the first version of this solar concentrator PV module used InGaP/GaAs double-junction cells located at the near-visible focus at the center of the primary and GaSb IR solar cells located behind the secondary.

The spectral splitting approach introduces two key advantages: 1) for each waveband a suitable solar cell with optimal bandgap can be used, in order to increase the conversion efficiency; 2) separate cell locations divide the heat load so cells work cooler at higher-efficiency points.

The first advantage is demonstrated by the use of the InGaP/GaAs and GaSb cell set rather than the traditional InGaP/GaAs/Ge monolithic triple-junction cell. Unfortunately, the three materials in the monolithic triple-junction cell do not have the ideal bandgap energies for an ideal monolithic triple-junction cell. The Ge bandgap energy is too low, generating excess current compared to the other two junctions. The excess current is wasted as heat. In contrast, the higher bandgap GaSb IR cell generates

a higher voltage, and the separate electrical connection extracts all the power produced. Overall module efficiency is thereby increased.

The spectral splitting approach is being adopted at the Physics Department of the University of Ferrara; Figure 1.17 shows a tricroic Cassegrain concentrator. It makes use of three different receivers: InGaP, GaAs and Si. Cross section shown in Figure 1.13 illustrates its working principle. Receivers are placed in a box at the back side of the primary mirror; in this way fin heat sinks can be easily mounted at the box walls.

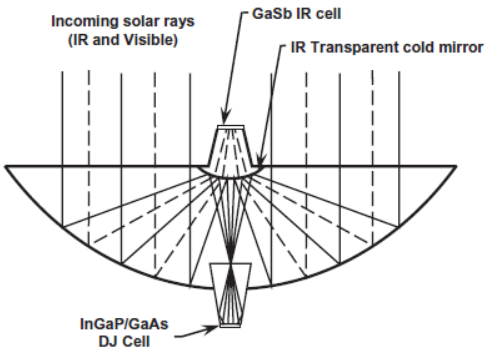

Figure 1.16 Dual-focus Cassegrainian PV module with dichroic secondary for use with separate multijunction solar cells.

The system makes use of two dichroic filters, 45° tilted, placed in the receiver box. The first receiver reflects the portion of the spectrum with $\lambda < 650$ nm and direct it onto the InGaP cell, while the second dichroic filter reflects the portion with $\lambda < 850$ nm and direct it onto the GaAs cell. The remaining part of the spectrum is transmitted through both filters and reaches the Si cell. Suitably optimized, this system is expected to reach 30 % efficiency.

1.8 INTRODUCTION TO CONCENTRATOR SOLAR CELLS

In this section we will review the main physical mechanisms that govern the operation of a semiconductor solar cell. Since such a kind of devices are essentially p-n junctions suitably engineered, in our analysis we will assume that the electrical properties of p-n junction are known and we will concentrate on what happens when a p-n junction is illuminated.

For the sake of simplicity we assume a monochromatic illumination of the cell, from the p-material side, with an energy of the photons such that $h\nu = E_G$. Furthermore, we assume that electron-hole pairs are generated only in the p-region at a distance from the p-n junction shorter than the electron diffusion length.

In order to comprehend the behaviour of a p-n junction under illumination we can consider three different cases: the short-circuit condition, the open-circuit condition and the case when an external

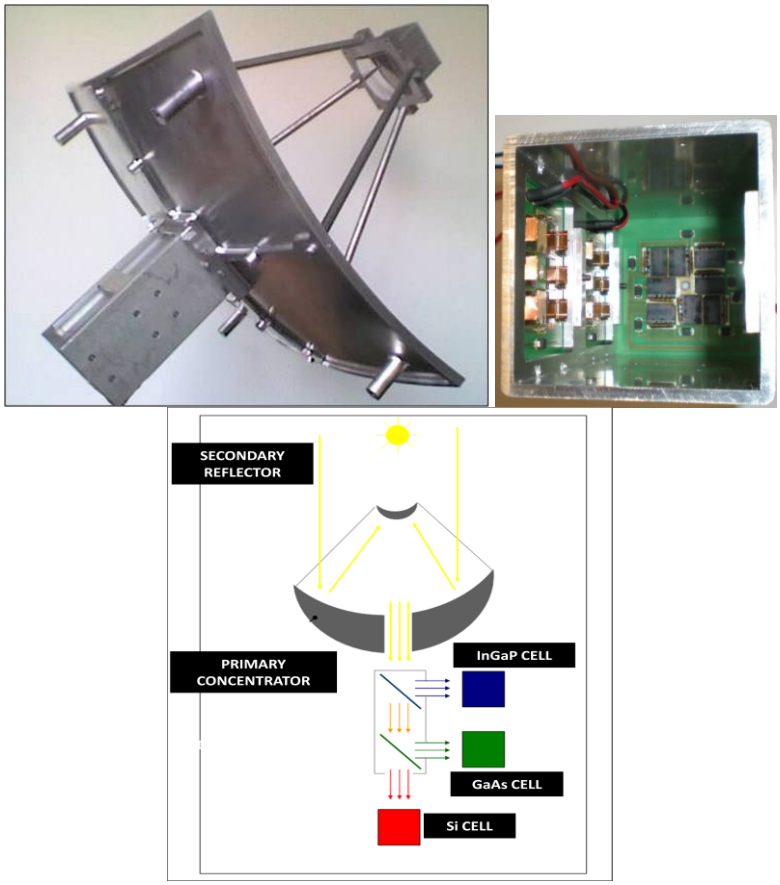

Figure 1.17 Tricroic Cassegrainian concentrator realized at the Physics Department of the University of Ferrara. Overall structure (top left), box containing the three receivers placed at the back side of the primary mirror (top right) and pictorial representation of the working principle (bottom)

load resistance is connected to the cell terminals [2]. The three cases are schematically represented in Figure 1.18.

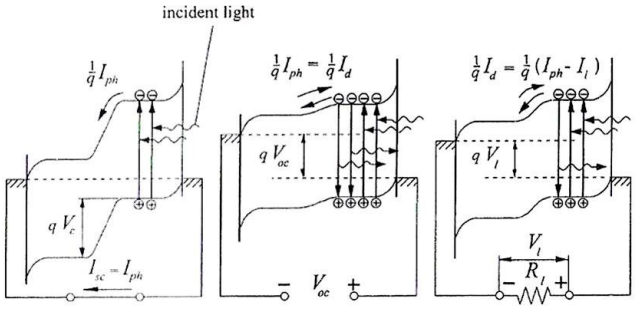

Figure 1.18 The band energy diagram of a p-n junction under illumination: in the short-circuit regime (left), in the open-circuit regime (center) and connected to an external load resistance (right).

In the short-circuit regime the external connection provides a zero potential difference between the n- and p-regions, so that the band energy diagram is equal to the band diagram of a p-n junction at thermodynamic equilibrium (without illumination and without bias voltage). In this case, however, a photogenerated current flows through the circuit. Electrons collected by the p-n junction at the n-side reach the back metal contact at the n-side and flow through the external wire. When they reach the interface between metal and the p-region they recombine with the photogenerated holes.

It is important to note that the energy diagrams of the n- and p-regions in the vicinity of the contacts correspond to the ideal non-rectifying (i.e. ohmic) contacts between a metal and a semiconductor without a barrier for the carrier flow-over. This situation can be arranged by more heavy doping the n- and p-regions in the vicinity of the contacts, so that $E_C - E_F$ and $E_F - E_V$ would be equal to zero, and also by choosing metals characterized by the corresponding Fermi level energy positions, similar to those in the semiconductor.

At open-circuit-regime electrons entering the n-region collect there and charge it negatively. At the same time, holes entering the p-region charge it positively. The resulting potential difference is called open-circuit voltage V_{OC}. This case is shown in the center part of Figure 1.1.

The V_{OC} magnitude is always less than the contact potential V_C, so that always exists a little step ΔE_C on the p-n junction diagram; this means that the potential energy of electrons near the conduction band bottom is lower in the n-region than that in the p-region. This fact is essential for an effective extraction of photogenerated electrons from the p-region into the n-region. The photocurrent I_{ph} doesn't depend on the p-n junction bias voltage. It can be expressed as the number of photogenerated carriers passing through the p-n junction in a unit time:

$$I_{ph} = q\frac{P_r}{h\nu} \tag{1.8}$$

where P_r is the incident monochromatic radiation power. Obviously, we are assuming that each incident photon generates an electron-hole pair; this condition is usually met satisfied for solar cells based on Si and GaAs.

At short-circuit regime, the short-circuit current is equal to the photocurrent:

$$I_{sc} = I_{ph} \tag{1.9}$$

Under open-circuit conditions the photocurrent is in equilibrium with the "dark" current I_d, the forward current produced by the p-n junction when it is biased with a potential difference V_{oc}. So we have:

$$I_d = I_0\left[exp\left(\frac{qV_{oc}}{AkT}\right) - 1\right] = I_{ph} \tag{1.10}$$

From (1.10) it's possible to find an expression for V_{oc} (at $I_{ph} \gg I_0$)

$$V_{oc} = \frac{AkT}{q} ln\left(\frac{I_{ph}}{I_0} + 1\right) \approx \frac{AkT}{q} ln\frac{I_{ph}}{I_0} \tag{1.11}$$

The "dark" current is accompanied by recombination of minority carriers (in our case electrons in the p-region). At recombination potential energy of electron-hole pairs is either released by means of emission of photons with $h\nu \approx E_G$ (radiative recombination), or dissipated as heat in the crystal lattice. Radiative recombination is represented in Figure 1.1 with arrows.

In order to find a general expression for the I-V characteristic of an illuminated p-n junction, we assume that a power generator is connected to the junction terminals. At a positive bias voltage the photocurrent is subtracted from the "dark" current, and at a negative one is summed to it. Assuming the direction of I_{ph} as positive, we can write:

$$I_l = I_{ph} - I_0 \left[exp\left(\frac{qV_l}{AkT}\right) - 1 \right] \tag{1.12}$$

where V_l is the voltage drop across the load resistance and I_l is the current flowing through it. Figure 1.19 shows an I-V characteristic of a solar cell [2]. Only portion of the curve in the second quadrant is shown, since only there the cell acts as a power source, since the direction of the current is "opposite" to the applied voltage polarity. Load resistance I-V characteristic is given by:

$$I_l = V_l / R_l \tag{1.13}$$

Figure 1.19 also shows load resistance I-V characteristics for different values of R_l itself.

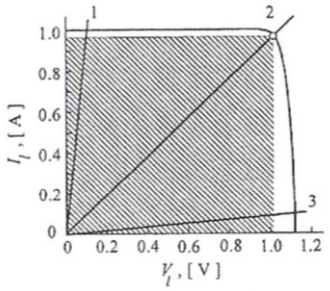

Figure 1.19 Illuminated I-V curve of a p-n junction in GaAs and I-V characteristics of load resistance R_l for different magnitudes of R_l, 0.1 Ω (1), 1.026 Ω (2) and 10 Ω (3).

Now we can calculate output electric power in the load resistance:

$$P = I_l V_l = I_{ph} V_l - I_0 V_l exp\left(\frac{qV_l}{AkT}\right) \tag{1.14}$$

Since in both short circuit and open circuit regimes P = 0, for either V_l or I_l is equal to zero, there exists some optimum value of $R_l = R_{opt}$, at which the cell provides its maximum output power. To find the corresponding values of $V_l = V_m$ and $I_l = I_m$, we have to solve the equation $dP/dV_l = 0$:

$$\frac{dP}{dV_l} = I_{ph} - I_0 \left[\frac{qV_m}{AkT} exp\left(\frac{qV_m}{AkT}\right) + exp\left(\frac{qV_m}{AkT}\right) \right] = 0 \tag{1.15}$$

After some rearrangements we obtain [1]

$$V_m \approx V_{oc} - \frac{AkT}{q} ln\left(\frac{qV_m}{AkT} + 1\right) \tag{1.16}$$

Equation (1.16) can be solved by the successive approximations method. Two calculations are enough to obtain four correct significant figures. Substituting V_m into the (1.12) we obtain

$$I_m \approx I_{ph} - I_0 exp\left[\frac{qV_{oc}}{AkT} - ln\left(\frac{qV_{oc}}{AkT} + 1\right)\right] \approx I_{ph}\left(1 - \frac{AkT}{qV_m}\right) \quad (1.17)$$

Thus it's possible to determine $R_m = V_m/I_m$ and, finally, P_m:

$$P_m = V_m I_m \approx I_{ph}\left[V_{oc} - \frac{AkT}{q} ln\left(\frac{qV_m}{AkT} + 1\right) - \frac{AkT}{q}\right] \quad (1.18)$$

The value of P_m corresponds to the area of the crosshatched rectangle in Figure 1.2.

The fill factor (FF) of an I-V characteristic is a parameter evaluating its "quality":

$$FF = \frac{P_m}{I_{sc}V_{oc}} = \frac{I_m V_m}{I_{sc}V_{oc}} \quad (1.19)$$

Fill factor quantifies how much the shape of an I-V characteristic of a solar cell is close to a rectangle. In this thesis several works based on concentrator solar cell numerical simulation will be presented. In all of them fill factor has been taken into account as figure of merit of the cell, since it is a parameter that gives an overall view of the cell working conditions.

The above obtained expressions allow us to better understand the fundamental physical parameters that limit the efficiency of an ideal solar cell [2].

The expression (1.18) can be rewritten as

$$P_m = I_{ph}\left(\frac{E_m}{q}\right) \quad (1.20)$$

where

$$E_m = q\left[V_{oc} - \frac{AkT}{q} ln\left(\frac{qV_m}{AkT} + 1\right) - \frac{AkT}{q}\right] \quad (1.21)$$

is the energy calculated for each absorbed photon, which is transferred to the load resistance at an optimum matching of the p-n junction and the external circuit. Rearranging the expression (1.21) it's possible to highlight the factors having effects on the value of E_m. Substituting in (1.14) the expression for V_{oc} given in (1.11) and the following expression for i_0 reported in [2]:

$$i_0 = ktN_c N_v\left(\frac{\mu_n}{L_n N_A} + \frac{\mu_p}{L_p N_D}\right) exp\left(-\frac{E_g}{kT}\right) \quad (1.22)$$

we obtain, after a further rearrangement

$$E_m = E_g - kT\left\{ln\left(\frac{N_c}{N_D}\right) + ln\left(\frac{N_v}{N_A}\right) + ln\left[\frac{kT}{i_{ph}}\left(\frac{\mu_n N_D}{L_n} + \frac{\mu_p N_A}{L_p}\right)\right] + ln\left(\frac{qV_m}{kT} + 1\right) + 1\right\} \quad (1.23)$$

Equation (1.16) shows that the energy gap E_g, defining the potential energy magnitude of one photogenerated electron-hole pair, is the upper estimation limit for E_m. The second term in the curly brackets represents in (1.23) represents losses of a fundamental character, constraining efficiency of a solar cell. The first two addenda in the curly brackets reflect the fact that the contact potential difference V_c is lower than than the magnitude of E_g / q [2]. The "losses due to V_c" depend on the

density of states in the valence and conduction bands of a semiconductor, and also on the majority carrier concentrations in the n- and p-regions of the p-n junction. The third addendum reflects the fact that $V_{oc}<V_c$. This kind of losses depend on the majority carrier concentration and electrophysical parameters (mobility, diffusion lengths) of the minority carriers in the n- and p-regions of the p-n junction. The fourth addendum depend on the three previous addenda (see the expression (1.16)) and reflect the fact that $V_m<V_{oc}$. Finally, the fifth addendum (kT multiplied by unity) can be interpreted as "losses due to optimum current", and depend on the fact that the current I_m is less than the photocurrent (see the expression (1.17)).

Keeping in mind that a monochromatic illumination of the p-n junction has been supposed, the conversion efficiency can be defined as the ratio of E_m to the energy of one absorbed photon hν:

$$\eta = E_m/h\nu \tag{1.24}$$

As is known, sunlight is not monochromatic; solar cell parameters, especially the energy gap E_g, has to match the real solar radiation spectrum.

As is known, the longest wavelength λ_g, starting from which photons can be absorbed in the solar cell material with the energy gap E_g, is

$$\lambda_g[\mu m] = 1.24/E_g[\mu m] \tag{1.25}$$

Photons with longer wavelength are not absorbed in the semiconductor and their energy is lost from the point of view of photovoltaic conversion.

Conversely, photons with an energy $h\nu > E_g$, produce "hot carriers" which, in addition to the excess potential energy E_g, gain the excess kinetic energy equal to the difference $h\nu - E_g$. However, this kinetic energy is rapidly spent heating the crystalline lattice. Thus only photons from a high-energy part of the spectrum are absorbed by the semiconductor, and only part of the energy of these photons is converted into the potential energy of the electron-hole pairs. Knowing the spectral distribution of the photon flux incident onto the cell surface it's possible to obtain the photocurrent density produced by the cell in the following way:

$$i_{ph} = q \int_{h\nu=E_g}^{\infty} \frac{dn_{ph}}{d(h\nu)} d(h\nu) \tag{1.26}$$

From (1.26) it can be deduced that, for a given spectral photon distribution, i.e. for a given solar radiation spectrum, photocurrent density decreases at increasing energy gap E_g of the p-n junction material. Figure 1.20 shows the dependence of i_{ph} on E_g for the solar spectra AM 0 and AM 1.5D [2]. The maximum energy utilized in the load for one absorbed photon (E_m in (1.23)), rises initially with increasing E_g and then starts to decrease when the change of the term containing i_{ph} becomes substantial.

The solution of the problem to find the optimum value of E_g depends on the way we determine E_m.

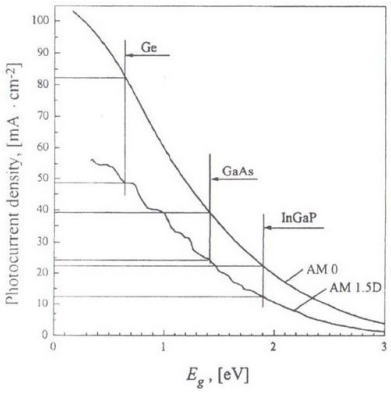

Figure 1.20 Dependences of the photocurrent density on the energy gap E_g, for the spectra AM 0 and AM 1.5D.

A known method of calculation of E_m is based on thermodynamic considerations [19-21]. A semiconductor solar cell, being in thermodynamic equilibrium with the surroundings, exchanges energy by means of radiant emission and absorption. The equilibrium black-body radiation which always exists inside a solar cell material at a given temperature defines the lower limit of the saturation current density i_0 in the p-n junction. According to [11], i_0 is given by:

$$i_0 = \frac{q(n^2+1)E_g^2 kT}{4\pi^2\hbar^3c^2} exp\left(-\frac{E_g}{kT}\right) \tag{1.27}$$

where n is the refractive index of the solar cell material. Physically, this expression presents i_0 as " a photocurrent generated by the intrinsic black-body irradiation". For its calculations the spectral distribution of the black-body radiation at the solar cell temperature is used, the contribution to i_0 being given by photons with $h\nu \geq E_g$. Then, knowing i_{ph}, one can find V_{oc} from (1.11), E_m from (1.21) and "monochromatic" efficiency from (1.24) at $h\nu = E_g$. These values of efficiency are depicted in Figure 1.21 by the lines 2, 3, 4 for three magnitudes of i_{ph}.

The wavelengths in the abscissa should be considered as that corresponding to E_g for individual semiconductor materials, as given in (1.25). For a chosen material the conversion efficiency magnitudes for light with wavelengths shorter than λ_g have to be reduced λ_g/λ times, which is pictured in the figure by three tilted straight lines for three semiconductor materials ($In_{0.5}Ga_{0.5}P$, GaAs and Ge) and i_{ph} = 1 A·cm^{-2}. The conversion efficiency of a solar cell based on a chosen material can be obtained by multiplication of magnitudes taken from the corresponding tilted straight line by the solar spectrum, and then by integration over wavelengths up to λ_g. The energy spectrum AM 0 is depicted in Figure 1.21 by the curve 1, and the results of multiplication for the above mentioned materials by the curves 5, 6, and 7. Thus the thermodynamically limited maximum value of the efficiency η_{max} for an idealized solar cell on the base of each chosen material is taken as the area enclosed by curve 5, 6, 7 when the area enclosed by curve 1 corresponds to 100%.

As in the case of conversion of monochromatic light, the values of η_{max} rise with increasing

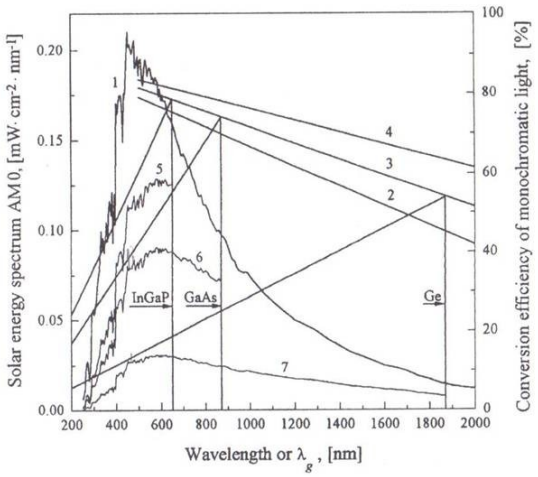

Figure 1.21 Curve 1 – the energy spectrum AM 0 for non-concentrated sunlight; lines 2, 3 and 4 – plots of maximum monochromatic efficiency off an idealized solar cell for i_{ph} = 0.1; 1 and 10 A·cm^{-2} respectively; sloped lines – spectral dependences of conversion efficiency in the idealized solar cells based on $In_{0.5}Ga_{0.5}P$, GaAs and Ge, at i_{ph} = 1 A·cm^{-2}; curves 5, 6 and 7 show the portion of solar energy converted into electricity in the corresponding solar cells.

photocurrent density, i.e. with concentration of sunlight.

If we denote the Sun concentration ratio as K_S, calculated magnitudes of $\eta_{max} = f(E_g)$ at conversion of non-concentrated (K_s=1) and concentrated (K_s=1000) sunlight are presented in Figure 1.22. AM 0 and AM 1.5D spectra have been considered. As can be seen from the figure, silicon and gallium arsenide have an energy gap magnitude that fall just into the range of the highest values of η_{max}.

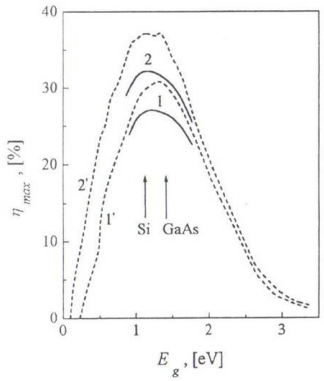

Figure 1.22 Maximum thermodynamic conversion efficiency of a solar cell made of a material with an energy gap E_g, where T = 300 K. 1, 1' – K_s = 1; 2, 2' – K_s = 1000; 1, 2 – for the Sun spectrum AM 0; 1', 2' – for the Sun spectrum AM 1.5D.

The maximum efficiency is about 31% for K_s = 1 and 37% for K_s = 1000 (AM 1.5D). These limits, calculated for a single junction solar cell, can be overcome by adopting multi-junction solar cells.

2 OHMIC LOSSES IN SOLAR CELLS

Ohmic losses in solar cells basically arise from the fact that semiconductor and metal layers by which a solar cell is made of are characterized by a non-zero resistivity value. As a consequence, as in any electric generator, in a real semiconductor solar cell a part of the generated power is dissipated at the internal resistance. Solar cells for conversion of concentrated sunlight have to be designed in such a way that internal ohmic losses are drastically reduced. Production of high-current high-efficiency solar cells implies an accurate choose of parameters of a semiconductor structure and of a solar cell design as a whole, taking into account optical, recombination and ohmic losses.

In the related literature there is no universally adopted procedure for the description and measurement of the ohmic losses in solar cells, despite the fact that solar cells have been used, for instance, in power supply systems for spacecrafts for almost forty years.

In this chapter, taken from [2], various aspects related to ohmic losses will be discussed in detail. Such a description will allow us to gain a deep insight into the problem. Several solar cell models with lumped and distributed parameters will be considered. An analytical approach will be developed in order to calculate illuminated current-voltage characteristics with known values of the internal resistance components.

2.1 INTERNAL RESISTANCE PROBLEM

Fig. 2.1a shows a simplified version of a typical solar cell geometry, that is a rectangular semiconductor wafer with a planar p-n junction. On the illuminated side a busbar contact is situated, and on the back side a solid one. It is assumed that incident light is uniformly distributed on the whole light-sensitive surface. Furthermore, every incident photon generates electron-hole pairs, which are then separated by the p-n junction.

In their travel towards the busbar contact, the photogenerated carriers overcome the sheet resistance of the p-n junction front region (the n-region in this case), then the metal-semiconductor contact resistance (the resistance of an intermediate region between the n-type layer and the busbar contact) and the resistance of the metallic contact strip. The resistance of the base region of the solar cell (the p-region in this case) and the contact resistance on the back surface are connected in series to the external load. In many types of solar cells intended for conversion of concentrated sunlight the resistances of the base region and of the back contact don’t constrain the output power, since the base region may be highly doped and the back contact area is much larger than that of the contact grid on the front surface. The relations between the main resistance components (the sheet resistance, the

contact resistance and the resistance of the strip) and the recombination and optical losses can be considered as follows. The sheet resistance of the solar cell n-region can be reduced, for instance, by increasing its thickness w.

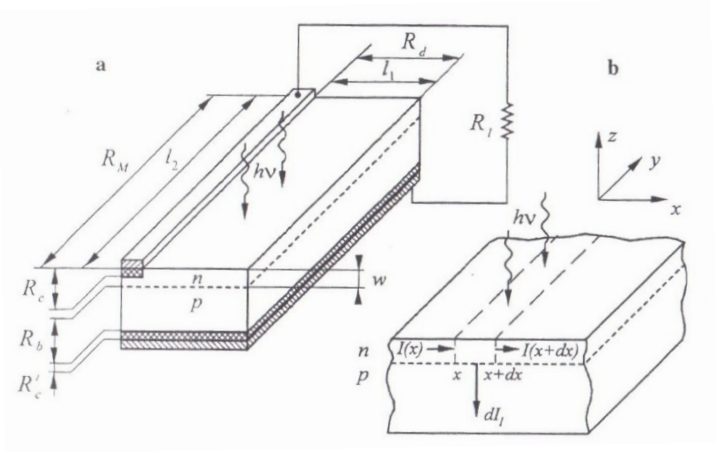

Figure 2.1 a – A "classic" design of a solar cell with a busbar contact, and b – scheme of current flow through a small part of a solar cell

However, this will result in an increase in the recombination losses, because collection by the p-n junction of holes generated by light in the vicinity of the surface will not be so effective. The same result may also be caused by increasing electric conductivity of the n-region at the expense of an increase in the doping level. What is more, the possibility of decreasing the resistance in such a way is restricted by the solubility limit of donor impurities and by their capability to create new free electrons. One may reduce radically the n-layer resistance by decreasing the solar cell size l_1 or by making several parallel contact strips connected with each other with an additional bus. However this will lead to an increase in the optical losses, for a significant part of the light-sensitive surface appears to be covered by the contact grid. In the solar cells intended for conversion of non-concentrated sunlight grid fingers are spaced 2-5 mm apart for a resulting shadowing coefficient of about 5%. In this case the grid pattern is prepared by the silk screening technique. In the high-current solar cells finger spacing is reduced to 0.1-0.3 mm, which requires application of a photolithographic process. For such solar cells the shadowing coefficient may approach 10-15%.

The magnitude of the contact resistance decreases with increasing contact area, however the optical losses tend to be higher. This resistance depends on the choice of metal (or alloy) for the contact and on the technology of metal deposition and thermal treatment. Such metals as Ni, Ag, Au, Pd, Cr, Al (for Si) and also combinations of layers of these metals are more widely used for making contacts to solar cells based on Si and GaAs. The deposition processes are vacuum deposition, chemical deposition, electroplating, or painting with a paste containing a metallic powder. Temperature and

duration of the thermal treatment also have an essential effect on this magnitude. The critical factor in this case is a risk of melt-through of the thin front region of the p-n junction. Let's consider an action of the sheet resistance of the front region in a solar cell which has a distributed nature regarding to the area of the p-n junction. We shall characterize it by its value R_d:

$$R_d = \rho l_1 / w l_2 \tag{2.1}$$

where ρ is the resistivity of the front layer material; w is the layer thickness; and l_1 and l_2 are the solar cell dimensions across the contact strip and along it, respectively. Let's make the following assumptions: w and the contact strip width are much smaller than l_1; the contact resistances R_c and R'_c are equal to zero; the longitudinal resistance of the metallic strip $R_M \ll R_d$; the base resistance $R_b = 0$. In this case it can be assumed that the potential V of the p-n junction front region change only along the x-axis normal to the contact strip.

To deduce $V(x)$ we shall consider a section of a solar cell of width dx (see Figure 2.1b). Part of the load current flows through the p-n junction section of width dx, i.e.

$$dI_l = \left\{ i_{ph} - i_0 \left[exp\left(\frac{qV(x)}{AkT} \right) - 1 \right] \right\} l_2 dx \tag{2.2}$$

The equation for the current flowing along the front layer has a form

$$I(x) = I(x + dx) + dI_l \tag{2.3}$$

According to Ohm's law, the current $I(x)$ is defined as the ratio of the varation in potential to the resistance of the section dx (defined similarly to equation (2.1)). Hence, allowing for the decrease of V along x

$$I(x) = -\frac{w l_2}{\rho} \frac{dV(x)}{dx} \tag{2.4}$$

In the same way one may write an expression for $I(x + dx)$. Then using equation (2.2) after regrouping the terms we can rewrite equation (2.3) in the form

$$\frac{d^2V(x)}{dx^2} = \frac{\rho}{w} \left\{ i_{ph} - i_0 \left[exp\left(\frac{qV(x)}{AkT} \right) - 1 \right] \right\} \tag{2.5}$$

Boundary conditions for this equation are:

$$V|_{x=0} = V_l \tag{2.6}$$

Because the voltage at the contact strip is equal to the voltage at the load, and

$$\left.\frac{dV}{dx}\right|_{x=l_1} = 0 \tag{2.7}$$

which follows from equation (2.4), since current doesn't flow through the right hand edge of the solar cell. When the external circuit is open, no current flows along the front layer, owing to all sections of the solar cell being uniformly illuminated. Then it follows from equation (2.4) that $dV(x)/dx = 0$, i.e. all points of the front layer have the same potential equal to the open circuit voltage, namely to that one which the solar cell would have at $R_d = 0$:

$$V_{oc} = \frac{AkT}{q} ln\left(\frac{i_{ph}}{i_0} + 1\right) \tag{2.8}$$

Having the form of the function $V(x)$ from equation (2.5), allowing for equations (2.6) and (2.7) and setting the values of V_l from 0 to V_{oc}, one may define the magnitude of the current I_l through the load resistance at the chosen value of V_l by integrating equation (2.2) to give:

$$I_l = \int_0^{l_1} \left\{ i_{ph} - i_0 \left[exp\left(\frac{qV(x)}{AkT}\right) - 1 \right] \right\} l_2 d_x \tag{2.9}$$

In rather a complicated manner the illuminated I-V characteristic of a solar cell could be constructed by points.

Unfortunately, the equation (2.5) cannot be solved analytically. In a number of works the problem was solved in an approximated form. One of the solution methods giving a "classical" result is the small parameter method. It is appropriate when the front layer resistivity is small enough. In this case a correction to the value of V_l corresponding to $\rho = 0$ is sought:

$$V_l|_{\rho=0} = \frac{AkT}{q} ln\left(\frac{I_{ph} - I_l}{I_0} + 1\right) \tag{2.10}$$

In the first approximation the correction appears to be equal to $-\frac{1}{3}\frac{\left(\rho/w\right)}{\left(l_1/l_2\right)}I_l = -\frac{1}{3}R_d I_l$, so the voltage at the load resistance at $\rho \geq 0$ is given by

$$V_l \approx \frac{AkT}{q} ln\left(\frac{I_{ph} - I_l}{I_0} + 1\right) - \frac{1}{3}R_d I_l \tag{2.11}$$

The latter expression corresponds to the situation when a lumped (series) resistance of magnitude $R_s = \frac{1}{3}R_d$ is connected in series to the p-n junction. Any contact resistance R_c may be added into the series resistance of the solar cell since it is a lumped one with respect to the total area of the p-n junction:

$$R_s = \frac{1}{3}R_d + R_c \tag{2.12}$$

Let us illustrate the effect of R_s on the shape of the current-voltage characteristics of a solar cell in the dark and under illumination. The equivalent circuit of a solar cell is pictured in Figure 2.2a. Both I-V characteristics in the dark and under illumination (Figure 2.2b) are found by an algebraic summation over voltage at the same current values of the p-n junction I-V characteristic (dashed curve) and of that for the resistance R_s. The latter is a straight line passing through the origin of the coordinates at angle γ, the cotangent of which is equal to R_s. The shape of the I-V characteristic under illumination is defined by the expression (2.11), which can be rewritten in the following way:

$$I_l \approx I_{ph} - I_0\left\{exp\left[\frac{q(V_l - R_s I_l)}{AkT}\right] - 1\right\} \tag{2.13}$$

The corresponding graph is close to the real shape of the illuminated I-V characteristic of a solar cell only in the case when the potential drop across the resistance $1/3\,R_d$ does not exceed AkT/q:

$$I_l \cdot \frac{1}{3}R_d \leq \frac{AkT}{q} \tag{2.14}$$

It is seen from Figure 2.2b that the V_{oc} value for an illuminated solar cell with internal ohmic losses coincides with that for a solar cell without losses, and is also equal to the voltage on the p-n junction when a dark current equal to the photocurrent ($I_d = I_{ph}$) is flowing through it. This circumstance is valid under uniform illumination conditions and allows us to construct the I-V characteristic of the p-n junction in a real solar cell excluding an error caused by any internal voltage drops. The p-n junction I-V characteristic is the dependence $I_{ph} = f(V_{oc})$ when the intensity of illumination is varied.

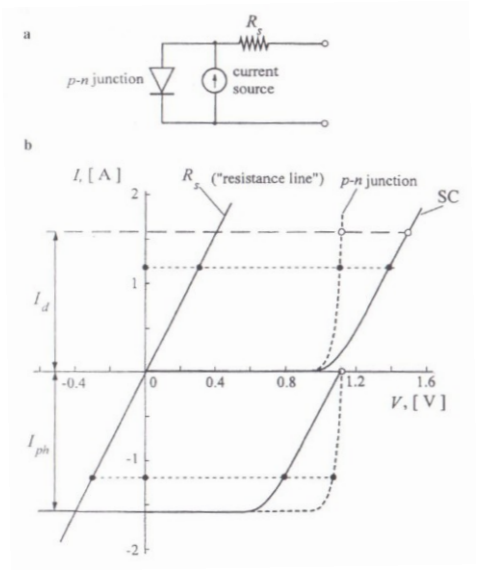

Figure 2.2 a – The equivalent circuit of an illuminated solar cell with a series resistance, and b – construction of dark and illuminated I-V characteristic of the solar cell with a series resistance

Comparison of the corresponding curve with the real dark or illuminated I-V characteristic of a solar cell reveals an action of the internal resistance.

The recalculation procedure from the distributed resistance of the front solar cell region into the effective lumped (series) one, similar to that discussed above, is considered in a number of publications. In other works a reverse problem is solved, the evaluation of R_s from the experimental I-V characteristic of a solar cell.

In some works more exact solutions of (2.5) are proposed. However, rather cumbersome analytical expressions are given for the I-V characteristic. If complexity is added to the calculation procedures, it is pertinent to use numerical solutions. An accurate solution by the model with the distributed R_d gives an excellent fit to experimental points, whereas the model with a series resistance gives an essentially different shape of the I-V characteristic. For the description of the ohmic losses in a solar cell some authors propose to introduce some effective series resistance of a value R_S^{eff} which appears to be dependent on the illumination level though none of the components of the internal resistance in this case depends on illumination. An accurate calculation reveals a main feature of the illuminated I-V characteristic of a solar cell with distributed parameters in comparison with that of a solar cell with a series resistance, i.e. smoothing of the bend between the horizontal and tilted portions of the curve. It should be noted that the maximum power point whose correct position defines an accuracy of calculation of the output electric power and efficiency of a solar cell, is located just at this part of the curve.

Thus, two approaches are mainly used in scientific publications to simulate the effect of the internal ohmic losses on the shape of the solar cell I-V characteristic. The first approach consists of a

maximum simplification of the problem. The equivalent circuit of a solar cell is imagined as consisting of a lumped diode and an effective series resistance (Figure 2.2a). This is justified in describing a solar cell I-V characteristic in such a range of operating currents when the potential drop along the distributed components of the resistance is comparable with the value AkT/q. When the operating current is increased, i.e. the case of concentrated sunlight conversion, the I-V characteristic shape differs essentially from the predicted one. A lumped equivalent of the distributed resistance depends on the illumination level and has a nonlinear character along the I-V curve under illumination.

The second approach is computer simulation of the internal resistance problem in a numerical form. Several works show that the results of computation fit well to the experimental I-V characteristic of a solar cell at any illumination level. Sometimes a multicomponent equivalent circuit of a solar cell consisting of a chain of diodes and resistors was used as a model for calculation. It gave the possibility to simulate exactly the operation of a solar cell with distributed ohmic losses in the front region and in the contact strip. There also exists an "intermediate" approach employing physical justified chain-type multicomponent models of the solar cell, and allowing us to obtain simple (at a little number of chain sections) analytical expressions for the coordinates of a number of points in the I-V characteristic at any level of illumination. This is feasible due to application of the partial-linear approximation for the I-V characteristics of the lumped diodes in the chain sections of the equivalent circuit. Such an approach allows us to establish generalities of the shape-formation of the illuminated I-V characteristics for a solar cell with distributed parameters, which will be shown below.

2.2 I-V CURVE FORMATION IN SOLAR CELLS WITH DISTRIBUTED PARAMETERS

Figure 2.3 depicts a solar cell of the simplest geometry (a) and its chain-type equivalent circuit (b). It is assumed that the metallic contact strip area is negligibly small in comparison with the solar cell area; the resistance of the strip as well as the resistances of p-base and back contact are equal to zero. The front contact resistance has a lumped nature with respect to the whole area of the p-n junction, so it can be represented by a series resistance R_s. The sheet resistance of the front layer is a distributed resistance R_d. Let's mentally divide the solar cell area into n equal parts parallel to the contact strip. Each n^{th} part contains a diode, generator of photocurrent and two resistors of the magnitudes $1/2n\,R_d$, that is represented as a chain section in the equivalent circuit. Let a solar cell be uniformly illuminated and connected to a variable load resistance R_l or to a power source of a reverse bias. According to the equivalent circuit of Figure 2.3b, currents and voltages are related by a set of Kirchhoff equations

$$I_l = \sum_{i=1}^{n} I_i$$

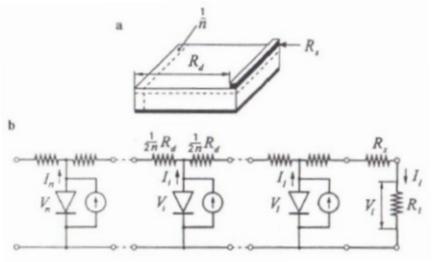

Figure 2.3 a – A simple solar cell design with a busbar contact and, b – the corresponding multisection equivalent circuit

$$V_1 = V_l + \left(\frac{1}{2n}R_d + R_s\right)I_l$$

$$V_2 = V_1 + \frac{1}{n}R_d(I_l - I_1) \tag{2.15}$$

$$V_3 = 2 + \frac{1}{n}R_d(I_l - I_1 - I_2)$$

. . . . . .

$$V_n = V_{n-1} + \frac{1}{n}R_d(I_l - I_1 - \cdots I_{n-1})$$

At a sufficient reverse bias the load current is equal to the photocurrent: $I_l = I_{ph}$ and under the open circuit condition $V_l = V_1 = V_2 = \cdots = V_n = V_{oc}$. The relationship between current and voltage in each i[th] diode is defined by the equation for an illuminated p-n junction:

$$I_i = \frac{1}{n}\left\{I_{ph} - I_0\left[exp\left(\frac{qV_l}{AkT}\right) - 1\right]\right\} \tag{2.16}$$

where I_0 is the saturation current for the whole p-n junction area and i = 1,2, … n.

Non-linearity of the conditions (2.16) is the main impediment to the solution of the set of equations (2.15). In order to simplify the problem we can consider a partial linear approximation of the I-V curves for the diodes in the equivalent circuit. In Figure 2.4 curve 1 is the exponential from equation (2.16) corresponding to the characteristic of one of the diodes. We shall replace this curve by two line segments, a horizontal one at a height of $1/n\, I_{ph}$ extending to some value of the cut voltage V_{cut} and a tilted one from V_{cut} to V_{oc}. Let's choose the value of V_{cut} so that the area under the formed polygonal line 1' would be equal to the area under the exponential 1 (so that the areas of the two hatched regions would be equal to each other). It may be shown that

$$V_{cut} = V_{oc} - \frac{2AkT}{q} \tag{2.17}$$

Let a solar cell be operating at V_l very close to V_{oc}. The relationship between current and voltage for each diode in this case will be calculated by the formula

$$I_i = \frac{1}{n} I_{ph} \frac{V_{oc} - V_i}{V_{oc} - V_{cut}} \quad for \ V_{cut} < V_i < V_{oc} \tag{2.18}$$

As V_l decreases, the net current I_l increases linearly, however the situation takes place until the voltage V_1 at the diode nearest to the load resistor drops down to the value V_{cut}.

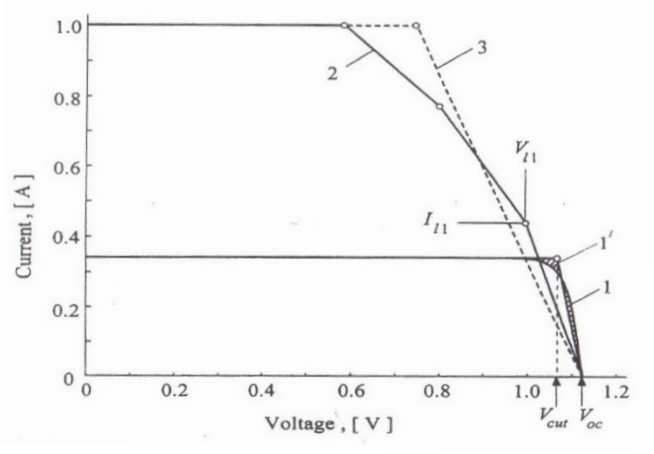

Figure 2.4 An example of constructing an illuminated I-V characteristic of a gallium arsenide solar cell assuming the three-section equivalent circuit (Figure 2.3): 1 – the exponential I-V characteristic of each of the diodes; 1' – the partial-linear approximation of the I-V characteristic; 2 – the illuminated I-V characteristic, in which the bend point position have been calculated by the formulae (2.15) at: I_{ph} = 1 A, V_{oc} = 1.14 V, R_d = 1 Ω, R_s = 0, A = 1, T = 300 K; and 3 – the same, but using the model of a solar cell with a lumped resistance

At this moment the contribution of the first diode to the current I_l is stabilized at the level $(1/n)I_{ph}$, and the net I-V characteristic suffers the first bending. The next bending (as V_l decreases) will take place at $V_2 = V_{cut}$. The total number of bend points, the coordinates of which we shall use later to construct the I-V characteristic, is equal to the chosen number n of the equivalent circuit sections. Denote the number of bend points of an I-V characteristic by the index j (j = 1, 2,… n, counting from the point V_{oc} side).

The following general solution of the equation set (2.15) at an arbitrary n was suggested in [22] on the basis of regularities in changing the formulae for the coordinates of the bend points I_{lj} and V_{lj} at the various number of sections n:

$$I_{lj} = \frac{j}{n} I_{ph} + \sum_{i=j+1}^{n} I_{ij} \tag{2.19}$$

where currents through lumped diodes of the equivalent circuit in the j[th] bend point of the I-V characteristic (i.e. I_{ij}) are defined from an auxiliary set of $(n-j)$ equations at i = j + 1:

$$(1+a)I_{ij} + aI_{(i+1)j} + \cdots + aI_{(n-1)j} + aI_{nj} = \frac{1}{n}I_{ph}$$

$$aI_{ij} + (1+2a)I_{(i+1)j} + \cdots + 2aI_{(n-1)j} + 2aI_{nj} = \frac{1}{n}I_{ph}$$

$$aI_{ij} + 2aI_{(i+1)j} + \cdots + 3aI_{(n-1)j} + 3aI_{nj} = \frac{1}{n}I_{ph}$$

$$\cdots\cdots\cdots\cdots\cdots\cdots\cdots\cdots\cdots\cdots\cdots\cdots\cdots\cdots\cdots\cdots \quad (2.20)$$

$$aI_{ij} + 2aI_{(i+1)j} + \cdots + [1+(n-1-j)a]I_{(n-1)j} + (n-1-j)aI_{nj} = \frac{1}{n}I_{ph}$$

$$aI_{ij} + 2aI_{(i+1)j} + \cdots + (n-1-j)aI_{(n-1)j} + [1+(n-j)a]I_{nj} = \frac{1}{n}I_{ph}$$

The following notation is used in (2.20):

$$a = \frac{1}{n^2}\frac{qI_{ph}R_d}{2AkT} \quad (2.21)$$

After calculating the current I_{lj}, the corresponding voltage V_{lj} is defined by the formula

$$V_{lj} = V_{oc} - \frac{2AkT}{q} - \left(\frac{2j-1}{2n}R_d + R_s\right)I_{lj} + \frac{j(j-1)}{2n^2}R_dI_{ph} \quad (2.22)$$

For example, let's consider the construction of the illuminated I-V characteristic of a solar cell at n = 3. At j=1 the set of equations (2.20) contains the number of lines n – j = 2.

$$(1+a)I_{21} + aI_{31} = \frac{1}{3}I_{ph}$$

$$aI_{21} + (1+2a)I_{31} = \frac{1}{3}I_{ph} \quad (2.23)$$

After finding I_{21} and I_{31} one can calculate I_{l1} from (2.19):

$$I_{l1} = \frac{1}{3} I_{ph} + I_{21} + I_{31} \tag{2.24}$$

and then V_{l1} can be found from (2.22).

At j = 2 the system (2.20) contains one line, therefore

$$(1 + a) I_{32} = \frac{1}{3} I_{ph} \tag{2.25}$$

$$I_{l2} = \frac{2}{3} I_{ph} + I_{32} \tag{2.26}$$

At j = n = 3 the solution is a trivial one:

$$I_{l3} = I_{ph} \tag{2.27}$$

since this is the last bend point of the illuminated I-V characteristic (counting from the V_{oc} side), after which the contribution of each of three diodes to the net load current is stabilized at the level $1/3\, I_{ph}$. After calculations using (2.23)-(2.27) and (2.22) we shall obtain the following formulae for coordinates of three bend points of the illuminated I-V characteristic:

$$I_{l1} = \frac{I_{ph}}{3}\left(1 + \frac{2 + a}{1 + 3a + a^2}\right),$$

$$V_{l1} = V_{oc} - \frac{2AkT}{q} - \left(\frac{R_d}{6} + R_s\right) I_{l1}$$

$$I_{l2} = \frac{I_{ph}}{3}\left(2 + \frac{1}{1 + a}\right),$$

$$V_{l2} = V_{oc} - \frac{2AkT}{q} - \left(\frac{R_d}{2} + R_c\right) I_{l2} + \frac{R_d}{9} I_{ph}$$

$$I_{l3} = I_{ph}\,,$$

$$V_{l3} = V_{oc} - \frac{2AkT}{q} - \left(\frac{R_d}{2} + R_c\right) I_{ph} \tag{2.28}$$

According to (2.21), in these expressions

$$a = \frac{1}{9} \frac{q I_{ph} R_d}{2AkT} \tag{2.29}$$

Figure 2.4 shows as an example the illuminated I-V characteristic constructed for a gallium arsenide solar cell (polygonal line 2) by the following initial data: I_{ph} = 1 A; V_{oc} = 1.14 V; T = 300 K; A = 1; R_d

= 1 Ω; $R_s = 0$.

Let's compare the shape of the constructed I-V characteristic with that which can be obtained in the framework of the I-V curve partial-linear approximation using single-section equivalent circuit of a solar cell with a series resistance (Figure 2.2a). In accordance with the initial data and the formula (2.12), $R_s = 0.33$ Ω, and the illuminated I-V characteristic is presented by a line with one bend (line 3 in Figure 2.4). It is seen that calculation using the multisectional equivalent circuit of a solar cell provides the illuminated I-V characteristic shape with a smoothed bend even at the small number of sections. Let's continue analysis of the expression (2.19-2.22) with the aim of revealing generalities of the shape-formation of the illuminated I-V characteristics of a solar cell with distributed ohmic losses.

At $R_d = 0$ and $R_s \neq 0$ (lumped ohmic losses) from (2.21) a = 0, therefore at any n and j the expressions (2.20) and (2.19) give $I_{lj} = I_{ph}$, and from (2.22) we find $V_{lj} = V_{oc} - (2AkT/q) - R_s I_{ph}$. Thus the illuminated I-V characteristic is presented by a polygonal line with one bend, similar to the line 3 in Figure 2.4. At $R_d \neq 0$ but $I_{ph} \to 0$ the magnitudes of V_{lj} at any n and j tend to the value $V_{lj} = V_{oc} - (2AkT/q)$, since all magnitudes of I_{lj} tend to zero. It is self-evident that the case $I_{ph} \to 0$ is considered here only up to an illumination level at which the illuminated I-V characteristic of each diode of the equivalent circuit still admits its partial-linear approximation, since the magnitudes of V_{oc} depend on I_{ph} . To analyze the ohmic losses it is more convenient to examine the differences in voltage between V_{oc} and V_{lj} values

$$V_{oc} - V_{lj} = \frac{2AkT}{q} + \left(\frac{2j-1}{2n} R_d + R_s\right) I_{lj} - \frac{j(j-1)}{2n^2} R_d I_{ph} =$$

$$= \frac{2AkT}{q} + \left\{\left[\frac{2j-1}{2n} - \frac{j(j-1)}{2n^2}\frac{I_{ph}}{I_{lj}}\right] R_d + R_s\right\} I_{lj} \qquad (2.30)$$

In the latter expression the cofactor before I_{lj} can be considered as the net resistance characterizing the j^{th} bend point of the I-V characteristic. Denote it as R_j^{Σ}:

$$R_j^{\Sigma} = R_j + R_s = \left[\frac{2j-1}{2n} - \frac{j(j-1)}{2n^2}\frac{I_{ph}}{I_{lj}}\right] R_d + R_s \qquad (2.31)$$

where R_j is the characteristic resistance resulting from the action of only the distributed resistance R_d. From (2.19)-(2.21) and also (2.31) it is clear that the magnitudes of I_{lj} and of R_j don't depend on R_s and are the functions of the generalized dimensionless argument $qI_{ph}R_d/2AkT$. It is interesting to note that the dependences of the relative values $I_{lj}/I_{ph} = f\left(qI_{ph}R_d/2AkT\right)$ and

$R_j/R_d = f\left(qI_{ph}R_d/2AkT\right)$ bear a universal character, and their plots may be used for construction of the illuminated I-V characteristic of a solar cell at any magnitudes of I_{ph}, R_d, A and T (if only the p-n junction I-V curve can be presented as the partial-linear approximation).

Figure 2.5 shows the dependences I_{lj}/I_{ph} and R_j/R_d, obtained for n = 5. Figure 2.6 shows a set of the illuminated I-V curves constructed in coordinates $(V_{oc} - V_l) \rightarrow I_l$ at: I_{ph} = 2, 10 and 20 A; R_d = 0.1 Ω; R_s = 0.01 Ω; A = 1; T = 300 K; n = 5.The origin of the coordinates corresponds to the open circuit condition, and the point with abscissa V = V_{oc} (marked by crosses) correspond to the short circuit regime. Till the points V = V_{oc} lie on the horizontal segments of the illuminated I-V curves, i.e. at the level I_{ph}, the trajectory of their motion, as I_{ph} increases, is described by the forward branch of the dark I-V characteristic of the p-n junction (dashed curve d). But if the last bend point of the dark I-V curve lies beyond V_{oc}, the short circuit current point lies below I_{ph} (i.e. $I_{sc} < I_{ph}$) and is constructed in such a way as is shown in Figure 2.6 by the curve c. From Figure 2.5a the current coordinates of the five bend points were defined at given I_{ph}, and then the voltage coordinates were calculated using (2.30). In decreasing I_{ph} the motion trajectories of the bend points draw towards the point $2AkT/q = 0.052\ V$ on the voltage axis. Just here the lines of the characteristic resistances R_j^{Σ} (formula (2.31)) originate. However, since R_s is a constant (straight line 1' in Figure 2.6) and R_j^{Σ} vary only slightly with illumination (Figure 2.5b) the bend point trajectories (lines 1-5 in Figure 2.6) can be represented by straight lines.

It is important that the motion trajectories of the first and last bend points of the illuminated I-V curves are straight lines even in the case of an infinite number of chain sections. Indeed, as $n \rightarrow \infty$ it follows from (2.30) that

$$V_{oc} - V_{l1} = \frac{2AkT}{q} + R_s I_{l1} \tag{2.32}$$

$$V_{oc} - V_{ln} = \frac{2AkT}{q} + \left(\frac{1}{2}R_d + R_s\right) I_{ph} \tag{2.33}$$

The first bend point trajectory at $n \rightarrow \infty$ is presented by the line R_s (the straight line 1' in Figure 2.6), and the last bend point trajectory by the line $(1/2)R_d + R_s$ (the straight line 5 in the same figure). The coordinate I_{l1} at $n \rightarrow \infty$ can be approximately defined as the point of intersection of the straight line 1' with the illuminated I-V curve at the finite number of chain sections. The relative magnitudes of I_{l1} / I_{ph} at $n \rightarrow \infty$ are shown by the dashed curve 1' in Figure 2.5a. Thus, if in this figure the abscissa is now considered as an axis of intensities of illumination (being proportional to I_{ph} at other unvariable parameters), one may distinguish three regions. The region of "low" illumination levels (from the

point of view of action of R_d) extends as far as I_{lj} values are considered to be approximately equal to I_{ph}. The illuminated I-V curves have a shape of "an exponent with a series resistance" (2.13). In the region of "medium" illumination levels the value of I_{l1} is noticeable in comparison with the I_{ph} value. The I-V curve is conventionally divided into two parts by the first bend point, the lower "exponential" part from $I_l = 0$ to I_{l1} and the upper part from I_{l1} to I_{ph} deformed due to the action of R_d. Finally, in the region of "high" illumination levels, all values I_{lj} tend towards the magnitude $(j/n)I_{ph}$. One can verify this by considering partial solutions I_{lj}, for example the expression (2.28) at $a \to \infty$. R_j values tend towards the magnitudes $(j/2n)R_d$ (see formula (2.31)). In this case an analytical expression for the illuminated I-V curve can be found as follows. Let's rewrite the expression (2.22) for V_{lj} under the $n \to \infty$ condition and at j-magnitudes comprising a noticeable part of n:

$$V_{lj} = V_{oc} - \frac{2AkT}{q} - \left(\frac{j}{n}R_d + R_s\right)I_{lj} + \frac{j^2}{2n^2}R_d I_{ph} \tag{2.34}$$

The derivative dV_l / dI_l has a sense of resistance, the graph of which is a tangent line to the I-V curve. At the j^{th} bend point of the I-V curve we can define this value as

$$\frac{dV_l}{dI_l} = \frac{V_{lj} - V_{l(j+1)}}{I_{lj} - I_{l(j+1)}} = -\left(\frac{j}{n}R_d + R_s\right) \tag{2.35}$$

if we use the formula (2.34) and the fact that under strong illumination $I_{lj} = (j/n)I_{ph}$. It is obvious that $dI_l = \left(I_{ph}/n\right)dj$ and the boundary condition $V_l = V_{oc} - (2AkT/q) - \left(\frac{1}{2}R_d + R_s\right)I_{ph}$ at j = n (see formula (2.33)). Then after integrating (2.35) we obtain

$$V_l = -\frac{R_d I_{ph}}{2n^2}j^2 - \frac{R_s I_{ph}}{n}j + C \tag{2.36}$$

where the integration constant $C = V_{oc} - (2AkT/q)$. Finally

$$V_l = V_{oc} - \frac{2AkT}{q} - \frac{R_d}{2I_{ph}}I_l^2 - R_s I_l \tag{2.37}$$

or in the form of dependence of current on voltage:

$$I_l = \left[\frac{R_s^2}{R_d^2}I_{ph}^2 + \frac{2I_{ph}}{R_d}\left(V_{oc} - \frac{2AkT}{q} - V_l\right)\right]^{1/2} - \frac{R_s}{R_d}I_{ph} \tag{2.38}$$

The latter expressions are valid within the interval $V_{in} < V_l < V_{oc} - (2AkT/q)$. At $R_s = 0$ the formula (2.38) corresponds to the expression $I_l = f(V_l)$ contained in publications [23, 24] with the aim of allowing for the action of R_d in the limiting case $R_d \to \infty$ (which is similar to our case $I_{ph} \to \infty$). To complete the consideration of the joint effect of the sheet (distributed, R_d) and contact (series, R_s)

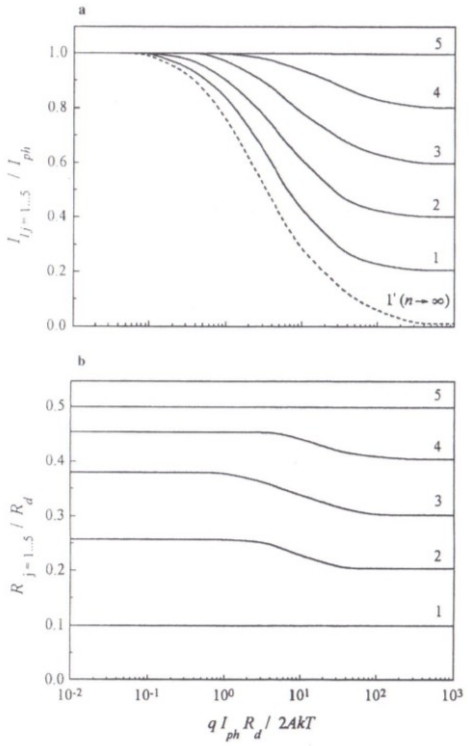

Figure 2.5 Dependences of the values I_{ij} / I_{ph} and R_j / R_d on the generalized argument $qI_{ph}R_d / 2AkT$ for a five-section solar cell equivalent circuit. The curve numbers correspond to the values of the index j. Curve 1' is the dependence of I_{l1} / I_{ph} at $\boldsymbol{n \to \infty}$

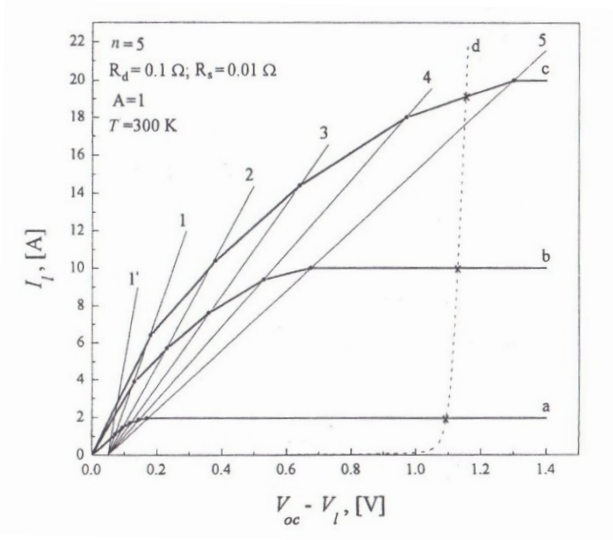

Figure 2.6 a, b and c – A family of illuminated I-V characteristics in the coordinates $(\boldsymbol{V_{oc} - V_l}) \to \boldsymbol{I_l}$ for a modeled gallium arsenide solar cell at I_{ph} = 2, 10 and 20 A, and d – "dark" I-V characteristic of the p-n junction in a solar cell. The slopes of the lines 1-5 correspond to the values $\boldsymbol{R_j^{\Sigma}}$ by the formula (2.31), the slope of the line 1' corresponds to the value R_s

resistances on the shape of the I-V characteristic of a solar cell we should notice that the obtained formulae (2.32), (2.33) and also (2.35) will be useful in the subsequent discussion of the procedures

for measurements of the distributed and lumped resistance components.

2.3 EXPERIMENTAL MEASUREMENT OF THE DISTRIBUTED AND LUMPED RESISTANCE COMPONENTS

The illuminated I-V curve of a solar cell with internal ohmic losses may be represented as the I-V characteristic of the p-n junction deformed by voltage drops across the internal resistance components. That is why the parameter A is involved in the formulae (2.28)-(2.30) for the current and voltage coordinates. It reflects the contribution of the p-n junction I-V characteristic shape to the resulting I-V curve shape of a solar cell.

To define the internal resistance components from the measured I-V curve of a solar cell, one should eliminate the uncertainty due to the unknown parameter A at different magnitudes of the current through the p-n junction. Fortunately, as has already been pointed out in the discussion of Figure 2.2, the p-n junction I-V characteristic of a real solar cell can be constructed as the dependence $I_{ph}^{'} = f\left(V_{oc}^{'}\right)$ for a given solar cell in varying illumination from zero level up to the level providing the required magnitude of I_{ph}. Thus, we shall assume that the p–n junction I-V characteristic coordinates are known to us. In connection with this, to find the values of R_d and R_s it would be more appropriate to analyze not the shape of the solar cell I-V curve itself but the shape of a "resistance curve", which would be constructed by subtraction of the voltage coordinates of the illuminated or dark I-V curve of the solar cell from those of the p-n junction at the same values of flowing current. Remember that the "resistance curve" is a straight line in the case of the series resistance model of a solar cell (see Figure 2.2). Let's consider the behavior of the "resistance curve" in the case of simultaneous action of lumped and distributed components of the internal resistance when the illumination intensity is varied.

As has been pointed out when deducing the formula (2.33), the voltage coordinate of the last bend point of the illuminated I-V curve at the I_{ph} level doesn't depend on a chosen number n of the equivalent circuit sections. Hence the voltage coordinate of the corresponding point of the "resistance curve", which we denote as ΔV_{ln}, also doesn't depend on n. Magnitudes of ΔV_{ln} at different illumination intensities can be found from the expressions (2.17) and (2.33):

$$\Delta V_{ln} = -\left(\frac{1}{2}R_d + R_s\right)I_{ph} \tag{2.39}$$

The expression (2.39) describes the "resistance curve" chord. The chord slope corresponds to the resistance magnitude $\frac{1}{2}R_d + R_s$. It doesn't depend on n nor on illumination intensity and may be used for obtaining R_d and R_s values as a first equation.

In principle, as a second equation for obtaining R_d and R_s, one may use the "one third rule" (2.12) valid at low illumination intensities. The expression (2.12) can also be obtained by analysis of the multisectional circuit of a solar cell used in our consideration. In our case the condition of "low" illumination is the location of all bend points of the illuminated I-V curve, as well as those of the "resistance curve", near the level I_{ph} (see Figure 2.5a). Considering the numerical example in Figure 2.7 for a hypothetical GaAs-based solar cell, one may notice that the bend points don't merge into one point, and that the actual "resistance curve" consists of two straight line segments (see the "resistance curve" "a" in the insert of Figure 2.7 for I_{ph} = 0.5 mA). In this case the straight line connecting the origin of coordinates and the first bend point may be considered as the I-V characteristic of an internal series resistance of a solar cell. Solving the equation set (2.20) in I_{ll} and V_{ll} and using (2.17), one may show that the slope of this line corresponds to $\frac{19}{54}R_d + R_s$ at n = 3, to $\frac{17}{50}R_d + R_s$ at n = 5 and tends, undoubtedly, to $\frac{1}{3}R_d + R_s$ at $n \to \infty$. Unfortunately, in experimental practice of measurement of the internal resistance components the "one third rule" presents difficulties in use, since high accuracy in the voltage measurements is required to construct the "resistance curve".

In connection with this, let's consider the possibilities of use of the "resistance curve" constructed from dark I-V curves of a solar cell and of the p-n junction (line "e" in Figure 2.7). It is apparent that the "dark resistance curve" has a slope in the origin corresponding to the value $\frac{1}{3}R_d + R_s$, because the "low" illumination conditions are identical to the "low" forward current conditions. However, as the forward bias increases, the current ceases to flow over the whole light-sensitive area of the solar cell, but will tend to pass the p-n junction directly under the contact strip. To describe this case, one should introduce into the circuit of Figure 2.2 one more diode between R_s and the rest of the sections, which identifies the solar cell area covered by the contact strip. It is clear that in the case of the large forward currents the slope of the "dark resistance curve" will tend to the value corresponding to R_s (see Figure 2.7), which could be used for independent measurement of the R_s magnitude. Unfortunately, running ahead, we should notice that the practical cells have a design of a contact strip on the light-sensitive surface such that narrow grid fingers are connected in a solar cell outlying area by means of a wide current-collecting bar. The presence of this bar has almost no effect on the shape of the illuminated I-V curve of the solar cell. Owing to this, a solar cell with the contact grid in the form of parallel strips can be considered as a definite number of the smaller solar cells of the simplest geometry (Figure 2.2) connected electrically in parallel. However, in the dark, at a sufficiently high forward bias at the p-n junction, the main fraction of the current flows directly under the wide current-collecting bar, and the measured magnitude of R_s appears to be an understated one.

The other possibility of obtaining information about the lumped internal resistance component of a solar cell arises from a "high" illumination level condition. In this case the slope of a straight line

connecting the origin of coordinates and the first bend point of the "resistance curve" tends to a value corresponding to $\frac{1}{2n}R_d + R_s$, i.e. to R_s . It means that the magnitude of R_s could be obtained from the slope of the tangent to the "resistance curve" at the origin of coordinates, as is shown in Figure 2.7 regarding the curve "d" for I_{ph} = 1000 mA. Thus this is a method of independent measurement of R_s . But in practice the "resistance curve" has a rather sharp curvature at the origin point so the accuracy of tangent construction is not so high. That is why we shall investigate the other possible way of producing an alternative equation to the expression (2.39) connecting the components R_d and R_s . Let's construct a tangent line to the illuminated "resistance curve" at the current value equal to I_{ph}. This is a straight line through the last (j = n) and the next to last (j = n – 1) bend points of this curve under $n \to \infty$ conditions. For the next to last bend point of the illuminated I-V curve we have, from the equation set (2.20) the single line

$$(1 + a)I_{n(n-1)} = \frac{1}{n}I_{ph}$$

Substituting this in (2.19), we obtain the current coordinate of the next to last bend point

$$I_{l(n-1)} = I_{ph}\left[\frac{n-1}{n} + \frac{1}{n(1+a)}\right]$$

and then the voltage coordinate $V_{l(n-1)}$ from (2.22). The cotangent of the slope angle of the tangent line to the "resistance curve" is defined by the ratio $\left(\Delta V_{ln} - \Delta V_{l(n-1)}\right)/\left(\mathrm{I_{ph}} - \mathrm{I_{l(n-1)}}\right)$ where $\Delta V_{l(n-1)}$ is the difference in voltage between corresponding points on the illuminated I-V curve $V_{l(n-1)}$ and on the p-n junction characteristic at one and the same current $I_{l(n-1)}$. Using for the p-n junction I-V characteristic its partial-linear approximation we obtain:

$$\frac{\Delta V_{ln} - \Delta V_{l(n-1)}}{I_{ph} - I_{l(n-1)}} = \left(1 - \frac{1}{2n}\right)R_d + R_s + (n-1)\frac{2AkT}{I_{ph}} \qquad (2.40)$$

Analysis of expression (2.40) shows that at an infinite number n of the equivalent circuit sections the slope of the tangent line corresponds to an infinite resistance, i.e. the "resistance curve" always has a horizontal segment at the level I_{ph}. The length of this segment is relatively large at low illumination levels (on the insert of Figure 2.7 it is, in fact, the whole segment of the curve "a" between the first and the last bend points) and decreases when illumination is increased. However the practical procedure of the "resistance curve" construction does not reveal this portion, since the real I-V characteristic of the p-n junction and that of the solar cell as a whole have a smooth transition of their tilted branches to horizontal ones at the level I_{ph}. This means that the accuracy of measurements of voltages and currents feasible in the experiment may be considered as if it sets a limited number n in the solar cell model. Therefore, in the expression (2.40) the last addition actually decreases with I_{ph}, and the whole expression tends to the value $R_d + R_s$ when illumination is increased. In Figure 2.7 the

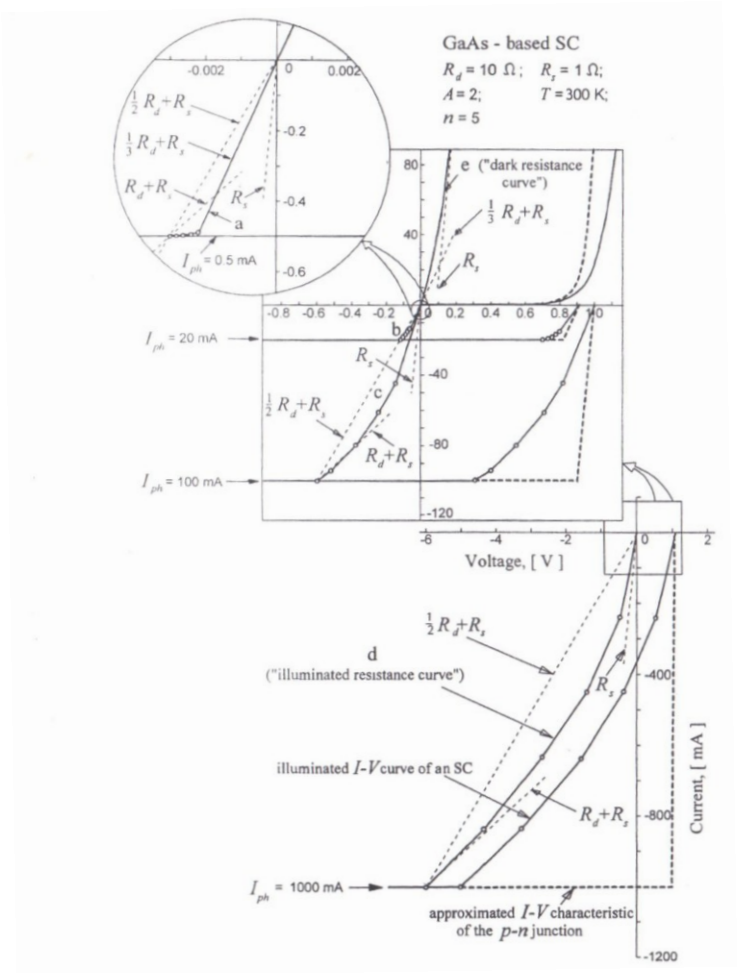

Figure 2.7 A general chart of the shape variation of the I-V characteristics and "resistance curves" for a "classic" geometry GaAs-based solar cell in varying illumination intensity (lines a, b, c and d have been constructed for I_{ph} values of 0.5, 20, 100, and 1000 mA, respectively). The line e is the "resistance curve" for the dark I-V characteristic

tangent lines with the slopes corresponding to this value are also indicated.

The expressions (2.39) and (2.40) can serve as a basis for measurements of R_d and R_s, as has been proposed in the work [28]. The measuring procedure is as follows. At reasonably high illumination intensity resulting in an obvious deformation of the I-V curve of the solar cell due to the action of the internal resistance components, the "resistance curve" is constructed. The slope of this curve chord corresponds to the value $\frac{1}{2}R_d + R_s$, and the slope of the tangent line to this curve at the current level I_{ph} corresponds to the value $R_d + R_s$. Specimens of GaAs- and Si-based solar cells with strip contacts have been experimentally studied. The value of R_d and R_s obtained from measurements by the technique described above and from direct electrical measurements by the conventional four-probe technique were compared. For the electrical measurements additional contact strips were prepared on the light-sensitive solar cells surface. The metering circuit for the solar cell on the basis of GaAs is presented in Figure 2.8a. Figure 2.8b shows construction of the illuminated characteristic of the p-n

junction and construction of the “resistance curves” at two I_{ph} magnitudes for that cell. The illuminated I-V curves were recorded at both forward and reverse biases using only one of the edge strip contacts. Independent electrical measurements of R_d and R_s were carried out without illumination and without voltage bias applied to the p-n junction. When current flowed along the front region of the p-n junction, a quarter fraction of the value of R_d and then the doubled value of R_s were measured.

It is seen from Figure 2.8b that both “resistance curves” have one and the same chord and similar slopes of the tangent lines at the I_{ph} levels. The calculated magnitudes of the distributed and lumped resistances of the solar cell were R_d = 56 Ω and R_s = 7.3 Ω. These results are in reasonable agreement with the results of the electrical measurements of the sheet and contact resistances by means of

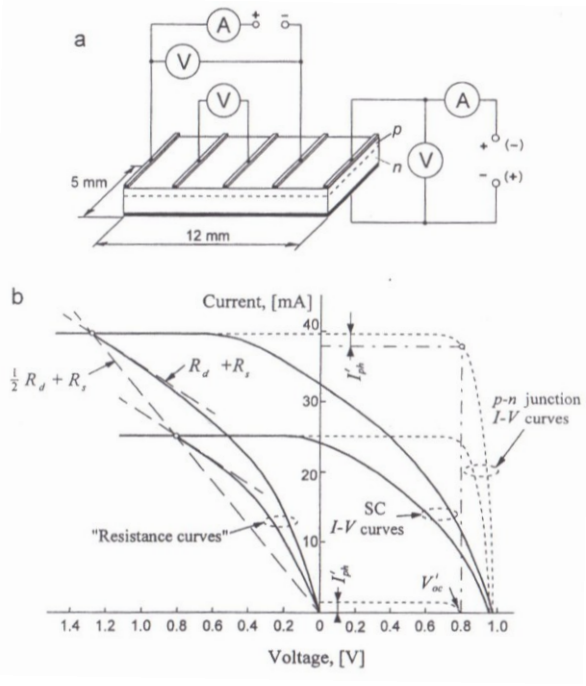

Figure 2.8 a – Design of a GaAs-based solar cell specimen with electric circuits for measurement of R_d , R_s and illuminated I-V curves, and b – illuminated I-V characteristics and the “resistance curves” at two illumination intensities [25]

the four-probe technique: R_{sh} = 62.4 Ω and R_c = 8.4 Ω. Thus, the technique of measurements of R_d and R_s proposed in [28] and considered above actually allows us to evaluate the distributed and lumped components of the solar cell internal resistance.

2.4 RESISTANCE OF THE METALLIC CONTACT GRID

Let us consider a more complicated problem consisting in the additional influence of the distributed resistance of the metallic contact grid on the shape of the solar cell illuminated I-V curve.

The solar cell geometry and corresponding equivalent circuit for the calculations are presented in Figure 2.9 [27]. We suppose that the solar cell dimension along the contact strip is much larger than

the transverse dimension, which allows us to discount the shunting effect of the semiconductor sheet resistance with respect to the longitudinal metallic strip resistance R_M. Thus, the photocurrent will flow through the solar cell front region in the direction perpendicular to the contact strip. The sheet resistance value R_{sh} in Figure 2.9 is determined in the same manner as R_d in Figure 2.3. The contact resistance R_c characterizes the whole area of the metallic strip.

To account for the effect of the second distributed component, the resistance R_M, the solar cell is divided into several equal parts, each represented by a special branch in the equivalent circuit.

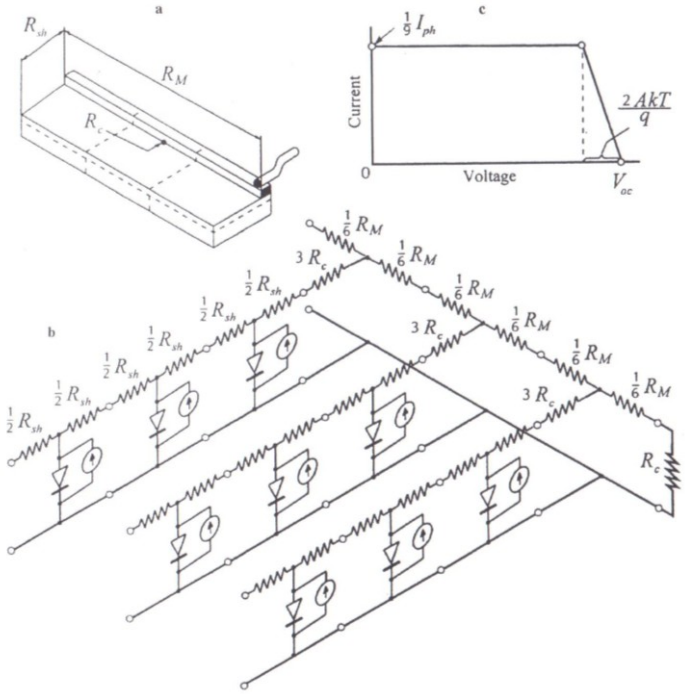

Figure 2.9 Geometry of a solar cell (a); its equivalent circuit accounting for the effect of the sheet resistance R_{sh} and of the resistance of a metallic contact strip R_M (b), and the partial-linear approximation of the illuminated I-V characteristic of one of the equivalent circuit diodes

The branches are connected to each other by corresponding portions of the resistance R_M. To account for the distributed resistance R_{sh}, each branch, by analogy with Figure 2.3, is composed of n sections (n = 3 in Figure 2.9). The resistance magnitudes on the equivalent circuit of Figure 2.9b correspond to nine similar rectangular parts of the solar cell under consideration. The partial-linear approximation of the illuminated I-V characteristic of every p-n junction part is shown in Figure 2.9c.

Calculation of the bend point coordinates of the solar cell net I-V characteristic should be begun by calculating the coordinates of the n bend points (corresponding to a number of chain sections) of the I-V characteristic of one of the equivalent circuit branches of Figure 2.9b. Necessary formulae can be obtained from (2.19)-(2.22) (or from (2.28) for n = 3) with the following replacements. The magnitude

$(1/m)I_{ph}$ should be substituted for I_{ph}, where m is the number of branches of the equivalent circuit. Instead of (2.21), the following expression has to be used:

$$a = \frac{1}{mn}\frac{qI_{ph}R_{sh}}{2AkT} \tag{2.41}$$

Then R_d and R_s are substituted by mR_{sh} and mR_c. The illuminated I-V characteristic of one of the three branches is represented by the polygonal line "a" in Figure 2.10.

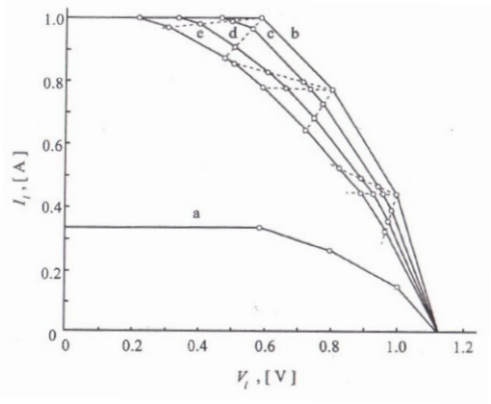

Figure 2.10 a – The illuminated I-V characteristic for one of the equivalent circuit branches in Figure 2.9b; b-e – illuminated I-V characteristics of a gallium arsenide solar cell at I_{ph} = 1 A, R_{sh} = 1 Ω, R_c = 0, A = 1. The magnitudes of R_M are, respectively, 0, 0.25, 0.5 and 0.75 Ω.

If R_M = 0, the net I-V characteristic of the solar cell has n bend points (line "b" in Figure 2.10). The numerical data of Figure 2.10 correspond to a GaAs-based solar cell of 1 cm^2 area: T = 300 K; I_{ph} = 1 A; A = 1; R_{sh} = 1 Ω; R_c = 0. At $R_M > 0$ the bend points of the illuminated I-V characteristic of individual branches are located at different voltages, therefore the net I-V characteristic of the solar cell has mn bend points. These points shift with increasing R_M. The trajectories of these shifts are shown in Figure 2.10 by dashed lines. The illuminated I-V characteristics "c", "d" and "e" correspond to the values of R_M equal to 0.25, 0.5 and 0.75 Ω, all other parameters being constant. Calculation of the bend points are reported for the equivalent circuit containing three branches. The Kirchhoff equations solution is related to the case when the trajectories of adjacent points do not intersect. The following expressions have been obtained [27]:

$$I_{lj1} = I_{lj}\left(1 + \frac{2 + a_j}{1 + 3a_j + a_j^2}\right)$$

$$V_{lj1} = V_{lj} - I_{lj1}\frac{R_M}{6}$$

$$I_{lj2} = I_{lj}\left[\left(1+\frac{1}{1+a_j}\right)(1+a_{j+1})+1\right]$$

$$V_{lj2} = V_{lj} - \frac{R_M}{6}\left[2I_{lj}\left(1+\frac{1}{1+a_j}\right)+I_{lj2}\right] \qquad (2.42)$$

$$I_{lj3} = I_{lj}\left(3+4a_{j+1}+a_{j+1}^2\right)$$

$$V_{lj3} = V_{lj} - I_{lj}\frac{R_M}{6}\left(9+6a_{j+1}+a_{j+1}^2\right)$$

Here the index j is the bend point number in illuminated I-V characteristic of the branch, counting from the point V_{oc}: j = 1, …, n; the values I_{lj} and V_{lj} are the coordinates of the bend points in this characteristic; and $a_j = (R_M/3)\left(I_{lj} - I_{l(j-1)}\right)/\left(V_{l(j-1)} - V_{lj}\right)$ is the ratio of the resistance of a metallic strip part, corresponding to one branch, to the dynamic resistance of this branch between the points j – 1 and j. The magnitude of j – 1 = 0 corresponds to the horizontal segment of the branch I-V characteristic ($a_{n+1} \equiv 0$). Some similarity of the expressions (2.42) and (2.28) is observed. The expressions (2.42) are more complicated, since in this case the initial I-V characteristic of the branch (Figure 2.10, line "a") has a more complicated shape than that of one section in Figure 2.9c. The last bend point coordinates at n = 3 are the following:

$$I_{l33} = I_{ph}$$

$$V_{l33} = V_{oc} - \frac{2AkT}{q} - \left(\frac{R_M}{2}+\frac{R_{sh}}{2}+R_c\right)I_{ph} \qquad (2.43)$$

We can conclude from (2.43) that the slope of the "resistance curve" chord actually also reflects the longitudinal resistance of the metallic contact strip. However, it is impossible to obtain relationships allowing us to separately evaluate two distributed components of the internal resistance. Such a condition can arise only as a result of the strongly non-uniform illumination of the solar cell area.

2.5 EFFECTIVE DISTRIBUTED AND EFFECTIVE SERIES RESISTANCES

In designing cells for highly concentrated sunlight one should take account of the conditions of optically matching a solar cell with a concentrator, and providing at the same time the internal resistance to be as low as possible. Since the concentrators characterized by a high magnitude of concentration ratio usually form the round image of the Sun, solar cells with a round light-sensitive area would be appropriate for use in this case. The shortest path for the photocurrent collected from a

round area is that through the radial strips. The photosensitive area is surrounded by a current-collecting bus, to which a copper lead is soldered. To arrange the radial strips at approximately equal distances from each other (optimal from the point of view of collecting the photocurrent over the semiconductor area between them) they are made in the form of lengths between several concentric strips. The grid resistance often appears to be a limiting factor in attempting to increase the device output. Let us first consider the special features of the equivalent circuit of a solar cell with the radial-circular contact grid, as has been done in [25].

A three-section equivalent circuit with such a grid is depicted in Figure 2.12. The round geometry solar cell may be regarded as consisting of sectors connected in parallel. That is why the whole solar cell may be considered as a single generalized sector. It is supposed that the sector surface is uniformly covered by a metallic contact grid characterized by the metal resistance R_M and by the contact transient resistance R_c. The photocurrent flows to the busbar collector in radial directions. Each lumped diode of the equivalent circuit is located in the geometrical center of each of the three equal-area parts of the sector (these parts are indicated in Figure 2.12 by dashed lines). Under uniform illumination all current sources generate photocurrents of the same magnitude $(1/3)I_{ph}$. The current flows through the resistances $3R_c$ before entering the metallic grid. A characteristic feature of the multisectional equivalent circuit of the round geometry solar cell in comparison with those from Figure 2.3 or Figure 2.9 is that different portions of the distributed resistance R_M are included in different sections. Indeed, when the radial current approaches the busbar collector, the metallic grid resistance decreases owing to both shortening of the distance for current flow and increasing the width of the grid. Distribution of R_M in the circuit of Figure 2.12 is calculated from the corresponding geometrical consideration.

For a given magnitude of the longitudinal specific resistance of the metallic strips and at a fixed grid "density", the value of R_M does not depend on the radius r of the solar cell light-sensitive area. One recalls that in the case of the rectangular geometry solar cell (Figure 2.1a) the value of R_d depends on the ratio of the length of the semiconductor layer to its width, rather than on absolute dimensions of the solar cell. In the same manner R_M depends on the ratio of the effective length of the sector to its width. The sector in Figure 2.12 represents the whole area of a round solar cell, and the ratio of the radius to the length of a circle is, as is known, a constant value.

For unlimited increase of the number of sections n, in the equivalent circuit of Figure 2.12, the point of connection of the last lumped diode (counting from the load resistance side) shifts towards the solar cell center. The resistance dR of an element of a flat ring of width dx and of radius x for the current, flowing in the radial direction, is proportional to $dx/2\pi x$, i.e. $R \sim ln(x_2/x_1)$; where x_1 and x_2 are the inner and outer radii of the ring, respectively. Hence, the net chain resistance value between the last diode point and the load resistance tends to infinity.

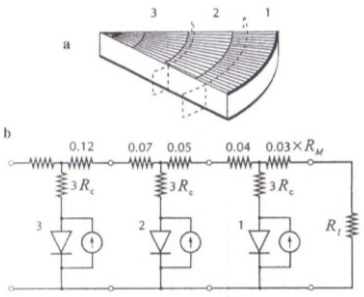

Figure 2.11 A generalized sector of a round geometry solar cell (a), and its three-section equivalent circuit (b)

For this reason the understanding of the absolute value of R_M is a matter of convention. For further consideration we shall take the values of the coefficients at R_M as proposed in [25]. These values are presented in the circuit of Figure 2.11. In the case of a three-section equivalent circuit, the areas equal to 1/6 of the total solar cell area have to be situated on both sides of the lumped diode. Therefore, one may show by calculation that the connection point of the last diode is located at a distance of $0.41r$ from the solar cell center. Thus, the value $0.31R_M$ could be measured on a real solar cell as a resistance between the outer collecting bus and a metallic ring, applied concentrically on the contact grid and characterized by a diameter equal to 0.41 of the bus diameter.

The calculation of the bend point coordinates of the illuminated I-V characteristic is carried out on the basis of the set of Kirchhoff equations. Uniform illumination is assumed.

Before presenting the final formulae we shall make one remark. It concerns the accuracy of representation of the I-V characteristic shape by discrete coordinates in the case when the voltage drop across the distributed resistance components is close to zero. It is apparent that at zero distributed losses all bend points of the I-V characteristic draw into one point at the level I_{ph}, so that the characteristic shape becomes similar to the line 3 in Figure 2.4. Calculation of the solar cell maximum output power from such an I-V characteristic gives a noticeable error, in contrast with a situation when this value is obtained from "the exponential I-V characteristic with a series resistance" (2.13).In [22] a simple expedient is proposed to decrease this error. The last bend point of the I-V characteristic is simply separated into two points: one point at the level I_{ph} but shifted in voltage farther from V_{oc} by the value $(2AkT)/q$, and another point at the level 0.95 I_{ph} and at the calculated value of voltage. In this case the I-V characteristic calculated for the three-section equivalent circuit has four bend points. Thus, the formulae for coordinates of these four points of the I-V characteristic for the round solar cell are:

$$I_{l1} = 0.33 I_{ph} \left[1 + \frac{2 + \frac{0.063 R_M}{R_c + R_D}}{\frac{0.091 R_M}{R_c + R_D}\left(1.3 + \frac{0.018 R_M}{R_c + R_D}\right) + 1} \right]$$

$$V_{l1} = V_{oc} - \left[0.03 R_M I_{l1} + (R_c + R_D) I_{ph}\right] \tag{2.44}$$

$$I_{l2} = 0.33 I_{ph} \left[2 + \frac{1}{1 + (0.063 R_M)/(R_c + R_D)} \right]$$

$$V_{l2} = V_{oc} - \left[0.11 R_M I_{l2} + (R_c + R_D - 0.027 R_M) I_{ph}\right]$$

$$I_{l3} = 0.95 I_{ph}$$

$$V_{l3} = V_{l2} - \frac{0.17 R_M \left(0.95 I_{ph} - I_{l2}\right)\left(I_{ph} - 0.64 I_{l2}\right)}{I_{ph} - I_{l2}}$$

$$I_{l4} = I_{ph}$$

$$V_{l4} = V_{oc} - (0.15 R_M + R_c + 2 R_D) I_{ph}$$

In the formula (2.44) the notation

$$R_D = 2AkT/qI_{ph} \tag{2.45}$$

is introduced, corresponding to the magnitude of the mean differential resistance of the p-n junction area at the photocurrent I_{ph}.

It is interesting to compare the shapes of the illuminated I-V characteristics calculated for equivalent circuits of the rectangular and round solar cells. In both cases we take R_c =0. Then the contact grid on the surface of a round solar cell (Figure 2.11) can be considered merely as some distributed resistance, similar to a sheet resistance in the case of a rectangular solar cell (Figure 2.3). Line 1 in Figure 2.12 represents the partial-linear approximation of an ideal illuminated I-V characteristic of the p-n junction in a solar cell; line 2 represents the I-V characteristic at the presence of ohmic losses in the lumped series resistance; line 3 represents the I-V characteristic at the presence of only distributed losses in a solar cell of rectangular geometry; and line 4 represents the I-V characteristic at the presence of only distributed losses in a solar cell of round geometry. Initial data for calculations were chosen such that the last bend points of the I-V characteristic at the level I_{ph} coincided. The artificial separation of the last bend point into two, at the level I_{ph} and at the level $0.95 I_{ph}$, is shown for all characteristics by a

dashed line. From comparison of the I-V characteristics of 2-4 it is clear that the distributed character of the ohmic losses results in a more convex shape of the I-V characteristic than can be obtained on the basis of analysis of a single-section equivalent circuit of a solar cell with a series resistance. However, the illuminated I-V characteristic for a round solar cell is more convex than that for a rectangular solar with a linear busbar contact.

The question arises whether one may propose formulae for calculation of discrete coordinates of the illuminated I-V characteristic valid for solar cells of any geometry. These formulae could be used for prediction of the I-V characteristic shape when the illumination level is increased. For example, the lines 2 and 4 in Figure 2.12 are calculated by the formulae (2.44) at purely lumped or purely distributed character of internal ohmic losses. It is apparent that at some values of R_c and R_M one may obtain by the formulae (2.44) an

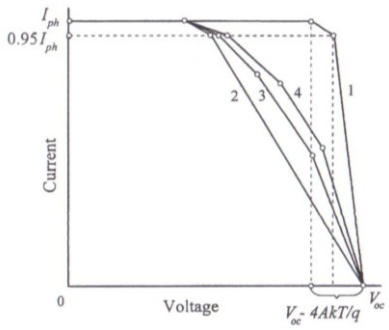

Figure 2.12 Comparison of illuminated I-V characteristics of a solar cell at zero ohmic losses (1); pure lumped losses (2); pure distributed losses in a rectangular geometry of a solar cell (3); and pure distributed losses in a round geometry of a solar cell (4)

illuminated I-V characteristic close in shape to the line 3. It means that purely distributed ohmic losses in a rectangular solar cell can be evaluated by some effective resistances, distributed resistances and lumped (series) resistances. Denote them as R_d^* and R_s^*. Also it is clear that it is impossible to obtain the line 4 of Figure 2.12 by the formulae for the I-V characteristic coordinates of a rectangular solar cell, because at purely distributed losses we have the line 3, and in introducing any lumped resistance the I-V characteristic would be closer to the line 2.

Thus, at an arbitrary geometry of a solar cell the calculation of the illuminated I-V characteristic coordinates by the formulae (2.44) using R_s^* instead of R_c and R_d^* instead of R_M should be considered as the way of construction of an I-V characteristic which is more convex than that constructed by the model of a solar cell with purely series resistance. Nevertheless, this way is physically justified, since account is taken of changes in shape of the illuminated I-V characteristics of the diodes comprising the equivalent circuit as illumination increases. The fitness of the I-V characteristic construction procedure proposed in [25] is confirmed by the calculated plots of Figure 2.13 [27]. Here the open

circles on the lines 1 and 2 are the discrete coordinates of the illuminated I-V characteristic of the hypothetical GaAs-based solar cell for I_{ph} = 0.5 A and 1 A calculated by the formulae (2.42) at R_c = 0, R_{sh} = 1 Ω, R_M = 0.75 Ω. The black points are the results of calculation by the formulae (2.44) at $R_s^* = 0.38\,\Omega$ and $R_d^* = 3.17\,\Omega$. It is seen that even under the "double distributed losses" conditions (when both resistances R_{sh} and R_M are in operation) there exists the possibility to accurately predict deformation of the solar cell I-V characteristic shape for increasing illumination level.

However, such a prediction is possible only when R_s^* and R_d^* are known parameters. The following procedure has been suggested in [25] for evaluation of these parameters from an experimental illuminated I-V characteristic. Two horizontal lines are plotted on the I-V characteristic diagram at the levels $0.95\,I_{ph}$ and $0.5\,I_{ph}$.

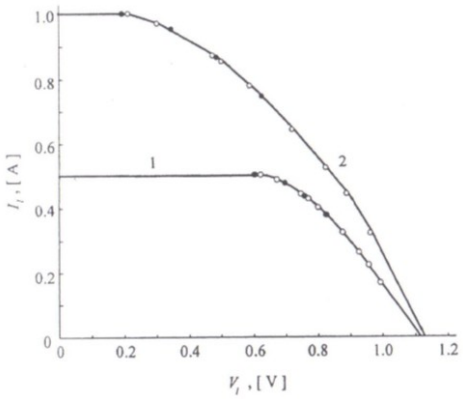

Figure 2.13 Illuminated I-V characteristics of a gallium arsenide solar cell at I_{ph} = 0.5 A (1) and I_{ph} = 1 A (2). The open circles represent calculation by the formulae (2.42) for a rectangular solar cell at R_c = 0, R_{sh} = 1 Ω, R_M = 0.75 Ω, and the dark circles represent calculation by the formulae (2.44) for a round solar cell at $\boldsymbol{R_s^* = 0.38\ \Omega}$ and $\boldsymbol{R_d^* = 3.17\ \Omega}$

Then through the point V_{oc} and the points of intersection of the horizontal lines with the I-V characteristic two straight lines are plotted. Cotangent values of the slope angles of these lines have a sense of resistance (denote them as $R_{0.95}$ and $R_{0.5}$). The magnitudes of $\boldsymbol{R_s^*}$ and $\boldsymbol{R_d^*}$ are defined from the following expressions:

$$\boldsymbol{R_d^* = 36\left\{0.62R_{0.5} - R_{0.95} + \left[(0.62R_{0.5} - R_{0.95})^2 - 0.4R_{0.95}(0.95R_{0.5} - R_{0.95})\right]^{1/2}\right\}}$$

$$R_s^* = 1.1R_{0.95} - 0.15R_d^* - \frac{2AkT}{qI_{ph}} \qquad (2.46)$$

The formulae (2.46) were obtained on the basis of geometrical consideration of the illuminated I-V characteristic plot constructed by calculated coordinates from the two-section equivalent circuit of a round geometry solar cell [25]. In these expressions the p-n junction I-V characteristic parameter A

(ideality factor) is present and that requires some additional measurements. Fortunately, in increasing the photocurrent density it tends to unity. For example, for a GaAs-based solar cell one may put A = 1, if $i_{ph} > 0.5$ A · cm^{-2} [29]. An example of the use of the formulae (2.44) and (2.46) is shown in Figure 2.14. The solid lines depict the experimental illuminated I-V characteristics of a round solar cell of 17 mm diameter with the nGaAs-pGaAs-pAlGaAs heterostructure and the radial-circular contact grid. The I-V characteristics were recorded under flash Xe-lamp illumination. To evaluate $R_{0.95}$ and $R_{0.5}$ parameters, the straight lines were constructed on the characteristic with I_{ph} = 100 A (curve 2). The values found were used in the formulae (2.46) to calculate effective values of R_s^* and R_d^*. These values were used instead of R_M and R_c in the formulae (2.44) for I_{ph} = 40, 100, 150 and 200 A. Corresponding values of V_{oc} were taken from experiment; A = 1; T = 300 K. Good agreement between calculated I-V characteristic bend points (marked in Figure 2.15) with the experimental curves was observed.

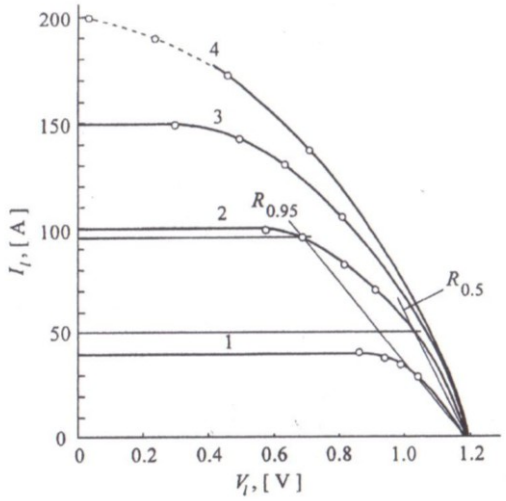

Figure 2.14 Experimental I-V characteristics of a gallium arsenide solar cell of 17 mm diameter under illumination by a flash lamp. Open circles represent I-V coordinates obtained from calculations by the formulae (2.44) at $R_M = \boldsymbol{R_d^*} = 2.4 \cdot 10^{-2}$ Ω and $R_c = \boldsymbol{R_s^*} = 1.8 \cdot 10^{-3}$ Ω, and straight lines represent construction of $R_{0.5}$ and $R_{0.95}$ resistances

Pursuing analysis of the solar cell operation on the basis of the equivalent circuit of Figure 2.11 we shall consider the effect of non-uniform illumination on the I-V characteristic shape. This matter is of great importance for the solar cells converting highly concentrated sunlight. As a rule, in this case every solar cell operates together with an individual concentrator-lens or parabolic mirror. Such a concentrator forms the round focal image of the Sun with the intensity distribution close to the axially symmetrical one. Under such conditions the solar cell center is, as a rule, illuminated more strongly than the peripheral areas are, resulting in an I-V characteristic shape different from that in the case of uniform illumination.

Let's consider the following situations. A photocurrent of one and the same magnitude is generated by

the central part of the solar cell comprising 1/3 or 2/3 of the total area; by the total area of the solar cell; by the peripheral part of the solar cell, when 1/3 of the area in the center is not illuminated. These situations are schematically depicted by the inset in Figure 2.15. An important feature of the solar cell operation under non-uniform illumination is the dependence of V_{oc} on the illumination distribution at the constant value of net photocurrent. Let only the center of the solar cell be illuminated, i.e. Section 3 in Figure 2.11. It is clear that under open circuit conditions the unilluminated diodes 1 and 2 will shunt the photocurrent. This means that a current flows along the contact grid towards the output leads. The voltage drop across the distributed resistance decreases V_{oc} at the device terminals, while the voltage at the diode 3 in this case is higher than the V_{oc} value under uniform illumination. Conversely, in illuminating only diode 1 the current flows in the opposite direction, so the increased voltage transfers directly to the solar cell terminals.

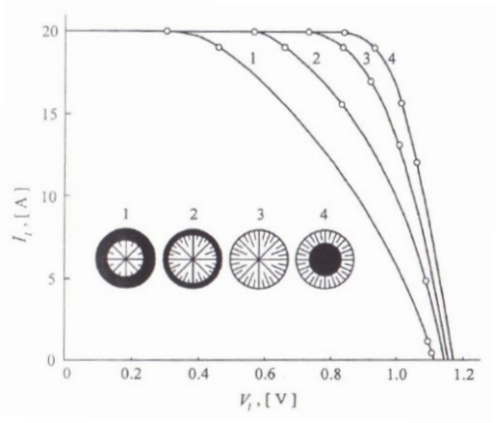

Figure 2.15 Experimental I-V characteristics of a high-current gallium arsenide solar cell of 17 mm diameter under illumination by a flash lamp through applied shadowing masks (see the insert). Open circles represent calculation results obtained on the base of the equivalent circuit of Figure 2.12

The curves 1-4 in Figure 2.16 represent the experimental I-V characteristics of the GaAs-based solar cell of 17 mm diameter at uniform illumination and various types of non-uniform illumination arranged with the use of the superimposed masks. This figure also shows the calculated points for V_{oc} and discrete coordinates of the I-V characteristic obtained on the basis of the equivalent circuit of Figure 2.12 (the formulae are not given due to their cumbersome character). It is seen that the non-uniformity of illumination has a strong effect on the output electric power, decreasing V_{oc} and the I-V characteristic fill factor at stronger illumination of the central area, and increasing them when only the peripheral areas are illuminated. If the R_d^* and R_s^* values are defined from the experimental I-V characteristic of the solar cell under non-uniform concentrated illumination, then the formulae (2.46) characterize the given solar cell together with the employed concentrator. Comparison of curves 3 and 4 in Figure 2.16 shows that the heightened illumination of the peripheral areas of a solar cell appears

to be more energetically beneficial than its uniform illumination. This gives a way for optimization of the sunlight concentrating system. It could be such a design where the distribution of illumination with a drop in the center would be formed. Such a distribution can be obtained, for instance, by employing sphero-torical and parabolo-torical mirrors [30] and also double-mirror systems or special Fresnel lenses. It is self-evident that such a way is justified only in the case when the longitudinal resistance of the contact grid constrains the solar cell output power. However, if constraining factors are the sheet resistance of the front semiconductor region or the contact resistance, then any local increase in the photocurrent density results in a decrease in output power, in contrast to the case of the solar cell uniform illumination.

2.6 CONVERSION EFFICIENCY OF SOLAR CELL WITH INTERNAL OHMIC LOSSES

The existence of internal ohmic losses is one of the reasons why the efficiency of a real solar cell differs from that predicted by theory. Let us analyze the influence of the ohmic losses on the solar cell efficiency. Choose as a measure of efficiency the ratio of the maximum output electric power P to the power P_0 which would be generated by this solar cell at the same illumination level if the internal ohmic losses were absent. It is implied that in both cases the photocurrent values are equal to each other. The optical and recombination losses concerned with photocurrent generation are not taken into account here.

Let us first consider the case of a solar cell with a pure lumped character of ohmic losses. The partial-linear approximations of the illuminated I-V characteristic of such a solar cell at $R_s = 0$ and at two magnitudes of $R_s > 0$ are pictured in Figure 2.16 (line a and lines b and c, respectively). It follows from geometrical consideration of the diagram that at small magnitudes of R_s the maximum power point lies at the I-V characteristic bend point. Considering the value $2AkT/q$ as negligibly small in comparison with V_{oc}, one may show that the conversion efficiency is defined by the expression

$$\frac{P}{P_0} = \frac{I_{ph}V_{l1}}{I_{ph}V_{l0}} \approx 1 - \frac{I_{ph}R_s}{V_{oc}} \tag{2.47}$$

At large values of R_s the maximum power point moves onto the slope portion of the I-V characteristic, so the voltage corresponding to this point becomes equal to $(1/2)V_{oc}$. For the range of magnitudes of $I_{ph}R_s \leqslant V_{oc}$ we get

$$\frac{P}{P_0} = \frac{I_{l2}V_{l2}}{I_{ph}V_{l0}} \approx \frac{1}{4}\frac{V_{oc}}{I_{ph}R_s} \tag{2.48}$$

It is easy to notice from the expressions (2.47) and (2.48) that to describe the function behavior P/P_0 one should choose the ratio $I_{ph}R_s/V_{oc}$ as a function argument.

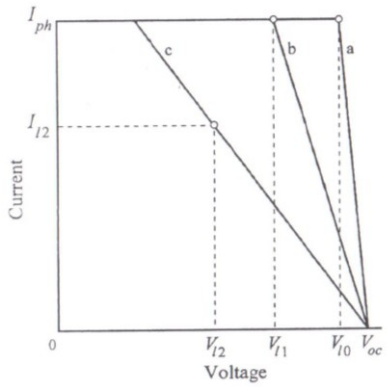

Figure 2.16 The partial-linear approximations of the illuminated I-V characteristics of a solar cell: a – $R_s = 0$; b, c – $R_s > 0$. Circles mark the maximum power points

Indeed, the dependence $P/P_0 = f\left(I_{ph}R_s/V_{oc}\right)$ bears the universal character describing the behavior of different types of solar cells for a wide range of illumination levels. For example, in a solar cell characterized by R_s = 0.1 Ω at I_{ph} = 1 A nearly the same portion of generated electric power is dissipated as in a solar cell with R_s = 0.01 Ω at I_{ph} = 10 A.

In general, to describe the ohmic losses in a solar cell with both the lumped and distributed components of the internal resistance, a number of dependences $P/P_0 = f\left[I_{ph}\left(R_s^* + R_d^*\right)/V_{oc}\right]$ can be constructed at different magnitudes of the R_s^*/R_d^* ratio. This has been done in the work [26] for the GaAs-based solar cells. The calculations have been carried out in the following way.

Each illuminated I-V characteristic is presented as consisting of segments of straight lines between points evaluated by the formulae (2.44) (Figure 2.17). The maximum power point has to coincide with the middle of the hypotenuse of the triangle formed by the continuation of one of the segments until it intersects the voltage and current axes. The magnitude of V_m is sought from the expression

$$V_m = \frac{1}{2}\frac{V_{l(j-1)}I_{lj} - V_{lj}I_{l(j-1)}}{I_{lj} - I_{l(j-1)}} \tag{2.49}$$

Here j = 1…4; and the magnitude of j – 1 = 0 at j = 1 corresponds to the point V_{oc}. Firstly, the obtained value of V_m has to be positive, and secondly, it has to fall within the range between chosen neighboring values of V_{lj} and $V_{l(j-1)}$. Hence, the magnitude of $V_{l(j-1)}$ has to be positive. After checking the conditions $V_{lj} \le V_m \le V_{l(j-1)}$, the current I_m is sought as

$$I_m = \frac{I_{l(j-1)}V_m}{2V_m - V_{l(j-1)}} \tag{2.50}$$

If this condition is not met, the calculation using (2.49) is repeated for other pairs of neighboring bend points. Finally, if the middles of the hypotenuses in the triangles corresponding to two neighboring

segments do not lie on the I-V characteristic, but are situated on opposite sides from the bend point separating them (as is depicted in Figure 2.17), this bend point itself is taken as the maximum power point. The shaded rectangle in Figure 2.17 corresponds to the maximum electric power.

At the first stage of P/P_0 calculations in [26], the fixed photocurrent density i_{ph} = 1 A · cm^{-2} was used at V_{oc} = 1.14 V, and the magnitudes of R_s^* and R_d^* were varied over a wide range. For the given case discrete coordinates of four I-V characteristic points were calculated by the formulae (2.44), and then the

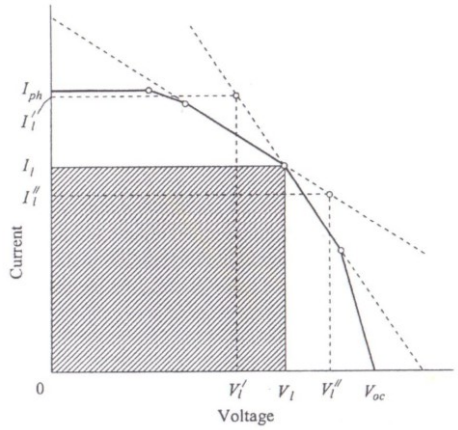

Figure 2.17 The procedure of calculation of the maximum power point of an approximated I-V characteristic

maximum power point coordinates and output electric power were calculated by the formulae (2.49) and (2.50). The calculated dependences of P/P_0 are presented by solid curves in Figure 2.18. Authenticity of these curves for a wide range of the photocurrent densities $0.01 \leq i_{ph} \leq 100\ A \cdot cm^{-2}$ was checked by additional selected calculations confirming universality of the obtained dependences.

Also the experimental verification of the dependences of Figure 2.18 was carried out in the work [26]. Flash illumination of the GaAs-based solar cells was used for I-V curve measurements. Solar cell specimens of quite varied geometries were chosen for this experiment (see the inset in Figure 2.18 and Table 2.1).

In the case of specimen "a" the parameter under variation was the resistance R_s^* at a fixed illumination level.

This was possible because at a chosen value of the photocurrent one may neglect the intrinsic resistance components of the specimen itself and introduce R_s with the help of a resistance box. In the case of the other specimens the illumination level (the photocurrent I_{ph}) was varied. Table 2.1 shows values of R_s^* and R_d^* for each of the specimens except the first one which were evaluated from the experimental I-V characteristics by the procedure given in section 2.5 (construction of $R_{0.5}$ and $R_{0.95}$ lines in accordance with figure 2.15 and then calculation of R_s^* and R_d^* by the formulae (2.46)).

Specimen “b” was an example of a solar cell of a classical design (see Figure 2.1a) where 6 units are parallel-connected. Specimen “c” intended for conversion of non-concentrated sunlight was characterized by the I-V characteristic ideality factor of $A \approx 1.2 - 1.3$ in the range of photocurrents I_{ph} = 0.05-0.1 A while all P_0 values were calculated for A = 1. This explains the discrepancy between the theoretical and the experimental data corresponding to this specimen in the region $P/P_0 \approx 1$.

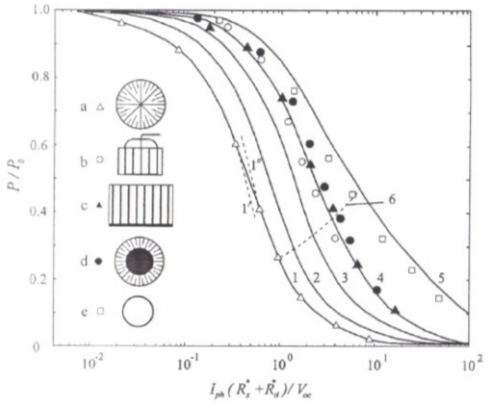

Figure 2.18 Dependences of the relative efficiency of the photoelectric conversion in a gallium arsenide solar cell on the generalized argument $\left(\boldsymbol{I_{ph}}(\boldsymbol{R_s^*} + \boldsymbol{R_d^*})\right)/(\boldsymbol{V_{oc}})$; $\boldsymbol{R_d^*} = \mathbf{0}$ (curve 1); $\boldsymbol{R_d^*}/\boldsymbol{R_s^*} = \mathbf{0.5}, \mathbf{2.5}$ and $\mathbf{7.5}$ (curves 2-4, respectively); $\boldsymbol{R_s^*} = \mathbf{0}$ (curve 5). Curve 6 is the lower boundary of $I_{sc} = I_{ph}$; and curves 1’ and 1’’ are calculated from the formulae (2.47) and (2.48). The symbols represent the experimental data (see the insert and Table 2.1)

Table 2.1 Parameters of the AlGaAs/GaAs-based solar cells under investigation

Sample geometry in Figure 2.19	Dimensions of photosensitive area	Effective values of resistances, Ω		
		R_s^*	R_d^*	I_{ph}, A
a	17 mm in diameter	0-10	0	1
b	7 × 5 mm^2	0.045	0.10	1-20
c	22 × 20 mm^2	0.14	1.25	0.05-17
d	ext. diameter 17 mm,	0.01	0.14	1-120
e	4 mm in diameter	0.16	3.90	0.05-15

Measurements on the specimen “d” were carried out under non-uniform illumination (the central part was shadowed), and the corresponding resistance values in Table 2.1 are related to such an operating regime.

An almost pure distributed character of ohmic losses in specimen “e” was achieved owing to the absence of the metallic contact grid on the solar cell photo-sensitive surface. Moreover, the ring-form current collector had a low contact resistance.

Good agreement of the theoretical and experimental data in Figure 2.18 corroborates the feasibility of

the practical use of the obtained dependences for the output power estimation for solar cells of various geometries over a wide range of illumination levels. In the case of the pure lumped ohmic losses ($R_d^* = 0$, curve 1), nearly the whole upper half of the $P/P_0 = f\left(I_{ph}R_s/V_{oc}\right)$ curve is adequately described by the approximating formula (2.47) (curve 1'), and the lower half by the formula (2.48) (curve 1'').

The dashed curve 6 of Figure 2.18 divides the set of curves into two parts. In the upper part the equality of the short circuit current I_{sc} to the photocurrent I_{ph} is met. In this case the ratio P/P_0 is equal to the ratio FF/FF_0, where FF is the fill factor of the solar cell I-V characteristic at a given illumination level; and FF_0 is the factor in the absence of internal ohmic losses. As to the saturation regime ($I_{sc} < I_{ph}$, the lower part), so the essentially higher values of FF take place in the case of pure distributed losses (curve 5) rather than in the case of lumped losses. This results from the higher convexity of the I-V characteristic of a solar cell with distributed ohmic losses.

It should be noted in conclusion that consideration of the multisection equivalent circuits of solar cells with distributed parameters allows us to obtain simple algebraic expressions for discrete coordinates of illuminated I-V characteristic. These expressions hold true for low, middle and high illumination levels. For the simplest solar cell geometry (a rectangular specimen with a linear busbar contact), a "classical" problem is solved concerning the comprehensive analysis of the I-V characteristic shape when both distributed and lumped components of the internal resistance take place. For the engineering calculations of the I-V characteristics of solar cells with an arbitrary geometry it is necessary to use two resistance magnitudes, the effective distributed resistance (R_d^*) and the effective lumped (series) resistance (R_s^*). These parameters do not depend on the illumination level and ensure construction of the illuminated I-V characteristic with a fair accuracy. For this reason they objectively characterize the internal ohmic losses in a solar cell. The obtained universal P/P_0 graphs may be used in solving various optimization problems concerned with design of the photovoltaic modules operating with sunlight concentrators.

3 PHYSICAL EFFECTS ARISING IN A SILICON SOLAR CELL OPERATING UNDER CONCENTRATED SUNLIGHT

The main topic of this thesis is the development of a distributed electrical solar cell model and its application to the analysis of solar cell behaviour in a variety of working conditions that are typically imposed by Concentrating Photovoltaic (CPV) Systems.

CPV systems allow to reach very high concentration ratios, leading to a series of physical effects to occur in the cells. Analysis of such effects is of great importance in understanding the behaviour of silicon solar cells operating under concentration and also can serve as a basis for improving cell design and performances.

3.1 HIGH DOPING EFFECTS

As has been pointed out in [31], at high doping concentrations, as in solar cell emitter region, several effects must be considered in order to describe the energy-band structure:

a) Many-body effects to account for the interaction between carriers and between carrier and ionized impurities. This effect results in virtually rigid shift of both the conduction and valence bands in the E-k space. E_c and E_v are shifted towards each other.
b) The effects of the electrostatic potential fluctuations to account for the random distribution of impurities together with the overlap of the electron wave functions at the impurity states causing *band tails* and *impurity bands*. This effect alters the shape of the density of states function.

3.1.1 MANY-BODY EFFECTS

There are three many-body effects to take into account for n-type highly doped silicon: electron-donor interactions, electron-electron interactions and electron-hole interactions. They were reviewed by Fossum and Lee [32].

- *Electron-donor interactions.* At sufficiently high dopant concentrations, the electrons are so numerous that Coulomb screening of the donor ions by the electrons effectively reduces the impurity ionization energy $E_C - E_D$. At doping levels higher than 3×10^{18} cm^{-3} for Si the ionization energy becomes zero.

  The electron-donor interaction results in a shifting up of the donor levels. For a zero ionization energy, the bound states are non-existent and the local lattice potential at the donor site equals

that at the other lattice sites, as if the donor impurity were not present. The bands remain virtually intact, while the donor levels move up and ultimately disappear into the conduction band.

- *Electron-electron interaction.* A solution of the one-electron approximation, taking the periodic potential due to the free electrons into account, indicates that the conduction band edge shifts downwards. This rigid gap narrowing is referred to as ΔE_c^{mb}.
- *Electron-hole interaction.* The majority carriers also screen the mobile minority carriers. This screening reduces the hole potential energy and effectively shifts the valence band up towards the conduction band. This rigid bandgap narrowing is referred to as ΔE_V^{mb}. Mahan [33] estimated the upward shift.

The total effect of the many-body effects on the gap narrowing equals $\Delta E_c^{mb} + \Delta E_V^{mb}$. The resulting gap change can also be detected with optical measurements.

3.1.2 RANDOM IMPURITY DISTRIBUTION

The impurity distribution in an extrinsic semiconductor is not uniform. For highly doped materials, the resulting fluctuation of the electrostatic potential energy causes a spatial dependence of the local quantum density of states. The statistical average over the entire lattice of the local density of states yields the total density of states function which results in a tailing of both the conduction and the valence band [34, 35]. This band tailing effect is shown in Figure 3.1.

Locally the energy gap is determined by the energy-dispersion relation and is equal to the optical gap. Due to the potential fluctuations however the average conduction-band density of states shows a tail below the parabolic conduction band. This macroscopic energy gap, as determined by electrical measurements, is therefore smaller than the optical one. The effects of disorder are modeled by an effective shift of the conduction band $\Delta E_G^{disorder}$, while still maintaining a parabolic density of states function.

The random impurity distribution also causes the existence of impurity bands. It is believed however that the global effect of the formation of an impurity band on the energy gap narrowing is not important due to the screening effect discussed earlier. The impurity band shifts upward and merges with the conduction band before becoming broad enough to influence the gap narrowing. The macroscopic energy gap narrowing, as determined by electrical measurement, is the result of the optical-gap narrowing and of the equivalent narrowing caused by the lattice disorder.

$$\Delta E_G^{el} = \Delta E_G^{el} + \Delta E_G^{disorder} \qquad \Delta E_G^{mb} = \Delta E_C^{mb} + \Delta E_V^{mb} = \Delta E_G^{opt}$$

The values for ΔE_G^{el} and ΔE_G^{opt}, calculated theoretically by Fossum and Lee [32] are shown in Figure 3.2.

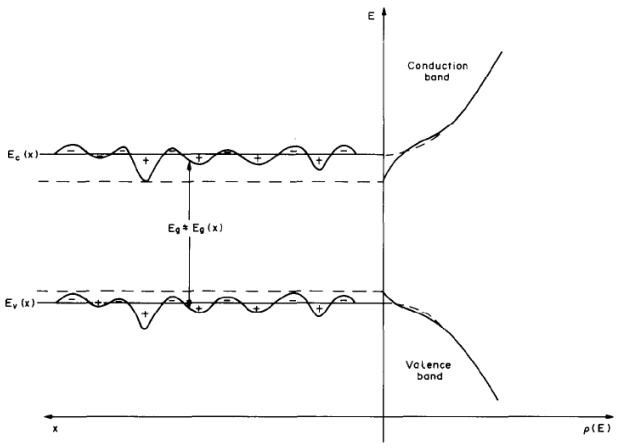

Figure 3.1 Formation of band tails resulting from random spatial variations of the electrostatic potential caused by the random impurity distribution

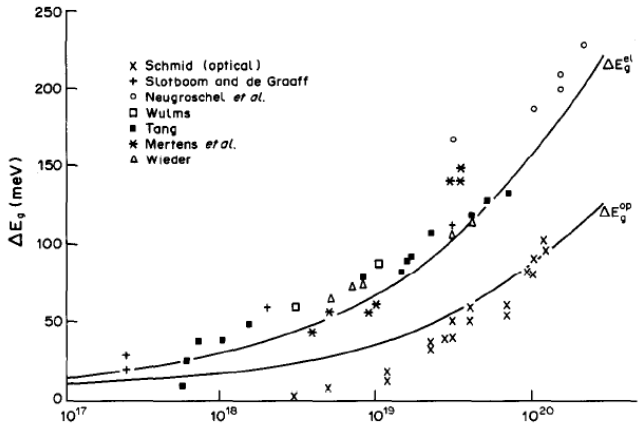

Figure 3.2 Electrical and optical energy gap narrowing versus donor doping density. The curves are based on theoretical calculations; the points are experimental data.

3.2 EFFECT OF HEAVY DOPING ON MINORITY CARRIER CONCENTRATION

As is shown in [36], in thermal equilibrium the concentrations of charge carriers in a semiconductor are given by

$$N_0 = N_C F_{1/2}(\eta_C) \tag{3.1}$$

$$P_0 = N_V F_{1/2}(\eta_V) \tag{3.2}$$

where N_C and N_V are the effective density of states in the conduction and valence bands, respectively, $F_{1/2}$ is the Fermi-Dirac integral of order 1/2, and

$$\eta_C = (E_F - E_C)/kT \tag{3.3}$$

$$\eta_V = (E_V - E_F)/kT \tag{3.4}$$

As suggested by Landsberg et al. [37], the analytic approximation

$$F_{1/2}(\eta) = \frac{e^{\eta}}{1 + C(\eta)e^{\eta}} \tag{3.5}$$

can be used in the range -4 ≤ η ≤ 10. Here $C(\eta)$ is a function of η given in [37]. Using (3.5) in (3.1) and (3.2), we can write

$$N_0 = \frac{N_C e^{\eta_c}}{1 + C(\eta_c)e^{\eta_c}} \tag{3.6}$$

$$P_0 = \frac{N_V e^{\eta_V}}{1 + C(\eta_V)e^{\eta_V}} \tag{3.7}$$

Thus from (3.6) and (3.7)

$$n_{ie}^2(x) = N_0 P_0 = \frac{N_C N_V e^{-E_G(x)/kT}}{1 + C(\eta_C)e^{\eta_C} + C(\eta_V)e^{\eta_V} + C(\eta_C)C(\eta_V)e^{-E_G(x)/kT}} \tag{3.8}$$

where

$$E_G(x) = E_{G0} - \Delta E_G(x) \tag{3.9}$$

In which E_{G0} is the bandgap of the intrinsic semiconductor, and $\Delta E_G(x)$ is the band gap narrowing due to heavy doping. For an n-type heavily doped region, as the emitter region of a solar cell, $\eta_V \ll 0$ and $C(\eta_V) = 0$ in (3.8). Furthermore, the term $C(\eta_C)C(\eta_V)e^{-E_G(x)/kT} \ll 1$. Therefore, for a heavily doped n-type region, (3.8) reduces to

$$n_{ie}^2(x) = N_0 P_0 = \frac{n_i^2 e^{\Delta E_G(x)/kT}}{1 + C(\eta_C)e^{\eta_C}} \tag{3.10}$$

Similarly, for a p-type heavily doped region

$$n_{ie}^2(x) = N_0 P_0 = \frac{n_i^2 e^{\Delta E_G(x)/kT}}{1 + C(\eta_V) e^{\eta_V}} \tag{3.11}$$

In (3.10) and (3.11), n_i is the intrinsic concentration in the pure semiconductor.

For an n-type heavily doped region equation (3.10) allows to take into account the bandgap narrowing and the Fermi-Dirac statistics. These two mechanisms affect the minority carrier concentration in opposite ways. Bandgap narrowing tends to increase the minority carrier concentration, while inclusion of Fermi-Dirac statistics tends to decrease the minority carrier concentration below the value calculated using Maxwell-Boltzmann statistics.

In (3.10), for $\eta \leq 4$ (e.g. $N_0 \leq 2\times10^{20}$ cm^{-3} in n-type silicon), $C(\eta)$ is [37]

$$C(\eta) \cong -0.04\eta + 0.3 \tag{3.12}$$

The above expression of $C(\eta)$ gives values of the Fermi-Dirac integral of order ½ with less than 4-percent error.

In non-equilibrium conditions, bandgap narrowing increases the minority carrier current by

1) increasing the minority carrier concentration,
2) decreasing the retarding built-in electric field acting on the minority carriers.

The increase in the minority carrier concentration P results from the increase in $n_{ie}^2(x)$. The decrease of the built-in electric field is due to the position dependence of $n_{ie}^2(x)$ (and hence of the effective bandgap) in the inhomogeneously doped emitter.

To develop a simple expression illustrating the reduction of the electric field, we now include only bandgap narrowing excluding the effect of Fermi-Dirac statistics for the present.

The effective electric field acting on minority carriers can be obtained from the expression for minority carrier current density in the n-type region:

$$J_P(x) = q\mu_p P(x) E(x) - qD_P \frac{dP(x)}{dx} \tag{3.13}$$

From (3.13) we obtain, in thermal-equilibrium conditions

$$E(x) = \frac{D_P}{\mu_P} \frac{1}{P(x)} \frac{dP(x)}{dx} \tag{3.14}$$

Substituting in (3.13) the (3.14) and the fact that $n_{ie}^2(x) = N_0(x)P_0(x)$, after some manipulations, we obtain [36]

$$J_P(x) \frac{N_0(x)}{n_{ie}^2(x)} dx = -qD_P d\left[\Delta P(x) \cdot \frac{N_0(x)}{n_{ie}^2(x)}\right] \tag{3.15}$$

The effective electric field acting on minority carriers, given in (3.14), can be expressed by using (3.15) and the fact that $n_{ie}^2(x) = N_0(x)P_0(x)$, as

$$E(x) = A(N_0)\left[-\frac{D_N}{\mu_N}\cdot\frac{1}{N_0(x)}\cdot\frac{dN_0(x)}{dx}\right] \tag{3.16}$$

where

$$A(N_0) \equiv \left[1 - \frac{N_0(x)}{kT}\cdot\frac{d\Delta E_G(x)}{dN_0(x)}\right] \tag{3.17}$$

The factor $A(N_0)$ measures the reduction of the built-in electric field due to bandgap narrowing, and is always less than 1. In the absence of bandgap narrowing, the holes experience a retarding electric field in an n-type diffused emitter. Figure 3.3 shows $A(N_0)$ as a function of the electron (majority carrier) concentration for three models of bandgap narrowing: Slotboom and DeGraaf [35], Hauser [38], and the more recent model of Lanyon and Tuft [39], which has the form

$$\Delta E_G = 22.5\times10^{-3}(N/10^{18})^{1/2}\ \ eV$$

for nondegenerately doped silicon, and

$$\Delta E_G = 16.2\times10^{-3}(N/10^{20})^{1/6}\ \ eV \tag{3.18}$$

for degenerately doped silicon.

Equations (3.16) and (3.17) indicate that the position dependence of the bandgap narrowing, in effect, decreases the retarding electric field.

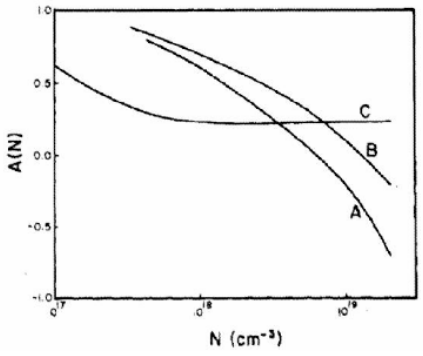

Figure 3.3 The bandgap narrowing reduction factor $\boldsymbol{A(N)}$ versus the electron (majority carrier) concentration N for: A- Lanyon Tuft model, B- Hauser model, and C- Slotboom-DeGraaf model.

3.3 RECOMBINATION IN HEAVILY DOPED SILICON

Minority carrier recombination in lightly doped silicon is quite well understood and can be explained by Shockley-Read-Hall phonon recombination through deep trap levels. Progress in crystal preparation and device processing has resulted in the achievement of very high minority carrier lifetimes. On the other hand, for heavy doping the situation is less clear since many recombination mechanisms may compete with each other. Although the experimental values show evidence for a minority carrier lifetime decrease with doping level, there exists no unanimous agreement in the literature concerning the minority carrier lifetime vs doping relation and the relative importance of the different mechanisms.

Several effects causing a decreasing minority carrier lifetime with increasing doping level exist [31].

- *More traps become effective.* Shockley-Read-Hall phonon recombination through a trap level is given by:

$$R = \frac{np - n_i^2}{(n + n_1)\tau_{p0} + (p + p_1)\tau_{n0}} \tag{3.19}$$

where

$$n_1 = n_i e^{(E_t - E_i)/kT} \qquad p_1 = n_i e^{(E_i - E_t)/kT}$$

In heavily doped n^+ material $n = N_D > p$ and equation (3.19) can be written as:

$$R = \frac{N_D \Delta p}{N_D \tau_{p0} + n_1 \tau_{p0} + p_1 \tau_{n0}} = \frac{\Delta p}{\tau_{p0} + (n_1/N_D)\tau_{p0} + (p_1/N_D)\tau_{n0}} \tag{3.20}$$

$$= \frac{\Delta p}{\tau_{eff}} \tag{3.21}$$

Equations (3.20) and (3.21) clearly indicate that if n_i or p_i exceed N_D, τ_{eff} will be large and the recombination level will be ineffective. This will be the case at low doping for levels situated close to the band edges. As illustrated in Figure 3.4 only levels situated in the range $2(E_F - E_i)$ behave as effective recombination centers. Since E_F moves towards the conduction band edge if N_D increases, more levels become effective at higher doping levels.

In n^+ material, the fundamental defect density increases with doping. The most probable fundamental defects in silicon appear to be of acceptor type. These defects are created during processing or crystal fabrication and will be frozen in during cooling. The solubility of such

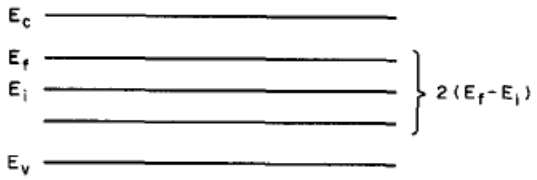

Figure 3.4 Effective recombination levels

defects can be derived as a function of the donor concentration N_D using an analysis proposed by Fuller [40] and reviewed by Fossum and Lee [41]. This analysis has found that the solubility of the ionized acceptor type defect increases strongly with the donor concentration.

- *The trap-assisted Auger process.* For low-doping concentrations, recombination via traps occurs through a process in which the recombination energy is released as phonons. It is basically a two-carrier process and the capture cross-section does not depend on the doping concentration. At higher dopant densities recombination through the same traps may occur via a process in which the recombination energy is released as kinetic energy given to a third carrier. This trap-assisted Auger process, as it occurs in n^+ silicon, is illustrated in Figure 3.5. An electron in the conduction band (1) collides with an electron in a trap (2) which recombines with a hole (3) in the valence band. The recombination energy is given to the first electron as kinetic energy. The recombination rate for this process can be written as:

$$R_{TAA} = C_{TAA} n n_T p \tag{3.22}$$

in which n_T denotes the concentration of traps, filled with electrons. In n^+ silicon $n_T = N_T$ with N_T

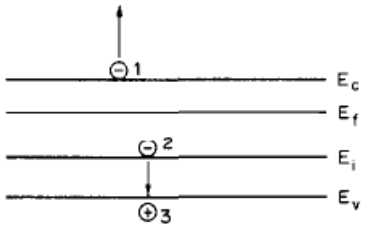

Figure 3.5 Trap-assisted Auger process in n^+ Si.

the total number of traps with energy level E_T.

Assuming complete ionization $n = N_D$ and equation (3.22) yields:

$$R_{TAA} = C_{TAA} N_D N_T P \tag{3.23}$$

C_{TAA} is the trap-assisted Auger coefficient. The lifetime corresponding to the process described by equation (3.23) is given by:

$$\tau_{TAA} = \frac{1}{C_{TAA} N_T N_D} \tag{3.24}$$

This expression clearly shows that the trap-assisted Auger lifetime decreases linearly with the donor concentration if the trap density is independent of the doping level. If N_T increases with the doping level the TAA process can yield stronger than linear dependencies. It can be proven that the C_{TAA} coefficient strongly increases if the energy that has to be bridged by the recombining electron-hole pair decreases. This implies that for n^+ silicon only levels relatively close to the valence-band edge will be effective recombination centers for the TAA process.

- *The band-to-band Auger process.* It is well known that the band-to-band (BBA) Auger process is important in heavily doped silicon. The process occurs as illustrated in Figure 3.6.

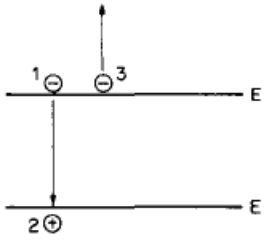

Figure 3.6 Band-to-band Auger process.

An electron (1) collides with another electron (3) in the conduction band. This collision results in a recombination of the first electron with a hole (2) in the valence band and the recombination energy is given to electron (3) as kinetic energy.
The recombination rate in n^+ silicon is given by:

$$R_{BBA} = C_{BBA} n^2 p \tag{3.25}$$

$$= C_{BBA} N_D^2 P \tag{3.26}$$

The corresponding lifetime is:

$$\tau_{BBA} = \frac{1}{N_D^2 C_{BBA}} \tag{3.27}$$

It is believed by many researchers that especially phonon-assisted band-to-band Auger effects can dominate the recombination in heavily-doped silicon.

3.4 SOLAR CELL PERFORMANCES IN THE PRESENCE OF HEAVY DOPING EFFECTS AND HIGH-LEVEL INJECTION

In [42] the basic set of transport equations for a conventional silicon solar cell have been solved by the modified form of the Gummel [43] and De Mari [44] algorithm. Effects due to high doping have been incorporated by defining the intrinsic charge carrier concentration, n_i, as a function of the band gap narrowing [45, 46], which is further modified by Fermi-Dirac statistics correction factor for density of states. The bandgap narrowing model [45, 46] taken in [42] gives sufficiently accurate interpretation of the characteristics. A combined form of Shockley-Read-Hall (SRH) recombination (i.e. recombination via trapping levels at the middle of the bandgap) and Auger recombination (i.e. direct band to band recombination) [47] has been used as the recombination rate:

$$R = \frac{pn - n_i^2}{\tau_{p0}(n + n_i) + \tau_{n0}(p + n_i)} + \gamma n\left(pn - n_i^2\right) \tag{3.28}$$

where γ is the Auger coefficient and τ_{p0} and τ_{n0} are the holes and electrons lifetimes, respectively.

The analysis have been performed in the sunlight concentration interval 1-200 AM 1.

The current-voltage characteristic of a solar cell can be expressed in the following way, neglecting any internal resistance component:

$$J = J_L - \sum_{j=1}^{3} J_{jo}\left(exp\left(\frac{qV}{a_j kT}\right) - 1\right) \tag{3.29}$$

where J_0 is the saturation current density and "a" is the ideality factor.

The above expression includes all the effects that occur in a diode; j = 1 indicates the diffusion process, j = 2 indicates the recombination process in the space charge layer of the diode and j = 3 indicates the high-injection effect which occurs at high level illumination. If the diode is controlled mainly by one of the processes, the above expression leads to

$$J = J_L - J_o\left(exp\left(\frac{qV}{akT}\right) - 1\right) \tag{3.30}$$

The values of J_0 and "a" determine the mechanism that controls the diode. Even though in [42] temperature is assumed to be a constant even at high illumination levels, its effect will be taken into account in our model, as we will see later. The cell's performance are evaluated in [42] by fitting values of open-circuit voltage, V_{OC}, short-circuit current density, J_{SC}, saturation current density, J_0, fill factor, FF and ideality factor, "a".

The basic structure assumed in [42] is a conventional n^+- p Si solar cell. The chosen surface doping concentration, N_s, is $3 \times 10^{20} cm^{-3}$ (phosphorous doped) and the bulk acceptor doping level is $10^{16} cm^{-3}$ (corresponding to a 1.5 Ω·cm resistivity, as can be deduced from Irvin curves) with a junction depth, x_j, of 0.3 μm (an error function diffused profile has been assumed); an emitter

resistivity of $30\,\Omega/\square$ has been considered in this case. The chosen thickness of the device is 250 μm with the front surface minority carriers (holes) recombination velocity, S_{p0}, of $5 \times 10^4\ cm/sec$.
The dependence of the minority carrier lifetime with doping concentration is similar to the one used by Fossum [48] in the solar cell analysis. The expression for the minority carrier hole lifetime in the diffused layer is

$$\tau_p = \frac{\tau_{p0}}{1 + \frac{N}{7.1 \times 10^{15}}} \tag{3.31}$$

A similar expression is used to determine the electron lifetime in the base. The lifetime constants τ_{p0} and τ_{n0} are chosen to be 39.4 and 394 μs for holes and electrons respectively. Since the absorption cross section for holes is usually larger than electrons, one tenth of the electron lifetime has been used throughout the structure. The photon spectrum AM 1 has been used to calculate the generation rate.
Here are reported some calculation results obtained in [42] and that will be used as input parameters in our model, as will be discussed later. The variation of J_{SC} with light concentration, X, is shown in Figure 3.7. The plot of lnJ_{SC} vs lnX is a straight line with a slope of 1.01. This deviation of J_{SC} from linearity can be explained following Fossum et al. [49]. This is because the photocurrent flows under short-circuit conditions. An electric field developed because of such photo-induced carriers in the base opposes the diffusion of the charges towards the back contact and prevents the recombination at the back contact to a certain extent. This action is somewhat similar to a back surface field (BSF).

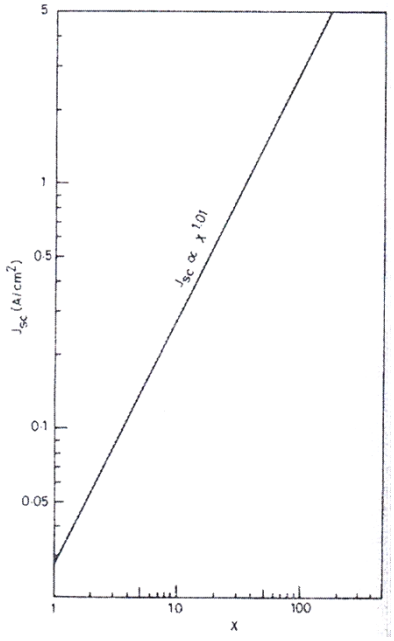

Figura 3.7 Short-circuit current density variation with X

The open-circuit voltage varies with J_{SC} and J_0 as,

$$\boldsymbol{V_{OC} = \frac{akT}{q} ln\left(\frac{J_{SC}}{J_0}\right)} \qquad (3.32)$$

Since J_{SC} varies as $X^{1.01}$ the V_{OC} in the above expression should vary as $\boldsymbol{lnX}$ and the plot of V_{OC} vs $\boldsymbol{lnX}$ should be a straight line. Experimental measurements and calculation results obtained in [40], however, show that the variation of V_{OC} with $\boldsymbol{lnX}$ is not linear at high illuminations. Here V_{OC} is the difference between the junction potential, V_J, and the potential drop across the base region, V_B, i.e.

$$\boldsymbol{V_{OC} = V_J - V_B} \qquad (3.33)$$

For an illumination level of one sun, low-level injection in the quasi-neutral base region is assumed. At high level illuminations, high-level injections occur throughout the base region. There exists an illumination level for which hole and electron charge densities become equal. This occurs, for the cell at about X = 100 suns. Since the tendency of electrons to diffuse is greater than for holes this results in an electric field directed away from the junction (this is true even for n-substrate). This develops the potential across the base, which is opposite in polarity to the junction potential and deviates from the behaviour given by (3.3). This is shown in Figure 3.8.

$\boldsymbol{lnJ_0}$ vs $\boldsymbol{lnX}$ and "a" vs $\boldsymbol{lnX}$ curves are shown in Figures 3.9 and 3.10, respectively. $\boldsymbol{lnJ_0}$ vs $\boldsymbol{lnX}$ curve has two distinct slopes suggesting two different mechanisms, that are controlling the diode in two different ranges of illumination. As the illumination is increased both the diffusion rate and the recombination rate increase with X.

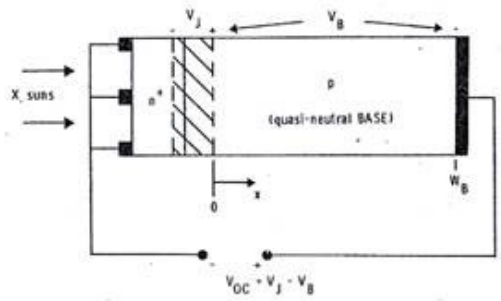

Figure 3.8 A voltage drop across the base arises at high levels of illumination

This is depicted in the initial portion of the $\boldsymbol{lnJ_0}$ and "a" plots. Above about 50 suns the high-injection starts to dominate the diffusion recombination processes. The ideality factor increases from 1.004 at X = 1 sun to 1.64 at X = 200 suns. This shows that the diode is mainly controlled by the high-injection process at high levels of illumination. Table 3.1 reports calculated values of J_{SC}, "a" and J_0 at different concentration levels, obtained in [000]. These values will be used as input parameters in the

distributed electrical model developed in this thesis. It important to note that theoretical development of the pertinent physics describing the solar cell behaviour under concentrated sunlight pertains to what we may call the "intrinsic" one dimensional portion of the cell illustrated in Figure 3.11.

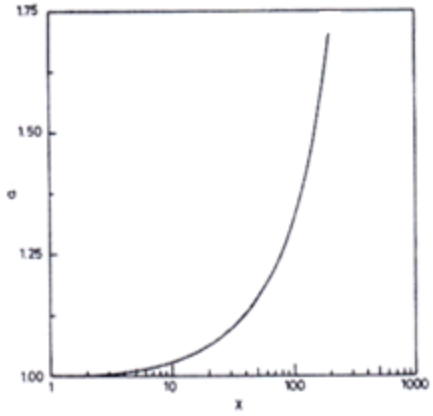

Figure 3.9 Ideality factor variation with X

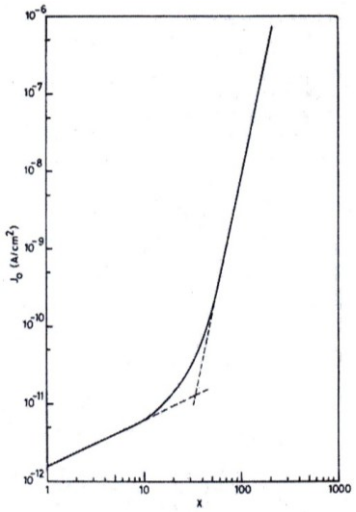

Figure 3.10 Saturation current density variation with X

Specification of the intrinsic device defines the cell structure, i.e. n^+ - p, p^+ - n - n^+ etc., and the morphology, i.e. doping profiles, junction depths, etc. If we want to assess the behaviour of an entire solar cell, we also have to define the "extrinsic" device by specifying the cell geometry and the top-electrode pattern. This is the approach followed in the work described in this thesis.

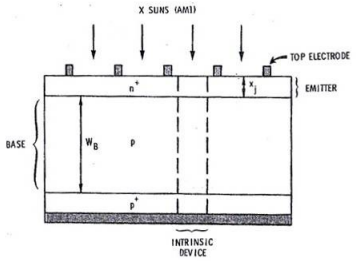

Figure 3.11 A n^+ - p – p^+ solar cell with its intrinsic portion identified

Table 3.1 Parameters of an n^+ - p silicon solar cell at various concentration ratios, as has been calculated in [42]

X (AM 1)	J_{SC} (A/cm^2)	a	J_0 (A/cm^2)
1	0.027	1.004	$1.584 \cdot 10^{-12}$
5	0.139	1.006	$4.087 \cdot 10^{-12}$
10	0.279	1.024	$6.783 \cdot 10^{-12}$
20	0.562	1.055	$1.244 \cdot 10^{-11}$
50	1.428	1.163	$1.585 \cdot 10^{-10}$
100	2.894	1.309	$7.943 \cdot 10^{-9}$
200	5.780	1.690	$6.192 \cdot 10^{-7}$

3.5 TEMPERATURE EFFECT

Increasing concentration factor X also increases cell working temperature, leading to a decrease of V_{OC} and FF. The most significant performance degradation is related to the decrease in V_{OC} which is due primarily to the temperature dependence of the intrinsic carrier concentration, $n_i(T)$. This dependence, together with the variation of the diode saturation current with n_i,

$$J_0 \propto n_i^2 \tag{3.34}$$

results in

$$\frac{dV_{OC}}{dT} \cong -2mV/°C \tag{3.35}$$

for an ideal p-n junction solar cell.

Furthermore, temperature coefficient of resistance (TCR) for silicon as a function of temperature and doping concentration, for both p- and n-type material, has been taken into account in order to adjust resistor values in our distributed electrical solar cell model, depending on cell working temperature.

It is defined as:

$$TCR(T) = \frac{1}{R}\frac{dR}{dT} \tag{3.36}$$

Theoretical calculations performed in [50], together with experimental values are shown in Figures 3.12 and 3.13; they have been used as additional input parameters in our model.

These results are valid for a doping concentration not higher than 10^{18} cm^{-3}. For greater doping concentration levels approximated values have been considered.

Finally, variation of resistance with temperature for solar cell metallization has also been considered. In this case a constant value of TCR (not dependent on temperature) has been assumed.

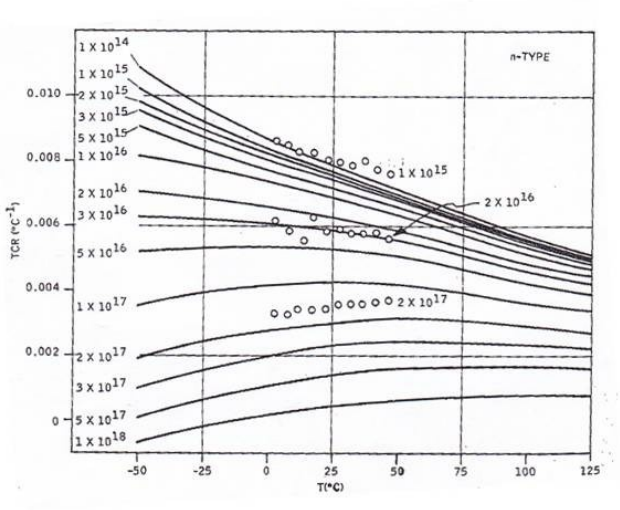

Figure 3.12 Calculated TCR obtained in [50], for n-type silicon as a function of temperature, shown for a range of donor concentrations

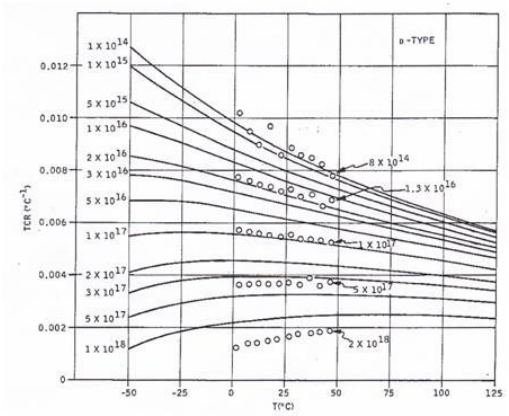

Figure 3.13 Calculated TCR obtained in [50], for p-type silicon as a function of temperature, shown for a range of acceptor concentrations

4 A 2.5D DISTRIBUTED SOLAR CELL MODEL

A number of works exists in literature about the representation of solar cell electrical behavior through a distributed electrical network and its subsequent solution by means of a suitable software. The major part of these models consist in dividing the solar cell surface in a grid of subcells, each of which is represented by its equivalent electrical circuit. In [51] and [52] each of the distributed model elements contains a single- or two-diode equivalent circuit with a shunt resistor in parallel, a base resistor connecting the PV element to the backside contact or ground representing the bulk resistivity, emitter resistors connecting to other elements representing series resistance in the emitter and contact resistors between emitter and contact fingers, if applicable, representing contact resistance. In [53] a distributed model based on single-diode equivalent circuit is implemented. This approach has also been followed in this work; solar cell surface has been divided into a grid of subcells each of which being represented by its equivalent electrical circuit. In particular bulk, emitter, metal-semiconductor contact and front contact grid resistances have been taken into account. Furthermore, back contact resistance has been modeled only in some cases, as we will see later, while it has been represented as an equipotential surface in all other cases.

Figure 3.1 shows a schematic representation of how solar cell surface is divided into a grid of elements and also presents the types of electrical circuits used to model each element, in their general structure. Firstly, as is shown in Figure 3.1, this is not a true 3-dimensional model, since the elements represent the dimension along the axis normal to the solar cell surface, so one dimension is not free. Secondly, two types of electrical circuit are used to represent cell surface, depending on whether the element is covered by front grid metallization or not. In the case of a bare semiconductor element, the equivalent circuit is that shown on the left side of Figure 3.1; it contains a single-diode model which takes into account p-n junction behavior, connected in parallel to a shunt resistor R_{S6} and a current generator I_{SC} (set to a value equal to the photogenerated current produced by that element), a bulk resistor R_{S5} and four emitter resistances R_{S1}, R_{S2}, R_{S3} and R_{S4} providing connections to the four neighboring elements of the grid. In the case of a subcell covered by front contact grid metallization current generator I_0 value is set to zero since that portion of the cell is shadowed by front metallization and therefore it does not produce any photogenerated current; bulk resistor and emitter resistances are substituted by metal-semiconductor contact resistance R_{M5} and emitter resistances R_{M1}, R_{M2}, R_{M3} and R_{M4}, respectively. The choice not to model emitter layer under front metallization is physically justified due to very low resistivity of metal with respect to semiconductor. Furthermore, this approximation allows us to reduce the total number of network elements and hence the computational time. In Figure 4.1 is evident the absence of the back contact layer: it is simply represented as an equipotential surface.

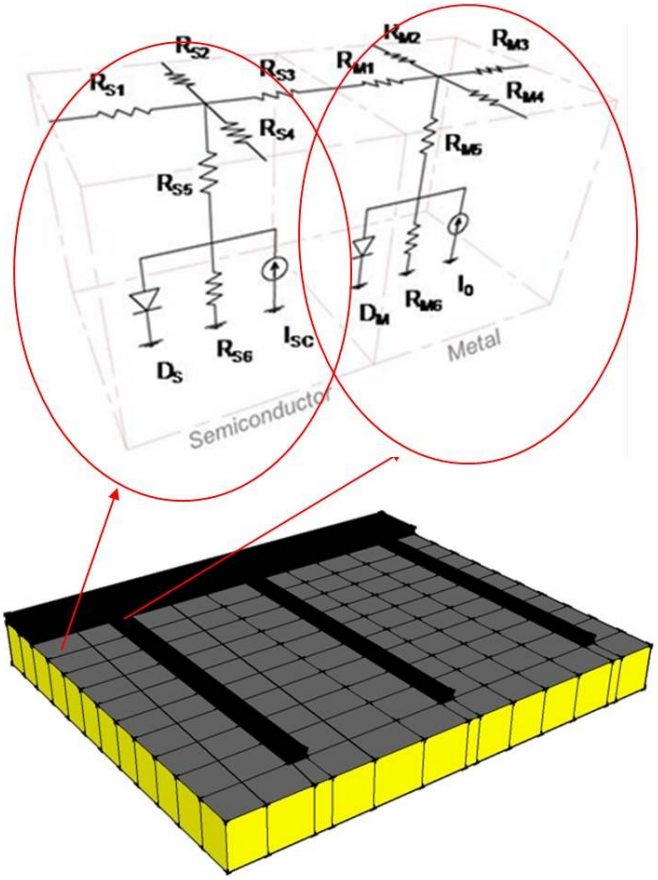

Figure 4.1 A pictorial representation of cell surface division in a grid of elements and types of electrical circuits used to represent them

Even though this is an acceptable approximation in most case studies, in some special conditions it must be modeled analogously to the emitter. This additional model refinement will be implemented when we will study the void formation in solar cell solder joints.

4.1 MODEL IMPLEMENTATION

The first step of the model implementation is the creation of the grid of subcells. Such a grid must have a resolution high enough to properly represent the front contact grid pattern. To this end a MATLAB script has been created in order to provide a binning of the cell surface; for most cases discussed in this thesis a non-linear binning has been performed; it allows to map different regions of the cell with different resolutions, leading to a reduction of the total number of elements with respect to a simple linear binning. Front contact grid pattern is constructed as a binary array by a separate MATLAB function; it identifies subcells covered by metallization allowing to use correct parameters for each of them.

Resistor values are calculated taking into account geometrical characteristics of each subcell in a way that will be discussed in Section 4.1.1.

Diode parameters, such as ideality factor and inverse saturation current have been calculated on the basis of the values reported in Table 3.1. In particular, saturation current values in each subcell have been obtained by multiplying saturation current density by the area of the subcells.

Current generator values have to be set to the short-circuit current values generated by each element of the grid. If we have a solar cell sample and we want to simulate its performance under concentration, we can experimentally measure a one-sun I-V curve of the sample: knowing the short-circuit current provided by that cell, we can multiply it by the desired concentration factor and obtain an approximated value of the short-circuit current generated by that cell for a certain concentration factor. This value can then be distributed among the grid elements proportionally to the area of each of them.

In this way experimental one-sun I-V characteristics could be compared to simulated ones; a very good agreement between experimental measurements obtained by means of a solar simulator and simulation results have been found for several silicon solar cell samples of different sizes.

Alternatively, a measure of spectral response of the sample can be carried out. Short-circuit current density provided by the sample at an arbitrary concentration factor can be calculated by multiplying each value of spectral response at a certain wavelenght by the irradiance distribution incident onto the cell at that wavelength and by integrating over the whole range of wavelengths considered. Mathematically we have

$$J_{SC} = \int_{\lambda_{min}}^{\lambda_{max}} SR(\lambda) \cdot E(\lambda) d\lambda \tag{4.1}$$

where $SR(\lambda)$ is the spectral response of the cell and $E(\lambda)$ is the spectral irradiance distribution. Both uniform and non-uniform irradiance distributions can be considered. In the latter case, the above integral is a local one; J_{SC} can be evaluated for each subcell of the grid and short-circuit current is obtained by simple integration over the subcell areas.

This procedure, even if on the one hand it requires the knowledge of spectral irradiance distribution incident onto the cell plane, on the other hand it is a more powerful one since it allows to simulate uneven illumination profiles and different spectral photon distributions, such as AM 1 and AM 1.5 spectra.

Spectral irradiance distribution incident onto the receiver of a Concentrating Photovoltaic System strongly depend on the concentrator and on the tracking accuracy of the system. Concentrator influence on the performance of concentrator solar cells will be analyzed in Chapter 4.

Boundary conditions are placed on the lateral edges of the cell by placing very high-value resistors; they take into account the discontinuity of the crystal lattice. The choice of the current extracting

points is another degree of freedom of this model which may affect the cell perfomance. Current can be extracted from the whole cell perimeter, or from some points.

Finally, the MATLAB script provides connections between elements of the grid and creates the PSPICE netlist of the entire nonlinear circuit which is subsequently elaborated by CADENCE PSPICE software. Simulation results allow us to know voltages in every point and currents in every branch of the circuit. Particularly important simulation outputs are I-V curve, power curve and voltage map on the emitter surface.

4.1.1 RESISTOR VALUES CALCULATION

Figure 4.2 shows a typical subcell characterized by its geometrical dimensions: width W, length L, bulk thickness b_t, emitter thickness e_t, metallization width m_w and metallization thickness m_t. Resistors values in the model are calculated by the following formulae:

$$R_{S5} = \rho_{bulk} \frac{b_t}{W \cdot L} \tag{4.2}$$

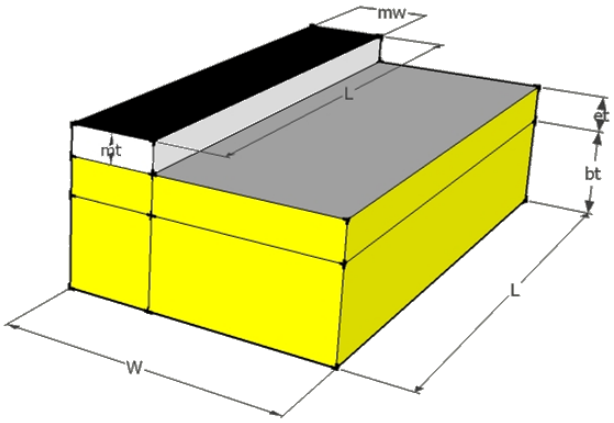

Figure 4.2 Geometrical properties of a typical subcell

$$R_{M5} = \frac{\rho_{contact}}{W \cdot L} \tag{4.3}$$

where ρ_{bulk} and $\rho_{contact}$ are bulk resistivity and metal-semiconductor contact resistivity, respectively. Emitter resistors and front metal resistors values have been calculated following the approach developed in [54]. It takes into account the mean path followed by photogenerated electrons in their travel towards the contact, where the mean is weighted on the whole electron population at every distance from the contact and not on all possible paths for a single electron starting from a fixed point. The shortest path for electrons to reach the contact is assumed; this approximation is justified since metal resistivity is much smaller than semiconductor resistivity. Assuming a uniform photogeneration

probability on the active area of the cell, electron mean path for a square cell element can be calculated, due to figure symmetry, only in a triangle with a vertex in the center of the square and the others on the vertexes of the figure.

If we refer to Figure 4.3, r being the distance from the center of the square, we can express photogeneration probability in the following way:

$$dP(r) = \frac{4}{L^2} 2rdr \tag{4.4}$$

By integrating (3.3) we obtain

$$P(r) = \int_0^{L/2} \frac{4}{L^2} 2rdr \tag{4.5}$$

yielding for mean path

$$\langle \frac{L}{2} - r \rangle = 8 \int_0^{L/2} \frac{1}{L^2} \left(\frac{L}{2} - r \right) rdr = \frac{L}{6} \tag{4.6}$$

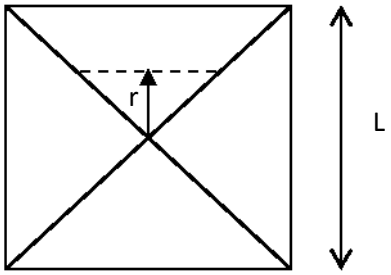

Figure 4.3 A square-shaped element of solar cell, due to its symmetry, can be divided into four triangles

For a rectangular cell element of dimensions L and b, assuming that electrons move towards the longest side of the element L, we have:

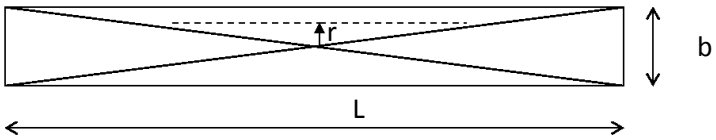

Figure 4.4 A rectangular-shaped element of solar cell, due to its symmetry, can be divided into four triangles

$$P(r)dr = \frac{N}{Lb} 2[(L - b) + 4r]dr \tag{4.7}$$

For the mean path we obtain:

$$\langle \frac{b}{2} - r \rangle = \frac{1}{Lb} \int_0^{b/2} 2\left(\frac{b}{2} - r\right)[(L-b) + 4r]dr = \frac{b}{4} - \frac{b^2}{12L} \tag{4.8}$$

If $L \gg b$:

$$\langle \frac{b}{2} - r \rangle \cong \frac{b}{4} \tag{4.9}$$

Comparison of (4.8) and (4.5) reveals that, for a given value of element area, the square leads to a shorter mean path for electrons and therefore to a higher collection efficiency.

Applying second Ohm's law we can calculate emitter and front metal resistors values in the case of a square cell element:

$$R_{Si} = \int_{L/2-L/6}^{L/2} \rho_{emitter} \frac{dr}{2re_t} = \frac{\rho_{emitter}}{2e_t} \int_{L/3}^{L/2} \frac{dl}{l} = \frac{\rho_{emitter}}{2e_t} ln\left(\frac{3}{2}\right) \tag{4.10}$$

$$R_{Mi} = \int_{L/2-L/6}^{L/2} \rho_{metal} \frac{dr}{2rm_t} = \frac{\rho_{metal}}{2m_t} \int_{L/3}^{L/2} \frac{dl}{l} = \frac{\rho_{metal}}{2m_t} ln\left(\frac{3}{2}\right) \tag{4.11}$$

where $\rho_{emitter}$ and ρ_{metal} are emitter and metal resistivity, respectively, and i = 1…4.

Similarly, for a rectangular cell element we have:

$$R_{Si} = \int_{b/2-b/4+b^2/12L}^{b/2} \rho_{emitter} \frac{dr}{re_t} \frac{b}{L} = \frac{\rho_{emitter}}{2e_t} \frac{b}{L} ln\left(\frac{6L}{3L+b}\right) \tag{4.12}$$

$$R_{Mi} = \int_{b/2-b/4+b^2/12L}^{b/2} \rho_{metal} \frac{dr}{rm_t} \frac{b}{L} = \frac{\rho_{metal}}{2m_t} \frac{b}{L} ln\left(\frac{6L}{3L+b}\right)$$

for i =1,3, and

$$R_{Si} = \frac{\rho_{emitter}}{2e_t} \frac{L}{b} ln\left(\frac{3}{2}\right) \tag{4.13}$$

$$R_{Mi} = \frac{\rho_{metal}}{2m_t} \frac{L}{b} ln\left(\frac{3}{2}\right)$$

for i=2,4.

Semiconductor resistance temperature dependence has been taken into account through the following linearized PSPICE model:

$$R(T) = R(T_{NOM}) \cdot R \cdot \left(1 + TC(T - T_{NOM})\right) \tag{4.14}$$

where R is a resistance multiplier, whose default value is 1, T_{NOM} is the nominal temperature, which is set to 27°C and TC is a temperature coefficient of resistance calculated on the basis of data reported in [50] and shown in the graphs 4.5 and 4.6.

Metal resistance variation with temperature has also been taken into account by choosing a constant value of TCR, equal to $38 \cdot 10^{-4}$ $°C^{-1}$.

5 CONCENTRATOR SOLAR CELL BEHAVIOUR UNDER UNEVEN ILLUMINATION PROFILES

Concentrating Photovoltaic systems (CPV) exploit optical components to focus the light gathered by a large-area collector onto relatively-small area PV receivers. The PV receiver may be either a single high-efficiency device or an array of cells usually connected in series. In both cases the irradiance profile of the caustic generated by the solar concentrator has a strong influence on the performance of the PV receiver. As has been widely demonstrated in [2] and in Chapter 2, uniform irradiance profiles allows for the best cell performance, while uneven irradiance profiles might lead to both a significant increase of series resistance and a reduction of the photogenerated current.

In this chapter we will introduce an innovative simulation tool which combines electrical device-level simulations through the above presented distributed model and optical simulations on the concentrator through ZEMAX-EE software, by ZEMAX Corp., a professional optical design software based on ray-tracing. In this way it's possible to assess the performance of a Concentrating Photovoltaic system as a whole in its real operative conditions.

5.1 ZEMAX MAIN FEATURES

Ray-tracing is a wide applicable technique for modeling the propagation of light through an optical system. The modeling of light propagation via ray-tracing is commonly called geometrical optics.

ZEMAX can operate in two main modes: sequential and non-sequential. In sequential ray-tracing rays are traced through a pre-defined sequence of surfaces while traveling from the object surface to the image surface. Rays hit each surface once in the order (sequence) in which the surfaces are defined. Imaging systems are well described by sequential surfaces. Sequential ray-tracing is numerically fast and is extremely useful for the design, optimization and tolerancing of such systems. Aberration calculations and diffraction calculations can be easily performed using sequential ray-tracing. Many conventional optical systems can be classified as imaging systems. These include photographic objectives, telephoto lenses, microscopes and telescopes.

The other main working mode of ZEMAX is non-sequential. Non-sequential ray-tracing implies that there is no predefined sequence of surfaces which rays that are being traced must hit. The objects that the rays hit are determined solely by the physical positions and properties of the objects as well as the directions of the rays. Rays may hit any part of any non-sequential object, and may hit the same object multiple times, or not at all. This can be contrasted with sequential ray tracing where all of the rays traced must propagate through the same set of surfaces in the same order.

In sequential mode in ZEMAX, all ray propagation occurs through surfaces which are located using a local coordinate system. In non-sequential mode, optical components are modeled as true three-dimensional objects, either as surfaces or solid volumes. Each object is placed globally at an independent *x, y, z* coordinate with an independently defined orientation.

The non-sequential ray tracing capabilities of ZEMAX do not suffer from the same limitations that sequential ray tracing does. Since rays can propagate through the optical components in any order, ,total internal reflection ray paths can be accounted for. While sequential mode is limited to the analysis of imaging systems, non-sequential mode can be used to analyze stray light, scattering and illumination in both imaging and non-imaging systems, such as the major part of solar concentrators.

Non-sequential ray tracing can be modeled in ZEMAX using one of two modes:

- Pure non-sequential ray tracing
- Mixed sequential / non-sequential ray tracing

When using pure non-sequential ray tracing, all optics to be traced are in a single non-sequential group. In addition, source and detector objects are setup within the group to launch and capture rays, respectively. The source modeling capabilities of pure non-sequential mode in ZEMAX are far more comprehensive than sequential mode. In sequential mode, you are limited to modeling point sources located on the object surface. Using the image analysis capabilities of sequential mode, planar extended sources located at the object surface can be modeled. Using pure non-sequential ray tracing, sources can be placed anywhere in the non-sequential group, at any orientation, and can even be placed inside of other objects. The source objects themselves can range from simple point sources (like those used in sequential mode) to complex, three-dimensional source distributions.

Rays from non-sequential sources, known as NSC rays, can be split and scattered by optical components. The analysis options available when tracing NSC rays include evaluating radiometric data on detectors and the storing of ray data in ray database files. Detectors can be modeled as planar surfaces, curved surfaces and even three-dimensional volumes. Non-sequential detectors support the display of a variety of data types including: incoherent irradiance, coherent irradiance, coherent phase, radiant intensity and radiance. Ray database files store the history of each ray traced. Ray paths can be filtered to isolate rays that hit specific objects.

When using mixed sequential / non-sequential ray tracing (also known as hybrid or mixed ray tracing), a collection of non-sequential objects are setup inside of a non-sequential group. This non-sequential group is part of a larger sequential system. Sequentially traced rays enter the non-sequential group through an entrance port, and exit the group through an exit port to continue propagating through the sequential system. Multiple non-sequential groups may be defined in the same sequential system, and any number of objects may be placed in each non-sequential group. This allows non-sequential components such as faceted mirrors, roof prisms or CAD objects to be included in a sequential design.

5.2 CASE STUDIES

In this study we considered three different types of concentrator optics: a Fresnel lens, a parabolic mirror and a Freeform mirror. They are characterized by significantly different flux distributions in the focal region. In particular, the Fresnel lens - being made out of PMMA – is strongly affected by chromatic aberration, while mirror-based systems have no wavelength dependence of the focal distribution. Each CPV concentrator has been simulated by non-sequential ray tracing and the irradiance maps on the focal plane have been collected into multispectral datacubes. Figure 5.1 [55] shows a shaded layout of the Fresnel lens and Freeform mirror systems.

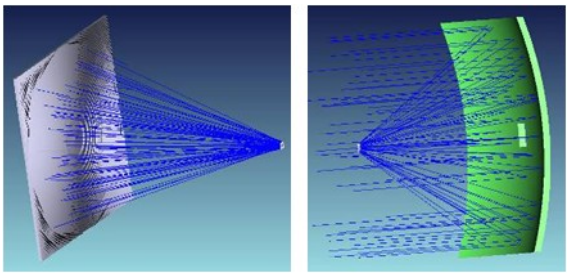

Figure 5.1 Shaded layout of Fresnel lens system (left) and Freeform mirror system (right)

The three concentrators have been chosen with a focal length of 200 mm and F/1 speed. Non sequential mode allows to take into account complex effects, such as ray-splitting at interfaces, polarization, scattering by surfaces and material bulk, which generate stray light and might affect significantly the focal spot distribution, especially in high-concentration systems.

The solar source has been represented in ZEMAX with a Dynamic Link Library (DLL) launching random rays within specific spectral bands, having spectral distribution according to AM 1.5d spectrum and angular distribution according to real sunshape [56]. A limb darkening factor of 0.8 has been considered [57,58], while the effects of circumsolar ratio have been neglected.

We chose to run the ray tracing simulations within 14 different wavebands, each one having 50 nm spectral width and central wavelength ranging from 400 to 1050 nm. As a preliminary operation we optimized the position of the PV receiver for the highest collection flux within the whole spectral range. The irradiance maps generated by ZEMAX have then been calculated and collected into multispectral datacubes. These bundles of irradiance maps describes completely the focusing property of each concentrator at the PV receiver plane. Figure 5.2 shows the irradiance maps of Fresnel lens calculated at 400, 850 and 1050 nm, while Figure 5.3 shows a comparison between the irradiance map of the parabolic mirror versus freeform concentrator, calculated at 850 nm. The color scale of the pictures is normalized in arbitrary units. The comparison shown in Figure 5.3 highlights the strong

difference in irradiance distribution uniformity between parabolic mirror and freeform mirror. Figure 5.4 shows the total irradiance profiles incident onto the receiver plane for the three concentrators. Despite of the very different illumination profiles, the average concentration ratio is almost the same, about 460 X. This allows us to perform a fair comparison of the three concentrators.

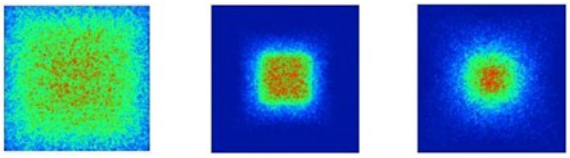

Figure 5.2 Fresnel lens irradiance maps calculated at 400 nm (left), 850 nm (center) and 1050 nm (right)

Figure 5.3 Parabolic mirror (left) and freeform mirror (right) irradiance maps calculated at 850 nm

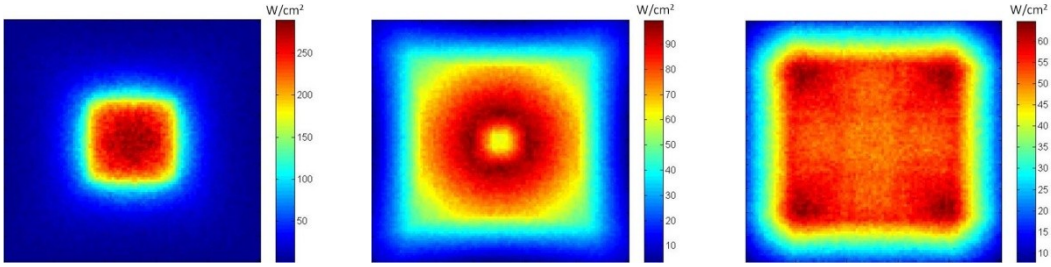

Figure 5.4 Total irradiance profile incident onto the receiver plane for Fresnel lens (top left), parabolic mirror (top right) and Freeform mirror (bottom)

5.3 PV DEVICE MODEL

The PV device we considered for this simulation is a silicon cell for high concentration with an active area of 7×7 mm^2. The small dimension of the device might lead to the hypothesis that the cell can be described by a simple one or two-diode model [59], but this is not the case for high concentration CPV systems. The strong radiant flux entering the PV receiver and the uneven irradiance distribution make the division of the device into smaller dimension elements a mandatory issue. This approach has been followed for large area or thin-film devices where the ohmic losses across the contact grid cannot be neglected.

The above procedure for the model implementation has then been followed. A non-uniform binning of the surface has been carried out in order to reduce the number of elementary cells in the simulation.

The smallest feature size in concentration PV cells are the front metal contacts (fingers) having a width ranging from 5 to 15 μm. A uniform binning of the whole surface of the device (7×7 mm^2 in size) with a few μm pitch would have led to a huge number of elementary cells and to unacceptably long computational times.

A solar cell sample has been chosen and a spectral response (SR) measurement has been performed using a calibrated tungsten lamp and a set of interference filters with a bandwidth of 10 nm FWHM (full width at half maximum). A white light bias with a color temperature of 6500 K has been added during the measurement; the irradiance of the bias light was 300 W/m^2. The calculation of the current density maps has been carried out using the irradiance maps collected into the datacubes. For each waveband we multiplied the corresponding irradiance map by the SR at the central wavelength. The datacube obtained by this operation has been summed into a single current density map. The current map has then been calculated by simple integration of the current density map over the surface of each non-uniform bin. It represents the actual photocurrent distribution profile injected into the corresponding PV device. Figure 5.5 shows the current map for each CPV system and highlights the current unevenness due to hotspots in the irradiance profiles. The dark lines represent the front contact grid pattern, where no current generation occurs. A conventional comb-like front contact grid pattern has been chosen, composed of a number of parallel vertical fingers. In addition, two busbars have been placed at the upper and lower sides of the cell. Front contact grid pattern is clearly shown in Figure 5.6. Current has been extracted by the two busbars all along their length.

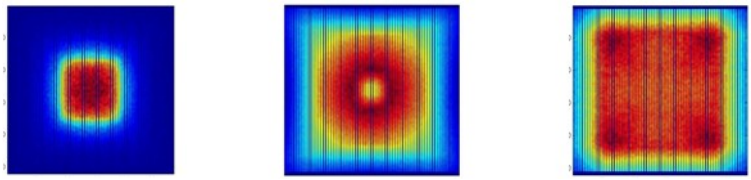

Figure 5.5 Current map for the system based on Fresnel lens (center), parabolic mirror (center) and freeform mirror (right)

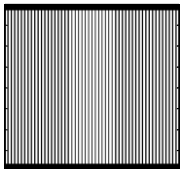

Figure 5.6 The comb-like front contact grid pattern with two busbars

Here are reported the main geometrical and electrical parameters used for the simulations:

- cell area 7×7 mm^2
- metallization coverage 10%
- finger width 10 μm

- finger height 5 μm
- busbar width 100 μm
- pitch (finger spacing) 130 μm
- emitter resistivity $\rho_{emitter}$ $5 \cdot 10^{-3}$ Ω·cm
- ρ_{bulk} $2 \cdot 10^{-2}$ Ω·cm
- ρ_{metal} $1.59 \cdot 10^{-6}$ Ω·cm
- $\rho_{contact}$ $5 \cdot 10^{-7}$ Ω·cm^2

Physical effects described in Chapter 4 have not been included in the simulations, due to the unavailability of parameters for this concentration level. Furthermore, temperature was supposed to be equal to 27°C. Therefore, simulation results will include only the effects of ohmic losses on cell performance. These will be discussed in the next Section.

5.4 SIMULATION RESULTS

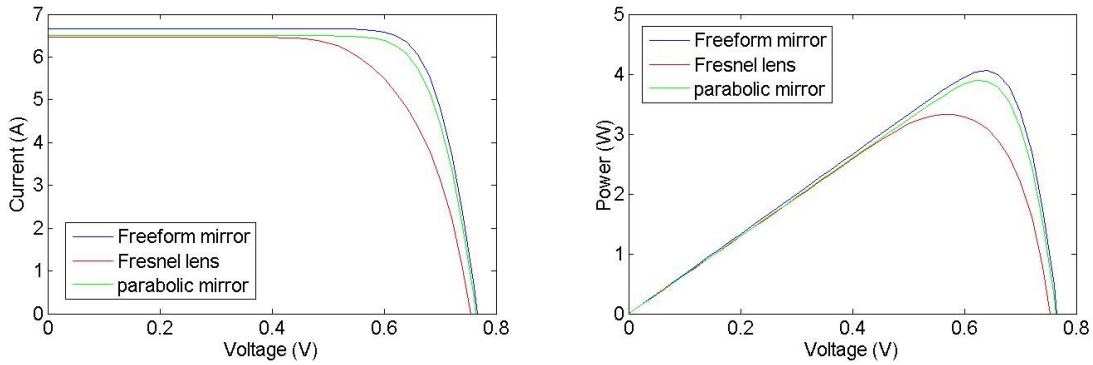

Figure 5.7 IV curves (left) and power curves (right) for the three concentrators

Figure 5.7 shows IV curves and power curves obtained from simulations for the three concentrators. As can be seen from the plots, the short-circuit current values are very similar, even though Freeform mirror have a short-circuit current value slightly greater than the others. However, there is a much greater difference in maximum power delivered by the cell in the three cases; in particular, the Freeform mirror provides a power value 22% greater than the Fresnel lens and 4.6% than the parabolic mirror. Fill factor confirms this behaviour since found values are 79.64% for the Freeform mirror, 68.36% for the Fresnel lens and 78.49% for the parabolic mirror. Such a difference cannot be explained only in terms of a difference in short-circuit current but involves a different impact of ohmic losses in the three cases. Emitter voltage maps, shown in Figure 5.8, help us to better understand the working conditions of the cell, since they show the voltage drop across the emitter and the ohmic contacts of the PV receivers in operative conditions, i.e. at maximum power point.

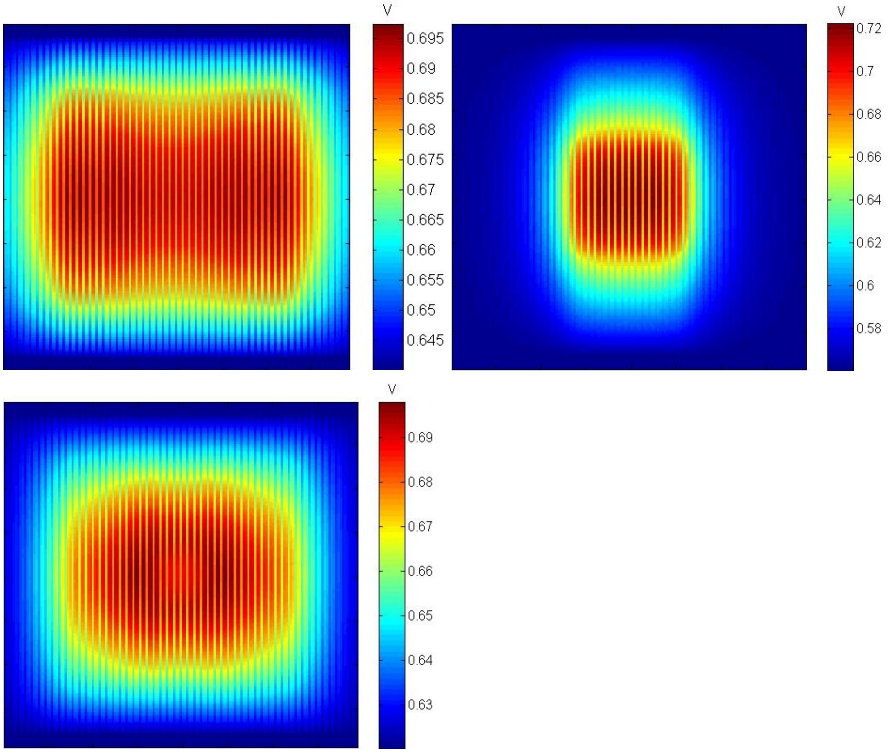

Figura 5.8 Voltage maps at the emitter surface calculated at the maximum power point, for Freeform mirror (top left), Fresnel lens (top right) and parabolic mirror (bottom)

In the case of Fresnel lens, the central region of the cell has a 150 mV bias higher than the maximum power voltage and thus, as has been extensively discussed in Chapter 2, his contribution to the current generation of the device is negligible. On the opposite, Freeform mirror and, to some extent, parabolic mirror generate an irradiance distribution smooth enough to reduce the voltage drop across the emitter down to 50-60 mV. In this way, the whole surface of the PV receivers operates at a bias very close to the maximum power voltage, leading to better performances. Table 5.1 summarizes the main parameters of the simulation results. The quantity C_{ratio} is defined as maximum to minimum irradiance ratio on the PV receivers. As can be seen from the Table, the Fresnel lens has a C_{ratio} considerably higher than parabolic and freeform mirrors which is consistent with the higher voltage drop across the emitter.

Table 5.1 Main simulation results

	I_{sc} (A)	V_{oc} (V)	P_{max} (W)	FF (%)	C_{ratio}
Fresnel lens	6.46	0.753	3.33	68.36	6.29
Parabolic mirror	6.49	0.763	3.89	78.49	2.13
Freeform mirror	6.66	0.765	4.07	79.64	1.55

6 ANALYSIS OF NON-CONVENTIONAL FRONT CONTACT PATTERNS IMPACT ON CONCENTRATOR SOLAR CELLS PERFORMANCES

Ohmic losses phenomena in concentrator solar cells strongly depend on front contact grid pattern; in particular they depend on the materials it is made of and on its geometrical arrangement. Especially at high concentration ratios the choice of front contact grid geometry becomes of crucial importance since it has a key role in extracting photogenerated current.

Optimal front contact grid geometry is a trade-off between two opposite needs: minimizing resistivity of the paths connecting the various current generation points on the cell surface to the current extraction point and, contemporarily, minimizing total cell coverage.

In [60] an approach based on the constructal theory is proposed to design the grid pattern in a photovoltaic solar cell.

In this Chapter we will apply our distributed electrical model to the analysis of concentrator solar cells performances in the presence of different types of front contact geometries. Furthermore we will propose a novel contact geometry, whose structure will be derived from geometrical considerations, and its performance will be compared to the other patterns.

Even though shadowing problem due to the presence of contacts can be overcome by the adoption of interdigitated back contacts, as is shown in Figure 6.1, the resulting solar cell design is much more complex. This is contrary to our aim, i.e. improving cell performances by means of a technological process relatively simple and cheap.

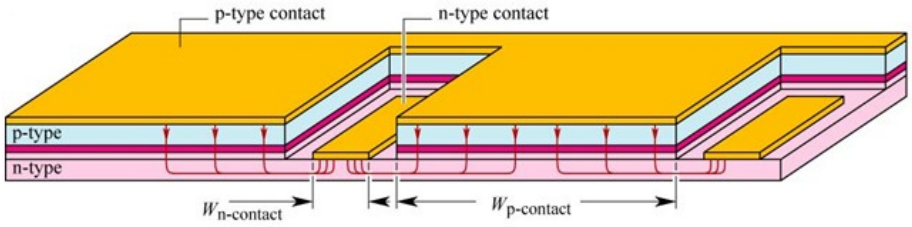

Figure 6.1 Interdigitated back-contact structure in a concentrator solar cell

For this reason our analysis will be limited to conventional front contact grid structures.

Following an idea presented for the first time in [54], we will introduce a front contact grid pattern characterized by a fractal structure.

6.1 BASICS OF FRACTALS

Fractal geometry is a very wide field, closely connected to physical non linear systems [61, 62]. In this section we just want to delineate its basic features. A fractal is a subset of R^n which is autosimilar and whose fractal dimension is usually greater than its topological dimension. Topological dimension is always an integer number and can be defined in the following way:

Definition: A subset S has a "k" topological dimension if every point in S has arbitrarily close neighbors, whose edges intersect S in a set of "k-1" dimension, and "k" is the minimum integer number that satisfy this condition.

Fractal dimension is a generalization of the previous concept and can be defined as:

Definition: A set S is called affine autosimilar if S can be divided into k subsets, each of which can be magnified by a M factor, reproducing S.

Definition: Fractal dimension of an affine autosimilar set S is defined as:

$$D = \frac{log(k)}{log(M)} \tag{6.1}$$

Fractal dimension concept is strictly connected to free path concept. From theory of free paths by diffusion in Euclidean d-dimensional structures [63], we have:

$$P(r,t) \sim t^{-d/2} exp(-r^2/t) \tag{6.2}$$

that gives the probability of returning to the starting point after some time:

$$P(0,t) \sim t^{-d/2} \tag{6.3}$$

The 2 factor in the above expression is characteristic of Euclidean structures and is a particular value of a magnitude called *free path* d_w. In general for a fractal $d_w > 2$; this can be easily understood thinking of how the complexity of a fractal structure leads to a longer walk for an hypothetical traveler placed on this structure with respect to an Euclidean structure to cover the same distance. In general the probability of returning to the starting point becomes:

$$P(0,t) \sim t^{-D/d_w} \tag{6.4}$$

Given that $D/d_w < d/2$, $P(0,t)$ is lower for fractal grids than for Euclidean ones.

A geometrical fractal can be constructed by iteration, in such a way that autosimilarity condition is satisfied. In this way it's possible to create structures which can be used as capillary front metallization for concentrator solar cells, contextually limiting the cell coverage.

The Koch snowflake, shown in Figure 6.2, is a fractal with strange geometrical properties: it is a closed figure constructed by an infinite number of iteration which has an infinite perimeter and can be enclosed in a figure with a finite perimeter. This is due to the fact that the perimeter is a divergent succession, while the area is a convergent series. This property can be useful for our purposes, since

the perimeter of the contact grid is related to its current collection capabilities, while the area is related to the metal coverage.

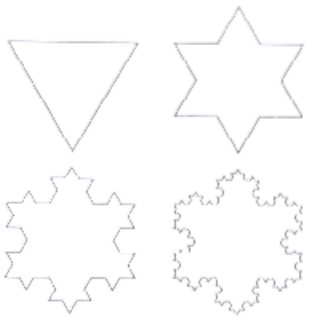

Figure 6.2 The first 4 steps of the construction of the Koch snowflake

6.2 IMPLEMENTED CONTACT GEOMETRY

The model we are searching for minimizes the paths of the charge carriers to reach the contacts and has properties of autosimilarity. An interesting group of geometrical figures is constituted by Bravais lattices in two dimensions, i.e. groups of figures each of which can fill a surface; they are triangles, rhombs, rectangles and hexagons. Among them the figure that guarantees the shortest mean path for a particle randomly generated in it to reach the perimeter, for given area and perimeter, is the hexagon. Unfortunately hexagon cannot be divided into smaller hexagons so that it completely fills the space. Square has this property and therefore a geometry with a square as its fundamental unit has been considered.

Figure 5.3 shows the resulting grid at the fourth order of iteration. Such a figure is also defined linearly autosimilar, because it is exactly the same at different scales. If *a* is the so called contraction factor of the figure, for consistency of the autosimilarity it has to be $a < {}^{1}/_{2}$, because if $a = {}^{1}/_{2}$ there would no place for contacts which separates, at the zero order of the iterative procedure of construction of the figure, the main structure into 4 squares. An isotropic structure in two dimensions has been considered, i.e. the contraction factor *a* is the same in the two directions. In particular, for the grid in Figure 5.3, *a = 0.4958.*

The contraction factor is characteristic of the system because it determines the dimensions of the squares at every iteration level. The other fundamental parameter of the structure is the magnification factor M, which has already been introduced for the definition of fractal dimension; in this case it is M = 2, which together with k =4 gives:

$$D = \frac{log(4)}{log(2)} = 2 \tag{6.5}$$

as fractal dimension, like a plane.

This seeming incongruity can be explained if we consider the structure showed in Figure 6.3 but in the case of an infinite number of autosimilarity levels; it can be shown that when this number tends to infinity the total area of the squares (the regions free of contacts) tends to zero, while the total contact area tends to

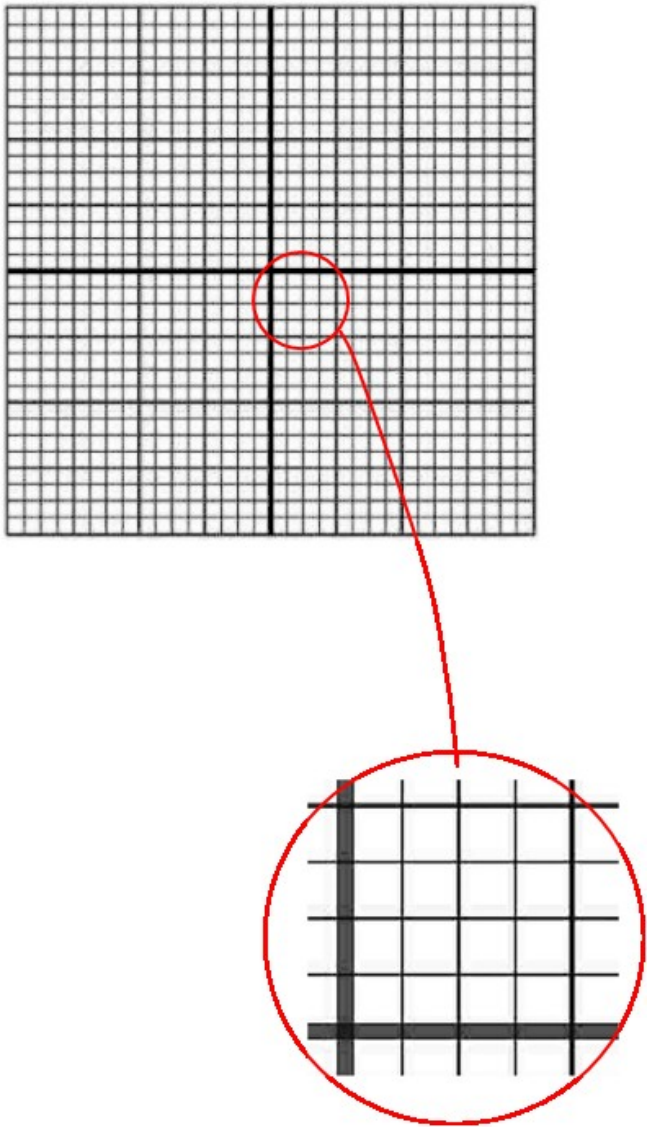

Figure 6.3 The proposed contact grid; the magnified particular shows 4 of the 5 autosimilarity levels of the figure

the entire area of the main structure.

Furthermore, it can be shown that the figure perimeter, when the number of autosimilarity levels N tends to infinity, diverges. The possibility to have a great area of collection is a desired feature.

The most important magnitude in defining the model is the contact width at n_{th} order of iteration, d_n: it is given by

$$d_n = a^n d \tag{6.6}$$

where d is the contact width at zero order of iteration.

As contact width at zero order has been chosen $d = 5\mu m$, since it is a common value in concentrator solar cells. If we choose N = 4 we find the following values of contact width at successive autosimilarity levels: *10 μm, 20 μm, 40 μm, 80 μm.* The contact structure has been simulated and resulting cell performances have been compared to the performances obtained with different types of front contact grid patterns.

6.3 CASE STUDIES

The purpose of this work is the assessment of silicon solar cell performances in the presence of different types of front contact grid patterns, at a medium concentration factor, i.e. 50 X [64].

Three types of front contact grid patterns have been considered: a conventional comb-like pattern, composed of a number of vertical fingers, which is shown in the top left side of Figure 6.4, a square-like pattern, which is usually implemented by STMicroelectronics and Emcore in their high efficiency concentrator solar cells, shown in the top right part of Figure 6.4 and the above presented fractal pattern, shown again in the lower part of Figure 6.4.

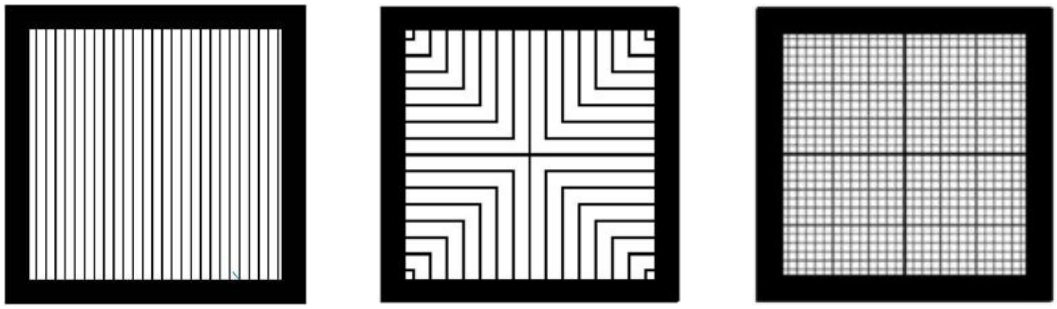

Figure 6.4 The three contact grid patterns considered: comb-like pattern (top left), square-like pattern (top right) and fractal pattern (bottom)

As can be seen from the Figure 6.4, a 100 μm-thick metallic frame has been applied to the cell perimeter in order to improve the charge carrier collection.

Current was supposed to be extracted by the four midpoints of the cell sides. Table 6.1 reports the main parameters used for the simulations. Diode ideality factor, inverse saturation current density and short-circuit current density have been chosen according to [42], from Table 3.1.

Temperature was supposed to be equal to 27°C.

Table 6.1 Parameter values used for the simulations

junction ideality factor	1.163
temperature	300 K
energy band gap	1.12 eV
short circuit current density	1.4 A / cm^2
concentration factor	50X
emitter resistivity	30 Ω / □
emitter thickness	300 nm
metal resistivity (Aluminium)	$4 \cdot 10^{-6}$ Ω·cm
metallization thickness	5 μm
bulk resistivity	1.5 Ω·cm
bulk thickness	250 μm
metal-semiconductor contact resistivity	$1 \cdot 10^{-6}$ Ω·cm^2

Three values of cell dimensions have been considered: $1 \times 1\ cm^2$, $1.5 \times 1.5\ cm^2$ and $2 \times 2\ cm^2$. For each structure and for each cell dimension value, geometrical parameters such as finger width, finger spacing, cell coverage and number of autosimilarity levels have been varied in order to reach the optimal condition in terms of power delivered by the cell. Simulation results have then been compared.

6.4 SIMULATION RESULTS

The first group of simulations has been performed for a $1 \times 1\ cm^2$ cell. Table 6.2 reports the optimized geometrical parameters of the three contact geometries and simulation results in terms of output power and fill factor. Figure 6.5 shows power curves for the three cases. Fractal pattern slightly overcomes the two other structures in terms of output power and fill factor, with an improvement of 1.5% with respect to the comb pattern and 2.3% with respect to the square-like one.

Increasing cell dimensions to $1.5 \times 1.5\ cm^2$ optimal geometrical configurations of the three structures have been found to be the ones reported in Table 6.3. In this case the previously observed performance gaps increase to 12.3% and 5.8%, respectively. Power curves for a $1.5 \times 1.5\ cm^2$ are shown in Figure 6.6.

The last group of simulations has been performed for a $\mathbf{2 \times 2\ cm^2}$ cell; in this case the fractal pattern provides an output power 13.8% higher than the square-like one and comb-like pattern results haven't

been reported because they turned out to be far worse than the others. Geometrical parameters and simulation results for this case study are shown in Table 6.4 and Figure 6.7, respectively.

Table 6.2 Optimized geometrical parameters of the three structure for a $\mathbf{1 \times 1}\ \boldsymbol{cm^2}$ cell

1 cm x 1 cm cell		P_{max} (mW)	FF (%)
comb-like	w_{finger} = 5 µm coverage = 5%	690	72.3
fractal	N = 4 w_{finger} = 5-10-20-40-80 µm coverage = 5%	700.7	75.9
square-like	w_{finger} = 5 µm coverage = 5%	684.6	71.8

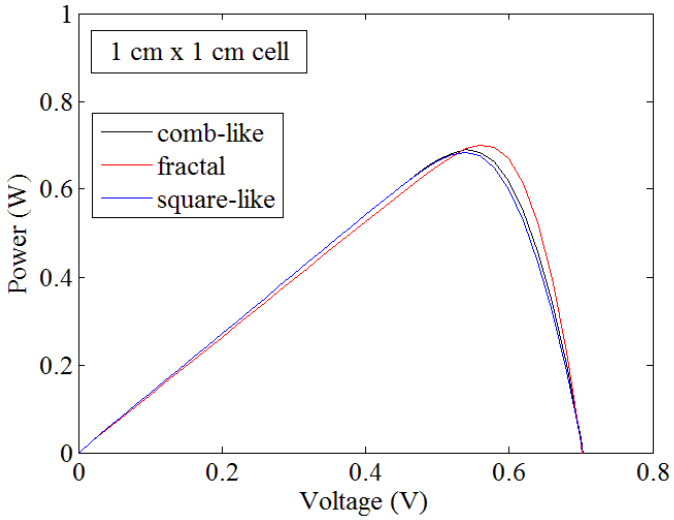

Figure 6.5 Power curves for the three structures, for a $\mathbf{1 \times 1}\ \boldsymbol{cm^2}$ cell

The increasing performance gap at increasing cell dimensions is due to the fact that in a bigger cell photogenerated charge carriers must follow longer paths to reach the contacts and therefore the front contact grid pattern assumes more importance in limiting the voltage drop across the emitter and the contacts. Voltage maps of the cell surface help us to gain an insight into cell working conditions.

Figure 6.8 shows voltage maps for the three structure for a $1 \times 1\ cm^2$ cell.

In this case the voltage drop across the emitter is quite small in all three cases, even though in some small regions of the comb-like pattern case it reaches about 50 mV. In general voltage distribution appears more uniform in the fractal and square-like cases.

If we move to consider the case of a $1.5 \times 1.5\ cm^2$ cell, shown in Figure 6.9, we can see that voltage drop across the emitter is obviously increased, but while for the fractal pattern it is nearly 50 mV, it

Table 6.3 Optimized geometrical parameters of the three structures for a $\mathbf{1.5 \times 1.5}\ \boldsymbol{cm^2}$ cell

1.5 cm x 1.5 cm cell		P_{max} (W)	FF (%)
comb-like	w_{finger} = 10 µm coverage = 10%	1.3	63.9
Fractal	N = 4 w_{finger} = 5-10-20-40-80 µm coverage = 5%	1.46	68.1
square-like	w_{finger} = 10 µm coverage = 9%	1.38	67.1

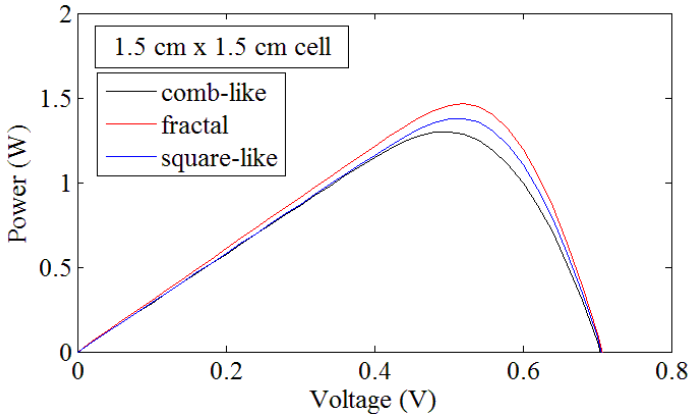

Figure 6.6 Power curves for the three structures, for a $\mathbf{1.5 \times 1.5}\ \boldsymbol{cm^2}$ cell

Table 6.4 Optimized geometrical parameters of square-like structure and fractal structure for a $\mathbf{2 \times 2}\ \boldsymbol{cm^2}$ cell

2 cm x 2 cm cell		P_{max} (W)	FF (%)
fractal	N = 5 w_{finger} = 10-20-40-80 µm coverage = 15%	2.31	67.3
square-like	w_{finger} = 20 µm coverage = 16%	2.03	60.3

reaches more than 60 mV for the square-like pattern and more than 100mV for the comb-like pattern. A so high potential drop in considerable areas of the cell implies a substantial decrease in current produced by the cell at maximum power point. The absence of an horizontal path for electrons to reach the contacts plays an important role in the performance worsening of the comb-like pattern.

Lastly, Figure 6.10 shows voltage maps in the case of a $2 \times 2\ cm^2$. Their inspection reveals a much more uniform voltage distribution in the fractal case than in the square-like case. In the first case the potential drop on the emitter is around 80 mV in almost the entire cell while in the second case, even though some small regions work at a voltage very close to the maximum power point, the major part

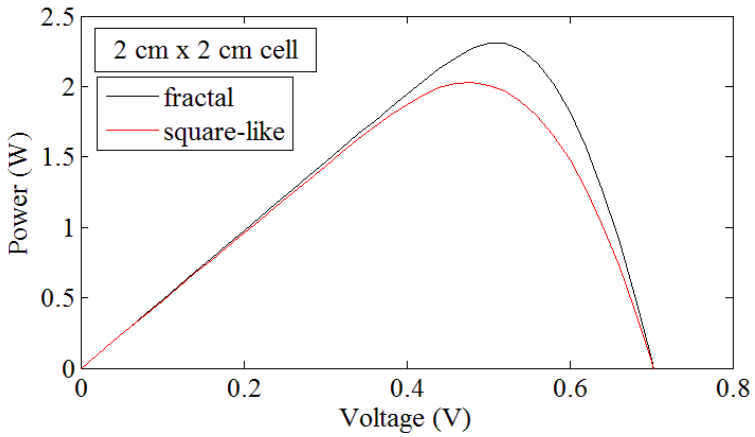

Figure 6.7 Power curves for square-like structure and fractal structure, for a $\mathbf{2 \times 2}\ \boldsymbol{cm^2}$ cell

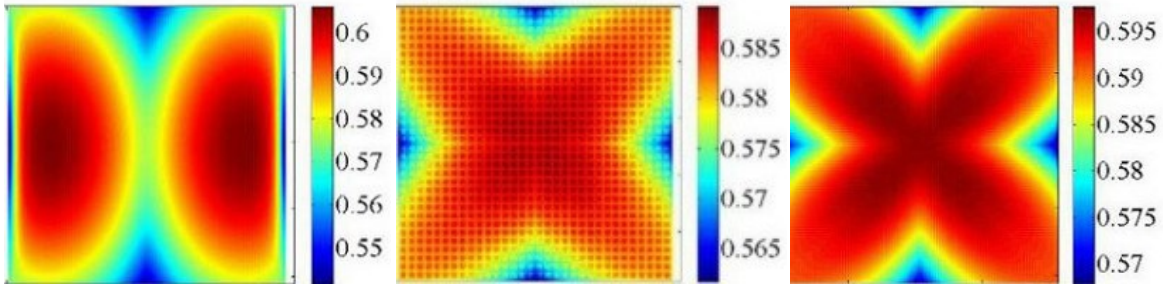

Figure 6.8 Voltage maps for comb-like (top left), fractal (top right) and square-like (bottom) patterns for a $\mathbf{1 \times 1}\ \boldsymbol{cm^2}$cell

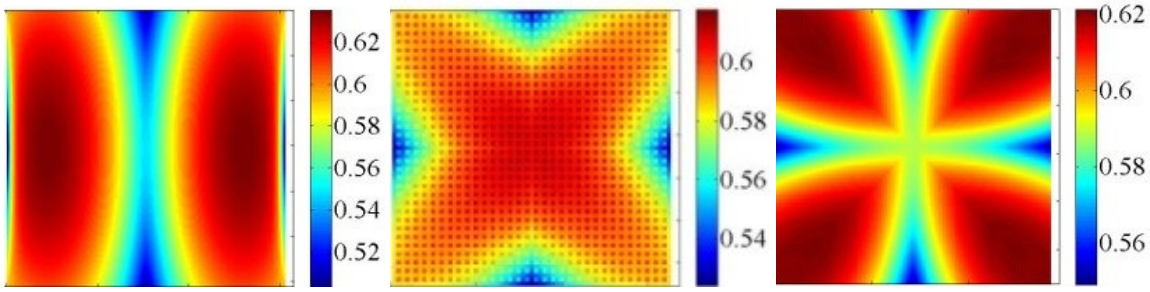

Figure 6.9 Voltage maps for comb-like (top left), fractal (top right) and square-like (bottom) patterns for a $\mathbf{1.5 \times 1.5}\ \boldsymbol{cm^2}$ cell

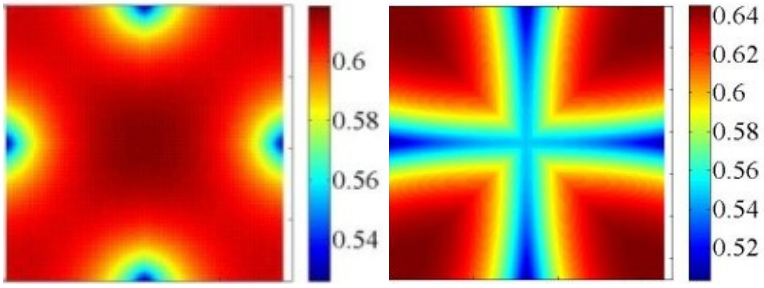

Figure 6.10 Voltage maps for fractal (left) and square-like (right) patterns for a $\mathbf{2 \times 2}\ \boldsymbol{cm^2}$ cell

of the cell operates at a voltage at least 120 mV higher and thus his contribution to the current generation is negligible.

7 ANALYSIS OF VOID FORMATION EFFECTS IN CONCENTRATOR SILICON SOLAR CELLS SOLDERED TO METAL CORE PRINTED CIRCUIT BOARD (MC-PCB)

Soldering processes in both microelectronic and photovoltaic fields are often affected by the formation of voids at the device-substrate interface. Voids formation may either be due to a bad soldering process, or arise as a result of thermomechanical stress introduced during device operation [65, 66]. These voids have a deleterious effect on heat sinking capabilities of the device [67] because they produce a local decrease in thermal conductivity in the solder region that leads to a local increase in the device working temperature. This in turn can lead to a further formation of voids. In the photovoltaic field, and especially under concentration conditions, solar cells periodically undergo a very high thermal load, so an assessment of the impact of the void formation on the solar cell temperature distribution and performances can be very useful.

In this chapter a joint thermal-electrical numerical analysis of void formation effects is presented; it combines thermal simulations performed by using ADINA 8.7 (Automatic Dynamic Incremental Nonlinear Analysis) software and electrical simulations by using PSPICE software. The purpose of this work is the assessment of the thermal and electrical performances of the PV receiver of a Concentrating Photovoltaic system constituted by a substrate which also acts as a heat sink and a concentrator silicon solar cell which is soldered to it, in the presence of a real-case void distribution in the solder joint.

Simulations have also been carried out for two other artificious distributions of voids, in particular a 2×2 and a 10×7 void matrix, and results have been compared.

The CPV system is constituted by a primary and a secondary concentrator in Cassegrain configuration, with an optical rod as tertiary element, providing a concentrating factor of 100 X. The shaded layout of the system is shown in Figure 7.1 [66]. The power effectively incident onto the receiver has been calculated supposing a concentrator optical efficiency of 75% and a cell conversion efficiency of 20%. Concentration factor of 100 X refers to standard direct normal irradiance (DNI) value of 850 W/m^2. In this way the incident power onto the cell is equal to 13.57 W.

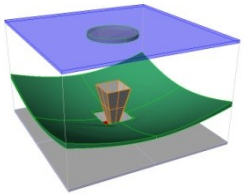

Figure 7.1 Shaded layout of the Cassegrainian concentrator

7.1 PRELIMINARY EXPERIMENTAL MEASUREMENTS

Four commercially available silicon solar cells (each of them with an area of 1.9 cm × 1.4 cm) have been soldered to a metal core printed circuit board (MC-PCB), in particular an IMS substrate (insulated metal substrate) for electrical connection, also acting as a heat spread element. Figure 7.2 shows the structure of such a substrate. It is made of a metal baseplate (aluminum is commonly used because of its low cost and density) covered by a thin layer of dielectric (usually an epoxy-based layer) and a layer of copper (with a thickness usually less than one hundred microns).

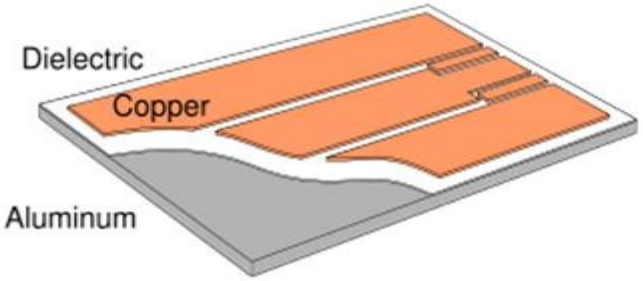

Figure 7.2 Structure of an IMS substrate consisting of a metal baseplate covered by a thin layer of dielectric and a layer of copper

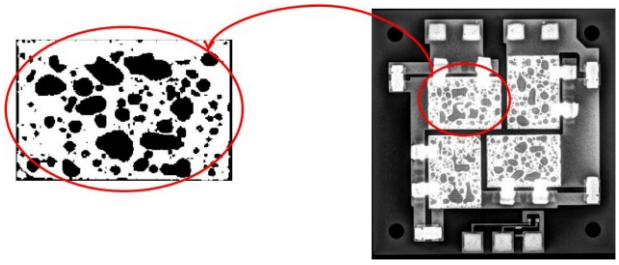

Figure 7.3 Void maps for the four cells obtained by X-ray inspection. The inset on the left side of the figure shows a magnified image of one of them

In an IMS substrate heat produced by an apparatus is transferred to a metallic mass thermally connected to it, but electrically insulated. This metallic mass constitutes the substrate on which the apparatus is mounted. It also allows to easily mount further heat sinking fins or fans. The sinking capabilities of such a structure are obviously limited by the presence of the dielectric which reduces the total thermal conductivity, but this effect is not so high since dielectric is usually realized increasing its thermal conductivity value. FR4 is often used as dielectric in IMS substrates with a thickness on the order of one hundred microns.

Soldering process has been carried out by a lead-free Sn/Ag eutectic solder paste in such a way that a great number of voids have arisen. Subsequently, a void map for the four cells has been obtained by

X-ray inspection. Figure 7.3 shows the four X-ray maps for the four cells.

7.2 THERMAL SIMULATIONS

One of these maps has been used as input parameters for a thermal finite element analysis (FEA), carried out by means of ADINA 8.7 software. In particular, the entire structure constituted by the cell and the IMS substrate have been modeled and simulated by means of this software. Assuming a fixed temperature of the bottom layer of the stack, i.e. the aluminum layer, and representing the voids as regions with a very low value of thermal conductivity, temperature maps of the cell surface have been obtained as a result. Such maps, for the real-case distribution, are shown in Figure 7.4 for two different values of temperature of the lowest layer, which we can consider as the heat sink temperature, exhibit hot spots in correspondence to each void. Figure 7.5 shows temperature maps for a 2×2 void matrix and a 10×7 void matrix, for a sink temperature of 45°C.

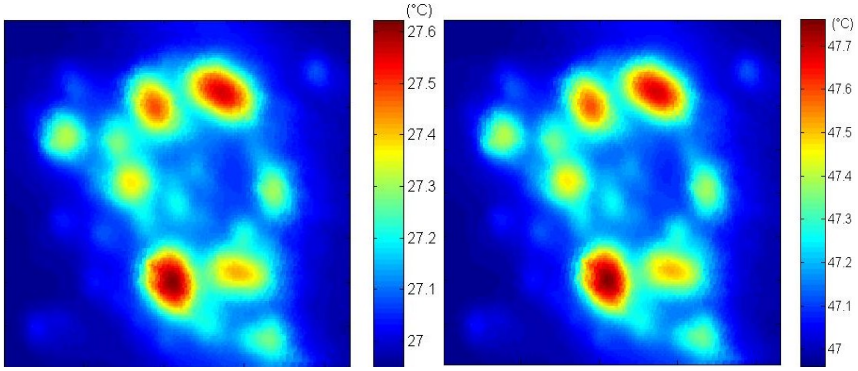

Figure 7.4 Temperature map of the cell surface for two different temperatures of sink, 25°C (left) and 45°C (right), for a real-case void distribution

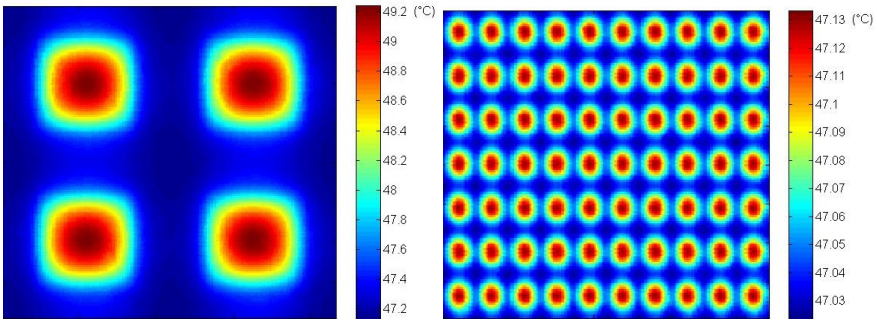

Figure 7.5 Temperature map of the cell surface for two different void distributions, a 2×2 void matrix (left) and a 10×7 void matrix (right), for a 45°C sink temperature

Simulations have also been carried out for other values of sink temperature, i.e. 25°C, 27°C, 35°C, 45°C and 65°C. It is interesting to note that temperature difference between the bottom layer and a point of the surface free of voids, which is about 2°C in Figure 7.4, slightly increases at increasing the temperature of the bottom layer. Analogously, also temperature distortion at the surface, which can be expressed as the difference between maximum and minimum temperature, increases at increasing sink temperature. For example, for a sink temperature of 25°C, temperature difference at the surface is about 0.6°C and it raises to more than 0.7°C for a sink temperature of 45°C. Furthermore, temperature distortion increases at increasing void dimensions. For example, difference between maximum temperature at the center of a void and minimum temperature on the cell surface reaches about 2°C for a 2×2 void matrix and only 0.1°C for a 10×7 void matrix.

7.3 ELECTRICAL MODEL

Although voids are localized in the solder joint region, in the electrical simulations they have been equivalently represented as discontinuities in the connection between solar cell back contact and ground. To this end, solar cell back contact layer, which had previously considered as an equipotential surface, has been modeled analogously to the emitter, by adding four resistances in each grid subcell.

A binary void map, i.e. a rectangular array whose values are equal to zero in correspondence of void regions and one otherwise, has been used to take into account the void distribution in the electrical simulations.

In order to include into the simulations the temperature distortion effect due to void presence the previously obtained temperature maps of the cell surface have then been used as input parameters in the PSPICE model that has been presented in this thesis.

In this way electrical parameters such as semiconductor layers resistivity and p-n junction inverse saturation current have been tuned depending on specific temperature value of each grid element. For this purpose TCR (temperature coefficient of resistance) values for emitter and bulk layers have been used as a function of dopant concentrations according to [50]. These values are also shown in Figures 3.12 and 3.13. A constant value of TCR (not dependent on temperature) equal to $38 \cdot 10^{-4}$ $°C^{-1}$ has also been used for metal (aluminum) resistance dependence on temperature.

A comb-like front contact grid pattern, composed of 10 μm-wide 5 μm-thick fingers and two 700 μm-wide busbars, for a total coverage of 15%, has been chosen. Current was supposed to extracted by two 3 mm-wide pads from one side of the cell.

Table 7.1 reports the main parameters values used for the electrical simulations.

7.4 ELECTRICAL SIMULATIONS

The first series of simulations have been performed for the real void distribution. Figure 7.6 shows power curves of the cell for different values of sink temperature while Figure 7.7 shows the decrease

Table 7.1 Parameters used for the electrical simulations

cell dimensions	1.9 cm x 1.4 cm
short-circuit current density	3 A/cm^2
emitter resistivity	30 Ω/□
bulk resistivity	1 Ω·cm
concentration factor	100X
metal-semiconductor resistivity	$1 \cdot 10^{-6}$ Ω·cm^2
metal resistivity	$2.82 \cdot 10^{-6}$ Ω·cm
emitter thickness	300 nm
bulk thickness	250 μm

in maximum power delivered by the cell as a function of sink temperature.

This performance worsening is mainly due to the decrease in the open circuit voltage caused by junction inverse saturation current increase with temperature.

Figure 7.8 shows a comparison of cell performances with and without voids. Because of the fact that, as has been previously pointed out, thermal simulations revealed that for a given value of sink temperature surface temperature (i.e. cell temperature) is about 2°C higher, in order to produce a fair comparison, each electrical simulation result obtained in the case of the presence of voids has been compared to the case of the absence of voids for the right surface temperature value; simulation results show that voids presence doesn't affect cell performances noticeably.

Simulations performed for the other two voids distributions, i.e. a 2×2 void matrix and a 10×7 void matrix, didn't produce an appreciable difference in cell performances which turned out to be substantially independent on void distribution, because of the very low back contact resistivity.

Electrical simulations also revealed that the voids presence causes a current crowding effect around them, in the regions of the cell back contact that lie just over the voids perimeter, as shown in Figure 7.9 for real void distribution and 2×2 void matrix, and in Figure 7.10 for 10×7 void matrix. As can be seen from the Figures, current density reaches very high values ($\approx 10^4$-10^5 A/cm^2) and its value

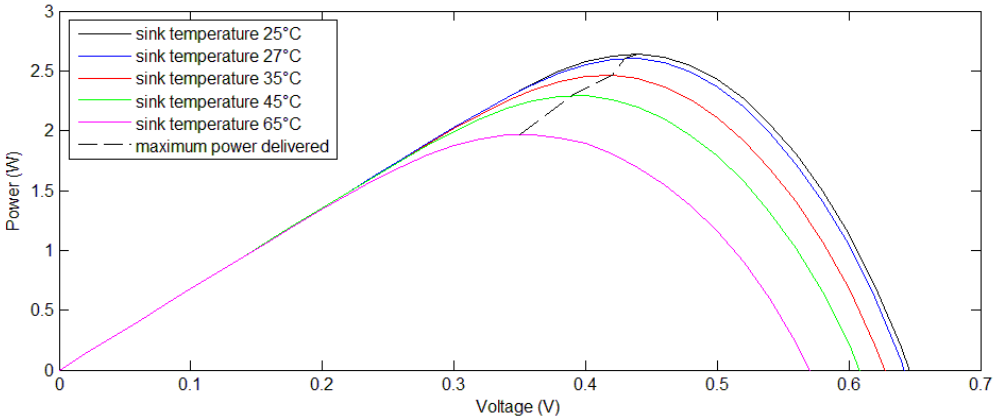

Figure 7.6 Power curves of the cell for different sink temperature values for a real void distribution

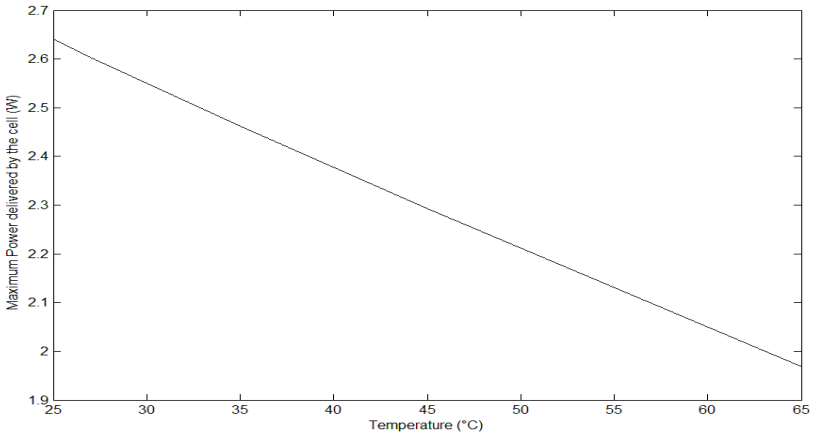

Figure 7.7 Maximum power delivered by the cell as a function of temperature

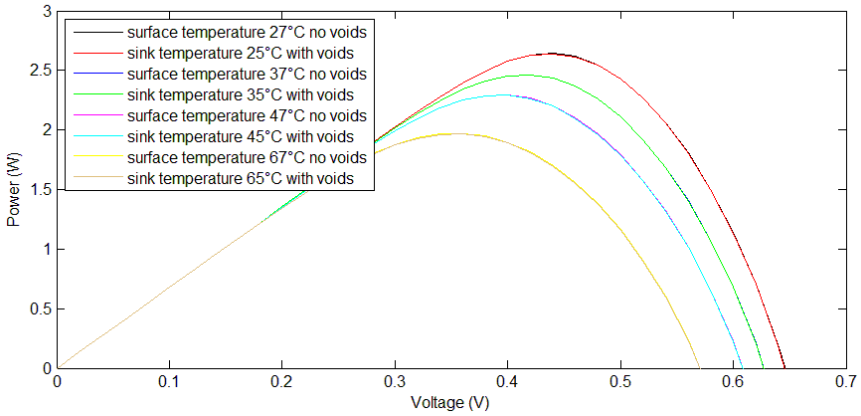

Figure 7.8 Comparison of cell power curves with and without voids for several values of sink temperature

increases at increasing void dimension. However, current density flowing in the cell turned out to be uniform, due to the current spreading effect of the cell back contact.

Such high current densities shown in Figures 7.9 and 7.10 could induce a localized cell heating because

of Joule effect, or even cause electromigration. It would be worth investigating these effects in a future work.

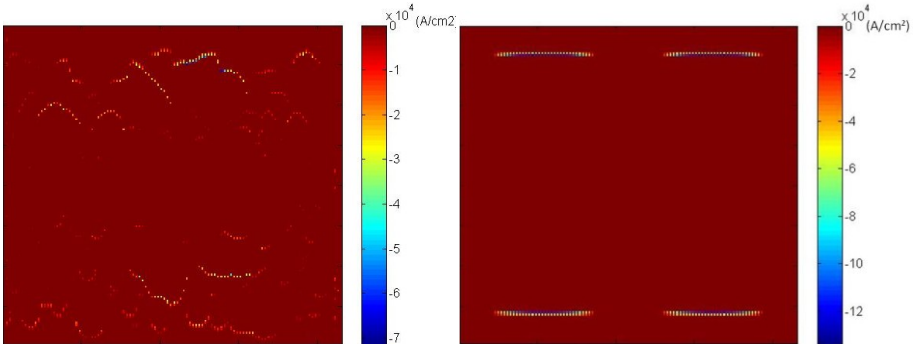

Figure 7.9 Current density flowing from cell back contact to ground for the real void distribution (left) and a 2×2 void matrix (right); a current crowding around voids is visible

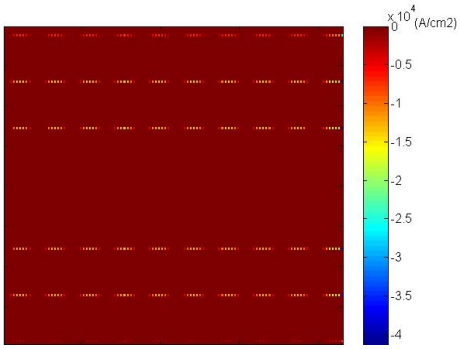

Figure 7.10 Current density flowing from cell back contact to ground for a 10×7 void matrix; a current crowding around voids is visible

APPENDIX A

A.1 MATLAB SOURCE CODE

As has been widely explained in Chapter 4, the 2.5D distributed model presented in this thesis is based on a MATLAB source code, which generates a PSPICE netlist containing the solar cell circuit description. In particular, a MATLAB script, which can be considered the main program, and two MATLAB functions have been developed.

The MATLAB script provides for the construction of the grid of elements, calculation of some electrical parameters involved in the simulation, such as resistor values, and the creation of a .txt file containing the description of the entire circuit. Each electrical element in the circuit is represented as a code line in the .txt file, using the PSPICE syntax. The MATLAB script also provides for the connection between elements and the choice of the current extraction points.

The I-V curve is traced performing a voltage sweep between 0 V and a fixed voltage value (typically less than 1 V for silicon cells).

A.1.1 MATLAB SCRIPT

Here are reported some extracts from the code which illustrate the main steps of the model implementation. Comments (in green in the code) explain the meaning of each part of the code.

```
k=1.38e-23; %Boltzmann constant
q=1.602e-19; %electron charge
T=300;  %temperature
JS=1.58e-12;   %saturation current density
N=1;   %ideality factor
VJ=0.96;   %junction potential
EG=1.12; %energy gap
Lcell=0.7;   %cell length
Wcell=0.7;   %cell width
areatot=Lcell*Wcell;   %cell area
IS=JS*areatot;   %saturation current
hmetal=5e-4;   %finger thickness in cm
remitter=30;   %emitter resistivity in ohm/[]
hemitter=3e-5;   %emitter thickness in cm
rmetal=1.59e-6;   %metal resistivity in ohm*cm
```

```
rcontact=1e-6;   %contact resistivity in ohm*cm^2
rbulk=0.02;   %bulk resistivity in ohm*cm
hbulk=0.04;   %bulk thickness in cm
.
.
.

%a prompt dialog box allows to set some simulation parameters
prompt={'finger width (in cm):','busbar width (in cm):','coverage (from 0
to 1):',...
    'number of semiconductor elements divisions between fingers:','number
of busbar elements in vertical:'};
name='comb-like simulation parameters';
defaultanswer={'10e-4','100e-4','0.1','1','6'}; %default values
answer=inputdlg(prompt,name,1,defaultanswer,'on');
largh_finger=str2num(cell2mat(answer(1)));
largh_busbar=str2num(cell2mat(answer(2)));
copertura=str2num(cell2mat(answer(3)));
n_div_semi_x=str2num(cell2mat(answer(4)));
n_div_busbar_y=str2num(cell2mat(answer(5)));
.
.
.
%call to the function correnti which realizes the non-linear binning and
%calculate the current map for the grid
%it returns several parameters among which the grid dimensions M and P
[M P n_finger current_map temp_matrix_interp XI YI
aree]=correnti(largh_busbar,largh_finger,copertura,n_div_semi_x,n_div_busba
r_y);
.
.
.
%call to the function griglia which returns a binary matrix representing
the front contact pattern geometry
[griglia]=crea_maschera(M,P,spaziatura,n_div_busbar_y);
.
.
.
```

```
%current values in the subcells covered by metallization are set to 0
mappa_correnti=current_map.*griglia;
.
.
.
% this double for cycle calculates the active area of the cell
for i=1:M,
    for j=1:P,
        if griglia(i,j)==1
            area_attiva=area_attiva+aree(i,j);
        end
    end
end

%coverage is then calculated in order to check for errors (it has to
%coincide with the value set in the prompt)
coverage=(areatot-area_attiva)/(areatot);
.
.
.
%arrays containing TCR (temperature coefficients of resistance) values as a
function of temperature are loaded
load TCR_n_type_mean_10e18;
load TCR_p_type_mean_1e16;
.
.
.
fid=fopen('prova.cir','w');   %the netlist file is created
.
.
.
%emitter resistances model instances and front metal resistances model
instances are placed in the circuit
%Node names in the circuit are composed of three numbers: the first two
numbers represent the position of the grid element to which the resistor
belongs, and the third number identifies the type of resistor in the
electrical circuit of the subcell, i.e. emitter resistor, bulk resistor...
```

```
%emitter resistance models are created depending on the value of TCR and
%temperature of each grid element
for i=2:M,
    for j=2:P,
        if griglia(i,j)==0
            fprintf(fid,'R%.3i%.3i1 %.3i%.3i5 %.3i%.3i3 Rmetal%.3i%.3i1
%e\n',i,j,i,j,i-1,j,i,j,Rmetal_1(i,j));
            fprintf(fid,'R%.3i%.3i2 %.3i%.3i5 %.3i%.3i2 Rmetal%.3i%.3i2
%e\n',i,j,i,j,i,j,i,j,Rmetal_2(i,j));
            fprintf(fid,'R%.3i%.3i3 %.3i%.3i5 %.3i%.3i3 Rmetal%.3i%.3i3
%e\n',i,j,i,j,i,j,i,j,Rmetal_1(i,j));
            fprintf(fid,'R%.3i%.3i4 %.3i%.3i5 %.3i%.3i2 Rmetal%.3i%.3i4
%e\n',i,j,i,j,i,j-1,i,j,Rmetal_2(i,j));
        else
            fprintf(fid,'R%.3i%.3i1 %.3i%.3i5 %.3i%.3i3 Rcell%.3i%.3i1
%.2f\n',i,j,i,j,i-1,j,i,j,Rsemi_1(i,j));
            fprintf(fid,'R%.3i%.3i2 %.3i%.3i5 %.3i%.3i2 Rcell%.3i%.3i2
%.2f\n',i,j,i,j,i,j,i,j,Rsemi_2(i,j));
            fprintf(fid,'R%.3i%.3i3 %.3i%.3i5 %.3i%.3i3 Rcell%.3i%.3i3
%.2f\n',i,j,i,j,i,j,i,j,Rsemi_1(i,j));
            fprintf(fid,'R%.3i%.3i4 %.3i%.3i5 %.3i%.3i2 Rcell%.3i%.3i4
%.2f\n',i,j,i,j,i,j-1,i,j,Rsemi_2(i,j));
        end
    end
end
%back contact resistances are placed in the circuit
%analogously to the emitter resistances
for i=2:M,
    for j=2:P,
            fprintf(fid,'Rback%.3i%.3i8 %.3i%.3i7 %.3i%.3i10
Rmetal%.3i%.3i1 %e\n',i,j,i,j,i-1,j,i,j,Rmetal_1(i,j));
            fprintf(fid,'Rback%.3i%.3i9 %.3i%.3i7 %.3i%.3i9 Rmetal%.3i%.3i2
%e\n',i,j,i,j,i,j,i,j,Rmetal_2(i,j));
            fprintf(fid,'Rback%.3i%.3i10 %.3i%.3i7 %.3i%.3i10
Rmetal%.3i%.3i3 %e\n',i,j,i,j,i,j,i,j,Rmetal_1(i,j));
            fprintf(fid,'Rback%.3i%.3i11 %.3i%.3i7 %.3i%.3i9
Rmetal%.3i%.3i4 %e\n',i,j,i,j,i,j-1,i,j,Rmetal_2(i,j));
    end
end
```

```
% substrate resistances and metal-semiconductor resistances are placed in
the circuit
for i=1:M,
    for j=1:P,
        if griglia(i,j)==0
            fprintf(fid,'R%.3i%.3i5 %.3i%.3i6 %.3i%.3i5
%e\n',i,j,i,j,i,j,Rcontact(i,j));
        else
            fprintf(fid,'R%.3i%.3i5 %.3i%.3i6 %.3i%.3i5 Rcell%.3i%.3i5
%f\n',i,j,i,j,i,j,i,j,R5(i,j));
        end
    end
end
%current generators are set to their correct value and diodes model
%instances are placed in the circuit
      for i=1:M,
          for j=1:P,
        fprintf(fid,'I%.3i%.3i %.3i%.3i7 %.3i%.3i6
%e\n',i,j,i,j,i,j,mappa_correnti(i,j));
        fprintf(fid,'D%.3i%.3i %.3i%.3i6 %.3i%.3i7 DMOD%.3i%.3i
%f\n',i,j,i,j,i,j,i,j,aree(i,j)/areatot);
          end
      end
%through the use of matrix_void_interp it's possible to take into account
voids
%in the case of the presence of voids no electrical connection is provided
%between the back contact layer and ground
%in the case of the absence of voids a very low value resistor is placed
%between the back contact layer and ground
for i=1:M,
    for j=1:P,
        if matrix_void_interp(i,j)==1
            fprintf(fid,'R%.3i%.3i12 %.3i%.3i7 0 %e\n',i,j,i,j,Rbar(2));
        end
    end
end
% very high value resistor are placed on the edges of the cell in order to
% avoid floating nodes
for i=1:M-1,
```

```
    fprintf(fid,'Rbar%.3i0014 %.3i0014 %.3i0014 %.1e\n',i,i,i+1,Rbar(1));
    fprintf(fid,'Rbar%.3i%.3i2 %.3i%.3i2 %.3i%.3i2
%.1e\n',i,P,i,P,i+1,P,Rbar(1));
    fprintf(fid,'Rbar%.3i00111 %.3i00111 %.3i00111
%.1e\n',i,i,i+1,Rbar(1));
    fprintf(fid,'Rbar%.3i%.3i9 %.3i%.3i9 %.3i%.3i9
%.1e\n',i,P,i,P,i+1,P,Rbar(1));
end
for j=1:P-1,
    fprintf(fid,'Rbar001%.3i1 001%.3i1 001%.3i1 %.1e\n',j,j,j+1,Rbar(1));
    fprintf(fid,'Rbar%.3i%.3i3 %.3i%.3i3 %.3i%.3i3
%.1e\n',M,j,M,j,M,j+1,Rbar(1));
    fprintf(fid,'Rbar001%.3i8 001%.3i8 001%.3i8 %.1e\n',j,j,j+1,Rbar(1));
    fprintf(fid,'Rbar%.3i%.3i10 %.3i%.3i10 %.3i%.3i10
%.1e\n',M,j,M,j,M,j+1,Rbar(1));
end
.
.
.
% electrical connection of the current extracting points to the voltage
%source is provided: in this example current is extracted by the upper
%and lower sides of the cell in all their length
%other configurations can be easily implemented
for i=1:P,
    fprintf(fid,'Rbarsource001%.3i1 001%.3i1 999 %.1e\n',i,i,Rbar(2));
    fprintf(fid,'Rbarsource%.3i%.3i3 %.3i%.3i3 999
%.1e\n',M,i,M,i,Rbar(2));
end
.
.
.
fprintf(fid,'VL  999  0\n');     %the voltage source is connected to the
correct terminals
%resistance models are created depending on the specific values of TCR and
%temperature of each grid element
for i=1:M,
    for j=1:P,
    fprintf(fid,'.MODEL Rmetal%.3i%.3i1 RES TC1=%.3i
T_ABS=%f\n',i,j,TCR_metal,temp_matrix_interp(i,j));
```

```
    fprintf(fid,'.MODEL Rmetal%.3i%.3i2 RES TC1=%.3i
T_ABS=%f\n',i,j,TCR_metal,temp_matrix_interp(i,j));
    fprintf(fid,'.MODEL Rmetal%.3i%.3i3 RES TC1=%.3i
T_ABS=%f\n',i,j,TCR_metal,temp_matrix_interp(i,j));
    fprintf(fid,'.MODEL Rmetal%.3i%.3i4 RES TC1=%.3i
T_ABS=%f\n',i,j,TCR_metal,temp_matrix_interp(i,j));
    format short;
    fprintf(fid,'.MODEL Rcell%.3i%.3i1 RES TC1=%.3i
T_ABS=%f\n',i,j,TCR_emitter(find(int16(TCR_emitter(:,1)*10)==int16(temp_mat
rix_interp(i,j)*10)),2),temp_matrix_interp(i,j));
    fprintf(fid,'.MODEL Rcell%.3i%.3i2 RES TC1=%.3i
T_ABS=%f\n',i,j,TCR_emitter(find(int16(TCR_emitter(:,1)*10)==int16(temp_mat
rix_interp(i,j)*10)),2),temp_matrix_interp(i,j));
    fprintf(fid,'.MODEL Rcell%.3i%.3i3 RES TC1=%.3i
T_ABS=%f\n',i,j,TCR_emitter(find(int16(TCR_emitter(:,1)*10)==int16(temp_mat
rix_interp(i,j)*10)),2),temp_matrix_interp(i,j));
    fprintf(fid,'.MODEL Rcell%.3i%.3i4 RES TC1=%.3i
T_ABS=%f\n',i,j,TCR_emitter(find(int16(TCR_emitter(:,1)*10)==int16(temp_mat
rix_interp(i,j)*10)),2),temp_matrix_interp(i,j));
    fprintf(fid,'.MODEL Rcell%.3i%.3i5 RES TC1=%.3i
T_ABS=%f\n',i,j,TCR_bulk(find(int16(TCR_bulk(:,1)*10)==int16(temp_matrix_in
terp(i,j)*10)),2),temp_matrix_interp(i,j));
    end
end
%diode models are created
for i=1:M,
    for j=1:P,
        fprintf(fid,'.MODEL DMOD%.3i%.3i D VJ=%.2f IS=%.3e EG=%.2f N=%.2f
(T_ABS=%f)\n',i,j,VJ,IS,EG,N,temp_matrix_interp(i,j));   %questa è la
dichiarazione del modello PSPICE dei diodi
    end
end
fprintf(fid,'.DC VL 0 1 0.02\n');   %a voltage sweep is performed (in this
example between 0 V and 1 V with a 0.02 V step)
```

A.1.2 FUNCTION CORRENTI

The function correnti provides the non-linear binning of the cell surface taking as input parameters the geometrical parameters set in the dialog box.

Taking multispectral irradiance maps and multiplying them by the spectral response of the cell it calculates the current map containing the short-circuit current values generated by each element of the grid. This current map is then interpolated on the basis of the non-linear binning. Temperature map of the cell surface and void map are also interpolated on the basis of the non-linear binning.

Here are reported some extracts from the function code. Comments are reported in green in the code.

```
%the function uses as input parameters busbar width, finger width,
coverage, number of
%semiconductor elements between fingers in horizontal and number of busbar
elements in vertical
% the fucntion returns the grid dimensison M and P, the number of fingers,
% the interpolated current map, the interpolated temperature map, the
% matrices XI and YI which contain the non-linear binning of the cell
% surface and the matrix aree containing the area value of each element of
% the grid
function
[M,P,n_finger,mappa_correnti_interp,temp_matrix_interp,XI,YI,aree]=correnti
(largh_busbar,largh_finger,copertura,n_div_semi_x,n_div_busbar_y)
.
.
.
%total number of fingers is calculated
n_finger=round(1/(largh_finger*(Lcell-2*largh_busbar))*(areatot*copertura-
2*largh_busbar*Wcell));
%grid dimensions M and P are calculated
P=round(n_div_semi_x*(n_finger+1)+n_finger+2);
M=round(P*Lcell/Wcell);
.
.
.
% files containing the multispectral irradiance maps are opened and each of
%them is multiplied by the corresponding value of spectral response
% in this way a current map is produced
```

```
D=100;   %multispectral irradiance maps are represented as matrices of
%100x100 elements
files_si=dir('*nm.txt');
nfiles_si=size(files_si,1);
spec_resp_si=[0.239 0.2475 0.2778 0.3032 0.3218 0.3347 0.3539 0.3723 0.3908
0.4106 0.3982 0.3409 0.2358 0];
wavelenght_si=zeros(nfiles_si,1);
filesort_si=struct([]);
for i=1:nfiles_si,
    pos_nm_si=regexp(files_si(i).name,'nm');
    wave_si=files_si(i).name(pos_nm_si-4:pos_nm_si-1);
    wavelenght_si(i)=str2double(wave_si);
end
wavelenght_si=sort(wavelenght_si);
for i=1:nfiles_si,
    for j=1:nfiles_si,
        if findstr(num2str(wavelenght_si(i)),files_si(j).name)>0
            filesort_si=[filesort_si;files_si(j)];
        end
    end
end
mappa_corr_si=zeros(D,D);
pos_si=zeros(D,D);
irrad_si=zeros(D,D);
irradianza=0;
for m=1:nfiles_si,
    fid=fopen(filesort_si(m).name,'r');
    for i=1:24,
        line=fgets(fid);
    end
    for i=1:D,
        line=str2num(fgets(fid));
        irrad_si(i,1:D)=line(2:end);
    end
    irradianza=irradianza+irrad_si;
    mappa_corr_si=mappa_corr_si+irrad_si*spec_resp_si(m);
end
correntisi=mappa_corr_si*areatot/(D^2);
load temp_matrix;% the temperature map is loaded
```

```
load matrix_void;% the void map is loaded
.
.
.
%X, Y, X_temp, Y_temp, X_centri, Y_centri, X_temp_centri, Y_temp_centri
% provides a linear binning of the cell surface
dim=size(temp_matrix);
for i=1:D,
    for j=1:D,
        X(i,j)=j*Wcell/D;
    end
end
for i=1:dim(1),
    for j=1:dim(2),
        X_temp(i,j)=j*Wcell/dim(2);
    end
end

%it'more correct to consider the center of each subcell as the current
%generation point. To this end X_centri and Y_centri are created
for i=1:D,
    for j=2:D,
        X_centri(i,j)=X(i,j-1)+(X(i,j)-X(i,j-1))/2;
    end
end
for i=1:D,
    X_centri(i,1)=X(i,1)/2;
end
for i=1:dim(1),
    for j=2:dim(2),
        X_temp_centri(i,j)=X_temp(i,j-1)+(X_temp(i,j)-X_temp(i,j-1))/2;
    end
end
for i=1:dim(1),
    X_temp_centri(i,1)=X_temp(i,1)/2;
end

for i=1:D,
    for j=1:D,
```

```
        Y(j,i)=j*Lcell/D;
    end
end
for j=1:dim(2),
    for i=1:dim(1),
        Y_temp(i,j)=i*Lcell/dim(1);
    end
end

for i=2:D,
    for j=1:D,
        Y_centri(i,j)=Y(i-1,j)+(Y(i,j)-Y(i-1,j))/2;
    end
end
for j=1:D,
    Y_centri(1,j)=Y(1,j)/2;
end
for i=2:dim(1),
    for j=1:dim(2),
        Y_temp_centri(i,j)=Y_temp(i-1,j)+(Y_temp(i,j)-Y_temp(i-1,j))/2;
    end
end
for j=1:dim(2),
    Y_temp_centri(1,j)=Y_temp(1,j)/2;
end

% this part of the code provides a non-linear binning of the cell surface
XI=zeros(M,P);   %XI initialization

XIatt=[];   %XIatt initialization
for i=1:n_div_semi_x,
    v(i)=i*(Wcell/(n_finger+1)-largh_finger)/n_div_semi_x;
end
%the vector v maps the semiconductor space between two fingers
v(n_div_semi_x+1)=v(n_div_semi_x)+largh_finger;
for k=1:n_finger+1,   %XIatt is the extension of v to the entire length of
%the cell
        XIatt=[XIatt v];
        v=v+Wcell/(n_finger+1);
```

```
end
XIatt(end)=[];   %the last element is removed because it represents an
%element that doesn't exist
for i=1:n_div_semi_y,   %XIattiva maps the active region of the cell
%(between the two busbars)
XIattiva(i,1:P-2)=XIatt;
end

% at the left and right edges of the cell two half-fingers are placed
% in this way periodic structures can be simulated by simulating only a
% part of them. To do this:
XIattiva=XIattiva+largh_finger/2;  %XIattiva is right-shifted by
%largh_finger/2
% a column is added at the left of the matrix containing values equal to
% largh_finger/2
XIattiva=[ones(n_div_semi_y,1)*largh_finger/2 XIattiva];
% a column is added at the right of the matrix containing values equal to
% Wcell
XIattiva=[XIattiva ones(n_div_semi_y,1)*Wcell];
% the upper and lower parts of XI corresponding to busbars are created
for i=1:n_div_busbar_y,
    XI(i,:)=XIattiva(1,:);
    XI(M-i+1,:)=XIattiva(1,:);
end
%XIattiva is placed in the active region between the ttwo busbars
XI(n_div_busbar_y+1:M-n_div_busbar_y,:)=XIattiva;
%the first rows of YI in the region of busbar are created
for i=1:n_div_busbar_y,
        YI(i,1:P)=i*largh_busbar/n_div_busbar_y;
end

% the last rows of YI in the region of busbar are created
for i=M-n_div_busbar_y+1:M,
    for j=1:P,
        YI(i,j)=Lcell-largh_busbar+(i-
M+n_div_busbar_y)*largh_busbar/n_div_busbar_y;
    end
end
%Yiattiva maps the active region of the cell between the two busbars
```

```
for i=1:P,
    for j=1:n_div_semi_y,
        YIattiva(j,i)=largh_busbar+j*(Lcell-2*largh_busbar)/n_div_semi_y;
    end
end
%in the active region between the two busbars YI=YIattiva is set
YI(n_div_busbar_y+1:n_div_semi_y+n_div_busbar_y,1:P)=YIattiva;
%XI_centri and YI_centri have the same meaning of X_centri and Y_centri
for i=1:M,
    for j=2:P,
        XI_centri(i,j)=XI(i,j-1)+(XI(i,j)-XI(i,j-1))/2;
    end
end
for i=1:M,
    XI_centri(i,1)=XI(i,1)/2;
end
for i=2:M,
    for j=1:P,
        YI_centri(i,j)=YI(i-1,j)+(YI(i,j)-YI(i-1,j))/2;
    end
end
for j=1:P,
    YI_centri(1,j)=YI(1,j)/2;
end
%aree contains the area values of each element of the grid
aree(1,1)=XI(1,1)*YI(1,1);
for j=2:P,
    aree(1,j)=(XI(1,j)-XI(1,j-1))*YI(1,j);
end
for i=2:M,
    aree(i,1)=(YI(i,1)-YI(i-1,1))*XI(i,1);
end
for i=2:M,
    for j=2:P,
        aree(i,j)=(XI(i,j)-XI(i,j-1))*(YI(i,j)-YI(i-1,j));
    end
end
% the MATLAB function interp2 allows to calculate current density values in
% the points defined by matrices XI_centri e YI_centri, given the ones in
```

```
% points defined by X_centri e Y_centri
%the same procedure is applied to temperature map and void map
correnti_interp_si=interp2(X_centri,Y_centri,mappa_corr_si,XI_centri,YI_cen
tri,'spline');
temp_matrix_interp=interp2(X_temp_centri,Y_temp_centri,temp_matrix,XI_centr
i,YI_centri,'spline');
matrix_void_interp=interp2(X_temp_centri,Y_temp_centri,matrix_void,XI_centr
i,YI_centri,'spline');
```

A.1.3 FUNCTION CREA_MASCHERA

Here is reported the code of the function crea_maschera, which returns a binary matrix reproducing the front contact grid pattern. This is the case relative to the function creating a comb-like front contact grid pattern. Obviously, the function is different for different kinds of front contact grid patterns, such as fractal or square-like. The function uses as input parameters the total numbers of elements M and P, the number of elements between fingers and the number of semiconductor elements of busbar in the vertical direction.

```
function [maschera]=crea_maschera(M,P,spaziatura,n_div_busbar_y)
maschera_comb=ones(M,P); %a MxP matrix is initialized to 1
maschera_comb(:,1:spaziatura:end)=0;   %matrix elements corresponding to
%grid elements covered by metallization are set to 0
maschera_comb(1:n_div_busbar_y,:)=0;   %the upper busbar is created
maschera_comb(M-n_div_busbar_y+1:M,:)=0;%the lower busbar is created
```

A.2 PSPICE NETLIST

In this section a simple example of PSPICE netlist generated by the above presented code is given. The cell is divided into a grid of M x P elements, with M=4 and P=5.

% the first code line is always the title

CURVA IV comb

% in the first part of the code instances of resistor models are placed in every subcell of the circuit, starting from emitter resistors and back contact resistors. For example, resistor R0010011 is placed between nodes 0010015 and 0010011; his model is Rmetal0010011 and its value is 7.324082e-003.

R0010011 0010015 0010011 Rmetal0010011 7.324082e-003
R0010012 0010015 0010012 Rmetal0010012 7.324082e-005
R0010013 0010015 0010013 Rmetal0010013 7.324082e-003
R0010014 0010015 0010014 Rmetal0010014 7.324082e-005
Rback0010018 0010017 0010018 Rmetal0010011 7.324082e-003
Rback0010019 0010017 0010019 Rmetal0010012 7.324082e-005
Rback00100110 0010017 00100110 Rmetal0010013 7.324082e-003
Rback00100111 0010017 00100111 Rmetal0010014 7.324082e-005
R0020011 0020015 0010013 Rmetal0020011 5.053617e-001
R0020012 0020015 0020012 Rmetal0020012 1.061461e-006
R0020013 0020015 0020013 Rmetal0020013 5.053617e-001
R0020014 0020015 0020014 Rmetal0020014 1.061461e-006
R0030011 0030015 0020013 Rmetal0030011 5.053617e-001
R0030012 0030015 0030012 Rmetal0030012 1.061461e-006
R0030013 0030015 0030013 Rmetal0030013 5.053617e-001
R0030014 0030015 0030014 Rmetal0030014 1.061461e-006
R0040011 0040015 0030013 Rmetal0040011 7.324082e-003
R0040012 0040015 0040012 Rmetal0040012 7.324082e-005
R0040013 0040015 0040013 Rmetal0040013 7.324082e-003
R0040014 0040015 0040014 Rmetal0040014 7.324082e-005
Rback0020018 0020017 00100110 Rmetal0020011 5.053617e-001
Rback0020019 0020017 0020019 Rmetal0020012 1.061461e-006
Rback00200110 0020017 00200110 Rmetal0020013 5.053617e-001
Rback00200111 0020017 00200111 Rmetal0020014 1.061461e-006
Rback0030018 0030017 00200110 Rmetal0030011 5.053617e-001
Rback0030019 0030017 0030019 Rmetal0030012 1.061461e-006
Rback00300110 0030017 00300110 Rmetal0030013 5.053617e-001
Rback00300111 0030017 00300111 Rmetal0030014 1.061461e-006
Rback0040018 0040017 00300110 Rmetal0040011 7.324082e-003
Rback0040019 0040017 0040019 Rmetal0040012 7.324082e-005
Rback00400110 0040017 00400110 Rmetal0040013 7.324082e-003
Rback00400111 0040017 00400111 Rmetal0040014 7.324082e-005
R0010021 0010025 0010021 Rmetal0010021 7.725825e-006
R0010022 0010025 0010022 Rmetal0010022 6.943230e-002
R0010023 0010025 0010023 Rmetal0010023 7.725825e-006
R0010024 0010025 0010012 Rmetal0010024 6.943230e-002
R0010031 0010035 0010031 Rmetal0010031 3.662041e-003
R0010032 0010035 0010032 Rmetal0010032 1.464816e-004
R0010033 0010035 0010033 Rmetal0010033 3.662041e-003
R0010034 0010035 0010022 Rmetal0010034 1.464816e-004
R0010041 0010045 0010041 Rmetal0010041 7.725825e-006
R0010042 0010045 0010042 Rmetal0010042 6.943230e-002
R0010043 0010045 0010043 Rmetal0010043 7.725825e-006
R0010044 0010045 0010032 Rmetal0010044 6.943230e-002
R0010051 0010055 0010051 Rmetal0010051 7.324082e-003
R0010052 0010055 0010052 Rmetal0010052 7.324082e-005
R0010053 0010055 0010053 Rmetal0010053 7.324082e-003
R0010054 0010055 0010042 Rmetal0010054 7.324082e-005
Rback0010028 0010027 0010028 Rmetal0010021 7.725825e-006
Rback0010029 0010027 0010029 Rmetal0010022 6.943230e-002
Rback00100210 0010027 00100210 Rmetal0010023 7.725825e-006
Rback00100211 0010027 0010019 Rmetal0010024 6.943230e-002

Rback0010038 0010037 0010038 Rmetal0010031 3.662041e-003
Rback0010039 0010037 0010039 Rmetal0010032 1.464816e-004
Rback00100310 0010037 00100310 Rmetal0010033 3.662041e-003
Rback00100311 0010037 0010029 Rmetal0010034 1.464816e-004
Rback0010048 0010047 0010048 Rmetal0010041 7.725825e-006
Rback0010049 0010047 0010049 Rmetal0010042 6.943230e-002
Rback00100410 0010047 00100410 Rmetal0010043 7.725825e-006
Rback00100411 0010047 0010039 Rmetal0010044 6.943230e-002
Rback0010058 0010057 0010058 Rmetal0010051 7.324082e-003
Rback0010059 0010057 0010059 Rmetal0010052 7.324082e-005
Rback00100510 0010057 00100510 Rmetal0010053 7.324082e-003
Rback00100511 0010057 0010049 Rmetal0010054 7.324082e-005
R0020021 0020025 0010023 Rcell0020021 11.99
R0020022 0020025 0020022 Rcell0020022 22.64
R0020023 0020025 0020023 Rcell0020023 11.99
R0020024 0020025 0020012 Rcell0020024 22.64
R0020031 0020035 0010033 Rmetal0020031 2.526808e-001
R0020032 0020035 0020032 Rmetal0020032 2.122922e-006
R0020033 0020035 0020033 Rmetal0020033 2.526808e-001
R0020034 0020035 0020022 Rmetal0020034 2.122922e-006
R0020041 0020045 0010043 Rcell0020041 11.99
R0020042 0020045 0020042 Rcell0020042 22.64
R0020043 0020045 0020043 Rcell0020043 11.99
R0020044 0020045 0020032 Rcell0020044 22.64
R0020051 0020055 0010053 Rmetal0020051 5.053617e-001
R0020052 0020055 0020052 Rmetal0020052 1.061461e-006
R0020053 0020055 0020053 Rmetal0020053 5.053617e-001
R0020054 0020055 0020042 Rmetal0020054 1.061461e-006
R0030021 0030025 0020023 Rcell0030021 11.99
R0030022 0030025 0030022 Rcell0030022 22.64
R0030023 0030025 0030023 Rcell0030023 11.99
R0030024 0030025 0030012 Rcell0030024 22.64
R0030031 0030035 0020033 Rmetal0030031 2.526808e-001
R0030032 0030035 0030032 Rmetal0030032 2.122922e-006
R0030033 0030035 0030033 Rmetal0030033 2.526808e-001
R0030034 0030035 0030022 Rmetal0030034 2.122922e-006
R0030041 0030045 0020043 Rcell0030041 11.99
R0030042 0030045 0030042 Rcell0030042 22.64
R0030043 0030045 0030043 Rcell0030043 11.99
R0030044 0030045 0030032 Rcell0030044 22.64
R0030051 0030055 0020053 Rmetal0030051 5.053617e-001
R0030052 0030055 0030052 Rmetal0030052 1.061461e-006
R0030053 0030055 0030053 Rmetal0030053 5.053617e-001
R0030054 0030055 0030042 Rmetal0030054 1.061461e-006
R0040021 0040025 0030023 Rmetal0040021 7.725825e-006
R0040022 0040025 0040022 Rmetal0040022 6.943230e-002
R0040023 0040025 0040023 Rmetal0040023 7.725825e-006
R0040024 0040025 0040012 Rmetal0040024 6.943230e-002
R0040031 0040035 0030033 Rmetal0040031 3.662041e-003
R0040032 0040035 0040032 Rmetal0040032 1.464816e-004
R0040033 0040035 0040033 Rmetal0040033 3.662041e-003
R0040034 0040035 0040022 Rmetal0040034 1.464816e-004
R0040041 0040045 0030043 Rmetal0040041 7.725825e-006

R0040042 0040045 0040042 Rmetal0040042 6.943230e-002
R0040043 0040045 0040043 Rmetal0040043 7.725825e-006
R0040044 0040045 0040032 Rmetal0040044 6.943230e-002
R0040051 0040055 0030053 Rmetal0040051 7.324082e-003
R0040052 0040055 0040052 Rmetal0040052 7.324082e-005
R0040053 0040055 0040053 Rmetal0040053 7.324082e-003
R0040054 0040055 0040042 Rmetal0040054 7.324082e-005
Rback0020028 0020027 00100210 Rmetal0020021 5.330819e-004
Rback0020029 0020027 0020029 Rmetal0020022 1.006265e-003
Rback00200210 0020027 00200210 Rmetal0020023 5.330819e-004
Rback00200211 0020027 0020019 Rmetal0020024 1.006265e-003
Rback0020038 0020037 00100310 Rmetal0020031 2.526808e-001
Rback0020039 0020037 0020039 Rmetal0020032 2.122922e-006
Rback00200310 0020037 00200310 Rmetal0020033 2.526808e-001
Rback00200311 0020037 0020029 Rmetal0020034 2.122922e-006
Rback0020048 0020047 00100410 Rmetal0020041 5.330819e-004
Rback0020049 0020047 0020049 Rmetal0020042 1.006265e-003
Rback00200410 0020047 00200410 Rmetal0020043 5.330819e-004
Rback00200411 0020047 0020039 Rmetal0020044 1.006265e-003
Rback0020058 0020057 00100510 Rmetal0020051 5.053617e-001
Rback0020059 0020057 0020059 Rmetal0020052 1.061461e-006
Rback00200510 0020057 00200510 Rmetal0020053 5.053617e-001
Rback00200511 0020057 0020049 Rmetal0020054 1.061461e-006
Rback0030028 0030027 00200210 Rmetal0030021 5.330819e-004
Rback0030029 0030027 0030029 Rmetal0030022 1.006265e-003
Rback00300210 0030027 00300210 Rmetal0030023 5.330819e-004
Rback00300211 0030027 0030019 Rmetal0030024 1.006265e-003
Rback0030038 0030037 00200310 Rmetal0030031 2.526808e-001
Rback0030039 0030037 0030039 Rmetal0030032 2.122922e-006
Rback00300310 0030037 00300310 Rmetal0030033 2.526808e-001
Rback00300311 0030037 0030029 Rmetal0030034 2.122922e-006
Rback0030048 0030047 00200410 Rmetal0030041 5.330819e-004
Rback0030049 0030047 0030049 Rmetal0030042 1.006265e-003
Rback00300410 0030047 00300410 Rmetal0030043 5.330819e-004
Rback00300411 0030047 0030039 Rmetal0030044 1.006265e-003
Rback0030058 0030057 00200510 Rmetal0030051 5.053617e-001
Rback0030059 0030057 0030059 Rmetal0030052 1.061461e-006
Rback00300510 0030057 00300510 Rmetal0030053 5.053617e-001
Rback00300511 0030057 0030049 Rmetal0030054 1.061461e-006
Rback0040028 0040027 00300210 Rmetal0040021 7.725825e-006
Rback0040029 0040027 0040029 Rmetal0040022 6.943230e-002
Rback00400210 0040027 00400210 Rmetal0040023 7.725825e-006
Rback00400211 0040027 0040019 Rmetal0040024 6.943230e-002
Rback0040038 0040037 00300310 Rmetal0040031 3.662041e-003
Rback0040039 0040037 0040039 Rmetal0040032 1.464816e-004
Rback00400310 0040037 00400310 Rmetal0040033 3.662041e-003
Rback00400311 0040037 0040029 Rmetal0040034 1.464816e-004
Rback0040048 0040047 00300410 Rmetal0040041 7.725825e-006
Rback0040049 0040047 0040049 Rmetal0040042 6.943230e-002
Rback00400410 0040047 00400410 Rmetal0040043 7.725825e-006
Rback00400411 0040047 0040039 Rmetal0040044 6.943230e-002
Rback0040058 0040057 00300510 Rmetal0040051 7.324082e-003
Rback0040059 0040057 0040059 Rmetal0040052 7.324082e-005

Rback00400510 0040057 00400510 Rmetal0040053 7.324082e-003
Rback00400511 0040057 0040049 Rmetal0040054 7.324082e-005

% now bulk resistors and metal-semiconductor resistors are placed in each subcell of the circuit

R0010015 0010016 0010015 1.000000e-001
R0010025 0010026 0010025 1.054852e-004
R0010035 0010036 0010035 5.000000e-002
R0010045 0010046 0010045 1.054852e-004
R0010055 0010056 0010055 1.000000e-001
R0020015 0020016 0020015 1.449275e-003
R0020025 0020026 0020025 Rcell0020025 0.061151
R0020035 0020036 0020035 7.246377e-004
R0020045 0020046 0020045 Rcell0020045 0.061151
R0020055 0020056 0020055 1.449275e-003
R0030015 0030016 0030015 1.449275e-003
R0030025 0030026 0030025 Rcell0030025 0.061151
R0030035 0030036 0030035 7.246377e-004
R0030045 0030046 0030045 Rcell0030045 0.061151
R0030055 0030056 0030055 1.449275e-003
R0040015 0040016 0040015 1.000000e-001
R0040025 0040026 0040025 1.054852e-004
R0040035 0040036 0040035 5.000000e-002
R0040045 0040046 0040045 1.054852e-004
R0040055 0040056 0040055 1.000000e-001

% in this part of the code current generators (identified by the letter I in the code) and instances of the diode models (identified by the letter D in the code) are placed in the circuit

I001001 0010017 0010016 0.000000e+000
D001001 0010016 0010017 DMOD001001 0.000004
I001002 0010027 0010026 0.000000e+000
D001002 0010026 0010027 DMOD001002 0.003564
I001003 0010037 0010036 0.000000e+000
D001003 0010036 0010037 DMOD001003 0.000008
I001004 0010047 0010046 0.000000e+000
D001004 0010046 0010047 DMOD001004 0.003564
I001005 0010057 0010056 0.000000e+000
D001005 0010056 0010057 DMOD001005 0.000004
I002001 0020017 0020016 0.000000e+000
D002001 0020016 0020017 DMOD002001 0.000259
I002002 0020027 0020026 1.962360e+000
D002002 0020026 0020027 DMOD002002 0.245910
I002003 0020037 0020036 0.000000e+000
D002003 0020036 0020037 DMOD002003 0.000519
I002004 0020047 0020046 1.962360e+000
D002004 0020046 0020047 DMOD002004 0.245910
I002005 0020057 0020056 0.000000e+000
D002005 0020056 0020057 DMOD002005 0.000259
I003001 0030017 0030016 0.000000e+000
D003001 0030016 0030017 DMOD003001 0.000259
I003002 0030027 0030026 1.962360e+000
D003002 0030026 0030027 DMOD003002 0.245910

I003003 0030037 0030036 0.000000e+000
D003003 0030036 0030037 DMOD003003 0.000519
I003004 0030047 0030046 1.962360e+000
D003004 0030046 0030047 DMOD003004 0.245910
I003005 0030057 0030056 0.000000e+000
D003005 0030056 0030057 DMOD003005 0.000259
I004001 0040017 0040016 0.000000e+000
D004001 0040016 0040017 DMOD004001 0.000004
I004002 0040027 0040026 0.000000e+000
D004002 0040026 0040027 DMOD004002 0.003564
I004003 0040037 0040036 0.000000e+000
D004003 0040036 0040037 DMOD004003 0.000008
I004004 0040047 0040046 0.000000e+000
D004004 0040046 0040047 DMOD004004 0.003564
I004005 0040057 0040056 0.000000e+000
D004005 0040056 0040057 DMOD004005 0.000004

% resistors representing the electrical connection of the back contact to ground are inserted in the circuit

R00100212 0010027 0 1.000000e-005
R00100312 0010037 0 1.000000e-005
R00100412 0010047 0 1.000000e-005
R00200212 0020027 0 1.000000e-005
R00200312 0020037 0 1.000000e-005
R00200412 0020047 0 1.000000e-005

% very high value resistors are placed at the edges of the cell in order to avoid floating nodes

Rbar0010014 0010014 0020014 1.0e+005
Rbar0010052 0010052 0020052 1.0e+005
Rbar00100111 00100111 00200111 1.0e+005
Rbar0010059 0010059 0020059 1.0e+005
Rbar0020014 0020014 0030014 1.0e+005
Rbar0020052 0020052 0030052 1.0e+005
Rbar00200111 00200111 00300111 1.0e+005
Rbar0020059 0020059 0030059 1.0e+005
Rbar0030014 0030014 0040014 1.0e+005
Rbar0030052 0030052 0040052 1.0e+005
Rbar00300111 00300111 00400111 1.0e+005
Rbar0030059 0030059 0040059 1.0e+005
Rbar0010011 0010011 0010021 1.0e+005
Rbar0040013 0040013 0040023 1.0e+005
Rbar0010018 0010018 0010028 1.0e+005
Rbar00400110 00400110 00400210 1.0e+005
Rbar0010021 0010021 0010031 1.0e+005
Rbar0040023 0040023 0040033 1.0e+005
Rbar0010028 0010028 0010038 1.0e+005
Rbar00400210 00400210 00400310 1.0e+005
Rbar0010031 0010031 0010041 1.0e+005
Rbar0040033 0040033 0040043 1.0e+005
Rbar0010038 0010038 0010048 1.0e+005
Rbar00400310 00400310 00400410 1.0e+005

Rbar0010041 0010041 0010051 1.0e+005
Rbar0040043 0040043 0040053 1.0e+005
Rbar0010048 0010048 0010058 1.0e+005
Rbar00400410 00400410 00400510 1.0e+005

% resistors called Rbarsource provide connection of the cell to the voltage source: in this case the voltage source has been connected to all the elements at the upper side of the cell

Rbarsource0010011 0010011 999 1.0e-005
Rbarsource0010021 0010021 999 1.0e-005
Rbarsource0010031 0010031 999 1.0e-005
Rbarsource0010041 0010041 999 1.0e-005
Rbarsource0010051 0010051 999 1.0e-005

% the voltage generator (VL) is placed in the circuit

VL 999 0

Resistor models are defined: they include TCR and temperature

.MODEL Rmetal0010011 RES TC1=3.800e-003 T_ABS=46.961061
.MODEL Rmetal0010012 RES TC1=3.800e-003 T_ABS=46.961061
.MODEL Rmetal0010013 RES TC1=3.800e-003 T_ABS=46.961061
.MODEL Rmetal0010014 RES TC1=3.800e-003 T_ABS=46.961061
.MODEL Rcell0010011 RES TC1=5.376e-004 T_ABS=46.961061
.MODEL Rcell0010012 RES TC1=5.376e-004 T_ABS=46.961061
.MODEL Rcell0010013 RES TC1=5.376e-004 T_ABS=46.961061
.MODEL Rcell0010014 RES TC1=5.376e-004 T_ABS=46.961061
.MODEL Rcell0010015 RES TC1=7.211e-003 T_ABS=46.961061
.MODEL Rmetal0010021 RES TC1=3.800e-003 T_ABS=46.979291
.MODEL Rmetal0010022 RES TC1=3.800e-003 T_ABS=46.979291
.MODEL Rmetal0010023 RES TC1=3.800e-003 T_ABS=46.979291
.MODEL Rmetal0010024 RES TC1=3.800e-003 T_ABS=46.979291
.MODEL Rcell0010021 RES TC1=5.376e-004 T_ABS=46.979291
.MODEL Rcell0010022 RES TC1=5.376e-004 T_ABS=46.979291
.MODEL Rcell0010023 RES TC1=5.376e-004 T_ABS=46.979291
.MODEL Rcell0010024 RES TC1=5.376e-004 T_ABS=46.979291
.MODEL Rcell0010025 RES TC1=7.211e-003 T_ABS=46.979291
.MODEL Rmetal0010031 RES TC1=3.800e-003 T_ABS=47.037102
.MODEL Rmetal0010032 RES TC1=3.800e-003 T_ABS=47.037102
.MODEL Rmetal0010033 RES TC1=3.800e-003 T_ABS=47.037102
.MODEL Rmetal0010034 RES TC1=3.800e-003 T_ABS=47.037102
.MODEL Rcell0010031 RES TC1=5.376e-004 T_ABS=47.037102
.MODEL Rcell0010032 RES TC1=5.376e-004 T_ABS=47.037102
.MODEL Rcell0010033 RES TC1=5.376e-004 T_ABS=47.037102
.MODEL Rcell0010034 RES TC1=5.376e-004 T_ABS=47.037102
.MODEL Rcell0010035 RES TC1=7.211e-003 T_ABS=47.037102
.MODEL Rmetal0010041 RES TC1=3.800e-003 T_ABS=47.007414
.MODEL Rmetal0010042 RES TC1=3.800e-003 T_ABS=47.007414
.MODEL Rmetal0010043 RES TC1=3.800e-003 T_ABS=47.007414
.MODEL Rmetal0010044 RES TC1=3.800e-003 T_ABS=47.007414
.MODEL Rcell0010041 RES TC1=5.376e-004 T_ABS=47.007414
.MODEL Rcell0010042 RES TC1=5.376e-004 T_ABS=47.007414

.MODEL Rcell0010043 RES TC1=5.376e-004 T_ABS=47.007414
.MODEL Rcell0010044 RES TC1=5.376e-004 T_ABS=47.007414
.MODEL Rcell0010045 RES TC1=7.211e-003 T_ABS=47.007414
.MODEL Rmetal0010051 RES TC1=3.800e-003 T_ABS=46.966608
.MODEL Rmetal0010052 RES TC1=3.800e-003 T_ABS=46.966608
.MODEL Rmetal0010053 RES TC1=3.800e-003 T_ABS=46.966608
.MODEL Rmetal0010054 RES TC1=3.800e-003 T_ABS=46.966608
.MODEL Rcell0010051 RES TC1=5.376e-004 T_ABS=46.966608
.MODEL Rcell0010052 RES TC1=5.376e-004 T_ABS=46.966608
.MODEL Rcell0010053 RES TC1=5.376e-004 T_ABS=46.966608
.MODEL Rcell0010054 RES TC1=5.376e-004 T_ABS=46.966608
.MODEL Rcell0010055 RES TC1=7.211e-003 T_ABS=46.966608
.MODEL Rmetal0020011 RES TC1=3.800e-003 T_ABS=46.984369
.MODEL Rmetal0020012 RES TC1=3.800e-003 T_ABS=46.984369
.MODEL Rmetal0020013 RES TC1=3.800e-003 T_ABS=46.984369
.MODEL Rmetal0020014 RES TC1=3.800e-003 T_ABS=46.984369
.MODEL Rcell0020011 RES TC1=5.376e-004 T_ABS=46.984369
.MODEL Rcell0020012 RES TC1=5.376e-004 T_ABS=46.984369
.MODEL Rcell0020013 RES TC1=5.376e-004 T_ABS=46.984369
.MODEL Rcell0020014 RES TC1=5.376e-004 T_ABS=46.984369
.MODEL Rcell0020015 RES TC1=7.211e-003 T_ABS=46.984369
.MODEL Rmetal0020021 RES TC1=3.800e-003 T_ABS=47.096783
.MODEL Rmetal0020022 RES TC1=3.800e-003 T_ABS=47.096783
.MODEL Rmetal0020023 RES TC1=3.800e-003 T_ABS=47.096783
.MODEL Rmetal0020024 RES TC1=3.800e-003 T_ABS=47.096783
.MODEL Rcell0020021 RES TC1=5.378e-004 T_ABS=47.096783
.MODEL Rcell0020022 RES TC1=5.378e-004 T_ABS=47.096783
.MODEL Rcell0020023 RES TC1=5.378e-004 T_ABS=47.096783
.MODEL Rcell0020024 RES TC1=5.378e-004 T_ABS=47.096783
.MODEL Rcell0020025 RES TC1=7.209e-003 T_ABS=47.096783
.MODEL Rmetal0020031 RES TC1=3.800e-003 T_ABS=47.330890
.MODEL Rmetal0020032 RES TC1=3.800e-003 T_ABS=47.330890
.MODEL Rmetal0020033 RES TC1=3.800e-003 T_ABS=47.330890
.MODEL Rmetal0020034 RES TC1=3.800e-003 T_ABS=47.330890
.MODEL Rcell0020031 RES TC1=5.382e-004 T_ABS=47.330890
.MODEL Rcell0020032 RES TC1=5.382e-004 T_ABS=47.330890
.MODEL Rcell0020033 RES TC1=5.382e-004 T_ABS=47.330890
.MODEL Rcell0020034 RES TC1=5.382e-004 T_ABS=47.330890
.MODEL Rcell0020035 RES TC1=7.206e-003 T_ABS=47.330890
.MODEL Rmetal0020041 RES TC1=3.800e-003 T_ABS=47.198477
.MODEL Rmetal0020042 RES TC1=3.800e-003 T_ABS=47.198477
.MODEL Rmetal0020043 RES TC1=3.800e-003 T_ABS=47.198477
.MODEL Rmetal0020044 RES TC1=3.800e-003 T_ABS=47.198477
.MODEL Rcell0020041 RES TC1=5.380e-004 T_ABS=47.198477
.MODEL Rcell0020042 RES TC1=5.380e-004 T_ABS=47.198477
.MODEL Rcell0020043 RES TC1=5.380e-004 T_ABS=47.198477
.MODEL Rcell0020044 RES TC1=5.380e-004 T_ABS=47.198477
.MODEL Rcell0020045 RES TC1=7.208e-003 T_ABS=47.198477
.MODEL Rmetal0020051 RES TC1=3.800e-003 T_ABS=46.995021
.MODEL Rmetal0020052 RES TC1=3.800e-003 T_ABS=46.995021
.MODEL Rmetal0020053 RES TC1=3.800e-003 T_ABS=46.995021
.MODEL Rmetal0020054 RES TC1=3.800e-003 T_ABS=46.995021
.MODEL Rcell0020051 RES TC1=5.376e-004 T_ABS=46.995021

.MODEL Rcell0020052 RES TC1=5.376e-004 T_ABS=46.995021
.MODEL Rcell0020053 RES TC1=5.376e-004 T_ABS=46.995021
.MODEL Rcell0020054 RES TC1=5.376e-004 T_ABS=46.995021
.MODEL Rcell0020055 RES TC1=7.211e-003 T_ABS=46.995021
.MODEL Rmetal0030011 RES TC1=3.800e-003 T_ABS=46.962226
.MODEL Rmetal0030012 RES TC1=3.800e-003 T_ABS=46.962226
.MODEL Rmetal0030013 RES TC1=3.800e-003 T_ABS=46.962226
.MODEL Rmetal0030014 RES TC1=3.800e-003 T_ABS=46.962226
.MODEL Rcell0030011 RES TC1=5.376e-004 T_ABS=46.962226
.MODEL Rcell0030012 RES TC1=5.376e-004 T_ABS=46.962226
.MODEL Rcell0030013 RES TC1=5.376e-004 T_ABS=46.962226
.MODEL Rcell0030014 RES TC1=5.376e-004 T_ABS=46.962226
.MODEL Rcell0030015 RES TC1=7.211e-003 T_ABS=46.962226
.MODEL Rmetal0030021 RES TC1=3.800e-003 T_ABS=47.058582
.MODEL Rmetal0030022 RES TC1=3.800e-003 T_ABS=47.058582
.MODEL Rmetal0030023 RES TC1=3.800e-003 T_ABS=47.058582
.MODEL Rmetal0030024 RES TC1=3.800e-003 T_ABS=47.058582
.MODEL Rcell0030021 RES TC1=5.378e-004 T_ABS=47.058582
.MODEL Rcell0030022 RES TC1=5.378e-004 T_ABS=47.058582
.MODEL Rcell0030023 RES TC1=5.378e-004 T_ABS=47.058582
.MODEL Rcell0030024 RES TC1=5.378e-004 T_ABS=47.058582
.MODEL Rcell0030025 RES TC1=7.209e-003 T_ABS=47.058582
.MODEL Rmetal0030031 RES TC1=3.800e-003 T_ABS=47.734874
.MODEL Rmetal0030032 RES TC1=3.800e-003 T_ABS=47.734874
.MODEL Rmetal0030033 RES TC1=3.800e-003 T_ABS=47.734874
.MODEL Rmetal0030034 RES TC1=3.800e-003 T_ABS=47.734874
.MODEL Rcell0030031 RES TC1=5.389e-004 T_ABS=47.734874
.MODEL Rcell0030032 RES TC1=5.389e-004 T_ABS=47.734874
.MODEL Rcell0030033 RES TC1=5.389e-004 T_ABS=47.734874
.MODEL Rcell0030034 RES TC1=5.389e-004 T_ABS=47.734874
.MODEL Rcell0030035 RES TC1=7.201e-003 T_ABS=47.734874
.MODEL Rmetal0030041 RES TC1=3.800e-003 T_ABS=47.355329
.MODEL Rmetal0030042 RES TC1=3.800e-003 T_ABS=47.355329
.MODEL Rmetal0030043 RES TC1=3.800e-003 T_ABS=47.355329
.MODEL Rmetal0030044 RES TC1=3.800e-003 T_ABS=47.355329
.MODEL Rcell0030041 RES TC1=5.384e-004 T_ABS=47.355329
.MODEL Rcell0030042 RES TC1=5.384e-004 T_ABS=47.355329
.MODEL Rcell0030043 RES TC1=5.384e-004 T_ABS=47.355329
.MODEL Rcell0030044 RES TC1=5.384e-004 T_ABS=47.355329
.MODEL Rcell0030045 RES TC1=7.205e-003 T_ABS=47.355329
.MODEL Rmetal0030051 RES TC1=3.800e-003 T_ABS=46.984244
.MODEL Rmetal0030052 RES TC1=3.800e-003 T_ABS=46.984244
.MODEL Rmetal0030053 RES TC1=3.800e-003 T_ABS=46.984244
.MODEL Rmetal0030054 RES TC1=3.800e-003 T_ABS=46.984244
.MODEL Rcell0030051 RES TC1=5.376e-004 T_ABS=46.984244
.MODEL Rcell0030052 RES TC1=5.376e-004 T_ABS=46.984244
.MODEL Rcell0030053 RES TC1=5.376e-004 T_ABS=46.984244
.MODEL Rcell0030054 RES TC1=5.376e-004 T_ABS=46.984244
.MODEL Rcell0030055 RES TC1=7.211e-003 T_ABS=46.984244
.MODEL Rmetal0040011 RES TC1=3.800e-003 T_ABS=46.962923
.MODEL Rmetal0040012 RES TC1=3.800e-003 T_ABS=46.962923
.MODEL Rmetal0040013 RES TC1=3.800e-003 T_ABS=46.962923
.MODEL Rmetal0040014 RES TC1=3.800e-003 T_ABS=46.962923

.MODEL Rcell0040011 RES TC1=5.376e-004 T_ABS=46.962923
.MODEL Rcell0040012 RES TC1=5.376e-004 T_ABS=46.962923
.MODEL Rcell0040013 RES TC1=5.376e-004 T_ABS=46.962923
.MODEL Rcell0040014 RES TC1=5.376e-004 T_ABS=46.962923
.MODEL Rcell0040015 RES TC1=7.211e-003 T_ABS=46.962923
.MODEL Rmetal0040021 RES TC1=3.800e-003 T_ABS=46.983527
.MODEL Rmetal0040022 RES TC1=3.800e-003 T_ABS=46.983527
.MODEL Rmetal0040023 RES TC1=3.800e-003 T_ABS=46.983527
.MODEL Rmetal0040024 RES TC1=3.800e-003 T_ABS=46.983527
.MODEL Rcell0040021 RES TC1=5.376e-004 T_ABS=46.983527
.MODEL Rcell0040022 RES TC1=5.376e-004 T_ABS=46.983527
.MODEL Rcell0040023 RES TC1=5.376e-004 T_ABS=46.983527
.MODEL Rcell0040024 RES TC1=5.376e-004 T_ABS=46.983527
.MODEL Rcell0040025 RES TC1=7.211e-003 T_ABS=46.983527
.MODEL Rmetal0040031 RES TC1=3.800e-003 T_ABS=47.054552
.MODEL Rmetal0040032 RES TC1=3.800e-003 T_ABS=47.054552
.MODEL Rmetal0040033 RES TC1=3.800e-003 T_ABS=47.054552
.MODEL Rmetal0040034 RES TC1=3.800e-003 T_ABS=47.054552
.MODEL Rcell0040031 RES TC1=5.378e-004 T_ABS=47.054552
.MODEL Rcell0040032 RES TC1=5.378e-004 T_ABS=47.054552
.MODEL Rcell0040033 RES TC1=5.378e-004 T_ABS=47.054552
.MODEL Rcell0040034 RES TC1=5.378e-004 T_ABS=47.054552
.MODEL Rcell0040035 RES TC1=7.209e-003 T_ABS=47.054552
.MODEL Rmetal0040041 RES TC1=3.800e-003 T_ABS=47.160167
.MODEL Rmetal0040042 RES TC1=3.800e-003 T_ABS=47.160167
.MODEL Rmetal0040043 RES TC1=3.800e-003 T_ABS=47.160167
.MODEL Rmetal0040044 RES TC1=3.800e-003 T_ABS=47.160167
.MODEL Rcell0040041 RES TC1=5.380e-004 T_ABS=47.160167
.MODEL Rcell0040042 RES TC1=5.380e-004 T_ABS=47.160167
.MODEL Rcell0040043 RES TC1=5.380e-004 T_ABS=47.160167
.MODEL Rcell0040044 RES TC1=5.380e-004 T_ABS=47.160167
.MODEL Rcell0040045 RES TC1=7.208e-003 T_ABS=47.160167
.MODEL Rmetal0040051 RES TC1=3.800e-003 T_ABS=46.956720
.MODEL Rmetal0040052 RES TC1=3.800e-003 T_ABS=46.956720
.MODEL Rmetal0040053 RES TC1=3.800e-003 T_ABS=46.956720
.MODEL Rmetal0040054 RES TC1=3.800e-003 T_ABS=46.956720
.MODEL Rcell0040051 RES TC1=5.376e-004 T_ABS=46.956720
.MODEL Rcell0040052 RES TC1=5.376e-004 T_ABS=46.956720
.MODEL Rcell0040053 RES TC1=5.376e-004 T_ABS=46.956720
.MODEL Rcell0040054 RES TC1=5.376e-004 T_ABS=46.956720
.MODEL Rcell0040055 RES TC1=7.211e-003 T_ABS=46.956720

% diode models are defined: they include inverse saturation current (IS), ideality factor (N) and temperature (T_ABS).

.MODEL DMOD001001 D VJ=0.96 IS=2.128e-008 EG=1.12 N=1.30 (T_ABS=46.961061)
.MODEL DMOD001002 D VJ=0.96 IS=2.128e-008 EG=1.12 N=1.30 (T_ABS=46.979291)
.MODEL DMOD001003 D VJ=0.96 IS=2.128e-008 EG=1.12 N=1.30 (T_ABS=47.037102)
.MODEL DMOD001004 D VJ=0.96 IS=2.128e-008 EG=1.12 N=1.30 (T_ABS=47.007414)
.MODEL DMOD001005 D VJ=0.96 IS=2.128e-008 EG=1.12 N=1.30 (T_ABS=46.966608)
.MODEL DMOD002001 D VJ=0.96 IS=2.128e-008 EG=1.12 N=1.30 (T_ABS=46.984369)
.MODEL DMOD002002 D VJ=0.96 IS=2.128e-008 EG=1.12 N=1.30 (T_ABS=47.096783)
.MODEL DMOD002003 D VJ=0.96 IS=2.128e-008 EG=1.12 N=1.30 (T_ABS=47.330890)

.MODEL DMOD002004 D VJ=0.96 IS=2.128e-008 EG=1.12 N=1.30 (T_ABS=47.198477)
.MODEL DMOD002005 D VJ=0.96 IS=2.128e-008 EG=1.12 N=1.30 (T_ABS=46.995021)
.MODEL DMOD003001 D VJ=0.96 IS=2.128e-008 EG=1.12 N=1.30 (T_ABS=46.962226)
.MODEL DMOD003002 D VJ=0.96 IS=2.128e-008 EG=1.12 N=1.30 (T_ABS=47.058582)
.MODEL DMOD003003 D VJ=0.96 IS=2.128e-008 EG=1.12 N=1.30 (T_ABS=47.734874)
.MODEL DMOD003004 D VJ=0.96 IS=2.128e-008 EG=1.12 N=1.30 (T_ABS=47.355329)
.MODEL DMOD003005 D VJ=0.96 IS=2.128e-008 EG=1.12 N=1.30 (T_ABS=46.984244)
.MODEL DMOD004001 D VJ=0.96 IS=2.128e-008 EG=1.12 N=1.30 (T_ABS=46.962923)
.MODEL DMOD004002 D VJ=0.96 IS=2.128e-008 EG=1.12 N=1.30 (T_ABS=46.983527)
.MODEL DMOD004003 D VJ=0.96 IS=2.128e-008 EG=1.12 N=1.30 (T_ABS=47.054552)
.MODEL DMOD004004 D VJ=0.96 IS=2.128e-008 EG=1.12 N=1.30 (T_ABS=47.160167)
.MODEL DMOD004005 D VJ=0.96 IS=2.128e-008 EG=1.12 N=1.30 (T_ABS=46.956720)

% a DC analysis is performed; a voltage sweep between 0 V and 1 V with a step of 0.02 is realized in order to trace the I-V curve of the cell. Graphical representation of results is enabled through the command .PROBE.

.DC VL 0 1 0.02
.PROBE
.END

A.3 FUNCTION CREA_MASCHERA

A further function has been created in order to extract voltage map of the cell surface at maximum power point from simulation output data.

Here is reported the code of the function, with comments in green.

```
%the function uses as input parameter an output PSPICE file containing
%output power values and voltage values in the emitter points for all
%values of external voltage generator VL.
function [mappa,massimo]=mappa_tensioni_comb(filename,M,P)
fid =fopen(filename,'r');
matrix=[];
%the file is read row by row
line=fgets(fid);
while line ~=-1
    matrix=[matrix;str2num(line)];
    line=fgets(fid);
end
potenza=matrix(:,2);
%voltage value corresponding to the maximum power is found
[massimo,posmax]=max(potenza);
%voltage values in the nodes 5 corresponding to the maximumm power point
%are placed in the vector vettore
```

```
vettore=matrix(posmax,3:end);
%voltage map mappa is then constructed
for i=1:M,
mappa(i,1:P)=vettore(P*(i-1)+1:P*i);
end
imagesc(mappa);
colorbar;
axis equal;
```

REFERENCES

1. L. Fraas, L. *Partain, Solar Cells and their Applications,* John Wiley & Sons
2. V. M. Andreev, V. A. Grilikhes, V. D. Rumyantsev *Photovoltaic Conversion of Concentrated Sunlight*, John Wiley & Sons
3. A. Salim and N. Eugenio . *Solar Cells* 29 , 1 (1990)
4. M. O ' Neill . Chapter 10. In *Solar Cells and Their Applications* , L. D. Partain , ed., 1st edition . New York, John Wiley & Sons (1995)
5. M. Klausmeier - Brown . Chapter 5. In *Solar Cells and Their Applications* , L. D. Partain, ed., 1st edition . New York, John Wiley & Sons (1995)
6. L. W. James and J. K. Williams . Fresnel optics for solar concentration on photovoltaic cells . In *13th IEEE Photovoltaic Specialists Conference* , Washington, DC, pp. 673 – 679 . New York, IEEE (1978)
7. A. Luque . *Solar Cells and Optics for Photovoltaic Concentration* . Bristol, England, IOP Publishing. International Standard Book Number 0 - 85274 - 106 - 5 (1989)
8. A. Heller , P. Nitz , and W. Platzer . Indoor characterization of Fresnel - type concentrator lenses . In *Proceedings of the 4th International Conference on Solar Concentrators for the Generation of Electricity or Hydrogen* , El Escorial, Spain , G. Sala , R. D. McConnel , and R. R. King , eds., pp. 289 – 293 (2007)
9. D. E. Arvizu . Development of the Sandia 200X experimental silicon module . In *13th IEEE Photovoltaic Specialists Conference* , Orlando , FL , pp. 805 – 813 . New York, IEEE (1984)
10. J. Jaus , P. Nitz , G. Peharz , G. Siefer , T. Schult , O. Wolf , M. Passig , T. Gandy , and A. W. Bett . Second stage refl ective and refractive optics for concentrator photovoltaics. In *Proceedings of the 33rd IEEE PVSC* , San Diego, CA , New York, IEEE (2008)
11. A. Neumann , A. Witzke , S. A. Jones , and G. Schmitt . Representative terrestrial solar brightness profi les . *J. Sol. Energy Eng.* **124** , 198 – 204 (2002)
12. W. T. Welford and R. Winston . *The Optics of Nonimaging Concentrators Light and Solar Energy* . San Diego, CA , Academic (1978)
13. N. R. Kaminar and H. C. Hamaker . 19% concentrator module effi ciency using single - junction GaAs cells . In *Proceedings of the 18th IEEE Photovoltaic Specialists Conference* , pp. 1559 – 1561 . New York, IEEE (1985)
14. H. F. MacMillan , H. C. Hamaker , N. R. Kaminar , M. S. Kuryla , M. L. Ristow , D. D. Liu , G. F. Virshup , and J. M. Gee . 28% effi cient GaAs concentrator solar cells. In *Proceedings of*

the 20th IEEE Photovoltaic Specialists Conference , Las Vegas, NV , pp. 462 – 468 . New York, IEEE (1988)

15. M. S. Kuryla , M. L. Ristow , L. D. Partain , and J. E. Bigger . 22.3% effi cient 12 cell 1000 sun GaAs concentrator module In *Proceedings of the 22nd IEEE Photovoltaic Specialists Conference* , Las Vegas, NV , pp. 506 – 511. New York, IEEE (1991)
16. G. S. Kinsey , R. A. Sherif , H. L. Cotal , P. Pien , R. R. King , R. J. Brandt , W. G. Wise , E. L. Labios , K. F. Wan , M. Haddad , J. M. Lacey , C. M. Fetzer , P. Verlinden, J. Lasich , and N. H. Karam . Multijunction solar cells for dense - array concentrators. *Proc. of the IEEE 4th World Conf. on Photovoltaic Energy Conversion Vol. 1,* Waikoloa, HI, May 7 – 12 , pp. 625 – 627 (2006).
17. L. M. Fraas , J. E. Avery , H. X. Huang , E. Shifman , K. Edmondson , and R. R. King. Toward 40% and higher multijunction cells in a new Cassegrainian PV Module . *Conference Record of the 31st IEEE Photovoltaics Specialists Conference.* Lake Buena Vista, FL, January 3 – 7 , pp. 751 – 753 (2005).
18. L. Fraas , J. Avery , H. Huang , L. Minkin , and E. Shifman . Demonstration of a 33% effi cient Cassegranian solar module . In *Proc. of the IEEE 4th World Conf. On Photovoltaic Energy Conversion, Vol. 1* , Waikoloa, HI, May 7 – 12 , pp. 679 – 682 (2006)
19. C. H. Henry, *Limiting Efficiency of Ideal Single and Multiple Energy Gap Terrestrial Solar Cells*, J. Appl. Phys. 51, 4494-4500, (1980)
20. W. Shockley, H. J. Queisser, *Detailed Balance Limit of Efficiency of p-n Junction Solar Cells*, J. Appl. Phys. 32, 510-519, (1961)
21. A. M. Vasil'ev, A. P. Landsman, Poluprovodnikovye Fotopreobrazovateli (Semiconductor Photoconverters), Sov. Radio, Moscow, 1971 (in Russian)
22. Kh. K. Aripov, V. D. Rumyantsev, *Laws Governing the Formation of Current-Voltage Characteristics of Solar Cell with Distributed Parameters*, Fiz. i Tekhn. Polupr., 17, 358-361, 1983, Translated into English in Sov. Phys. Semicond. 17, No. 2, 1983
23. A. De Vos, *The Distributed Series Resistance Problem in Solar Cells*, Solar Cells, 12, 311-327, 1984
24. A. De Vos, P. De Visschere, *Diagnosis of a large Distributed Series Resistance in Solar Cells*, Solar Cells, 10, 69-80, 1983
25. Kh. K. Aripov, V. D. Rumyantsev, *Solar Cells with Distributed Parameters:Current-Voltage Characteristics Under Uniform and non-Uniform Illumination*, Geliotekhnica No. 4, 6-10, 1983, Translated into English in Applied Solar Energy, No. 4, 1983

26. Kh. K. Aripov, V. D. Rumyantsev, *Solar Cells with Distributed Parameters: Photovoltaic Conversion Efficiency*, Geliotekhnica No. 5, 3-6, 1983, Translated into English in Applied Solar Energy, No. 5, 1983

27. Kh. K. Aripov, V. D. Rumyantsev, L. Hernandez, *An Account of Distributed Nature of Front Layer and Contact Grid Resistances at Calculation of Solar Cell Current-Voltage Characteristics*, Geliotekhnica No. 5, 3-6, 1986, Translated into English in Applied Solar Energy, No. 5, 1986

28. V. D. Rumyantsev, J. A. Rodriguez, *Method of Calculating the Distributed and Lumped Components of the Resistance in Solar Cells*, Solar Cells, 28, 241-252, 1990

29. Zh. I. Alferov, Kh. K. Aripov, B. V. Egorov, V. R. Larionov, V. D. Rumyantsev, O. M. Fedorova, L. Hernandez, Investigations of Heterophotocells with Intermediate Conversion of Radiation at High Level of Illumination, Fiz. i Tekhn. Polupr., 14, 685-690, 1980, Translated into English in Sov. Phys. Semicond. 14, No. 4, 1980

30. A. K. Alimov, A. I. Kulagin, N. K. Kivalov, G. Ya. Umarov, V. D. Rumyantsev, L. M. Goldstein, E. A. Guner, V. I. Solove'chik, N. V. Makov, *Investigations of Parabola-Toroidal Profiled Solar Concentrators for High-Current Heterophotocells*, Geliotekhnica, No. 3, 33-35, 1984, Translated into English in Applied Solar Energy, No. 3, 1984

31. R. J. Overstraeten, R. P. Mertens, Heavy Doping Effects in Silicon, Solid-State-Electronics, Vol. 30, No. 11, pp. 1077-1087, 1987

32. J. G. Fossum, D. Lee, Solid-State-Electronics

33. G. D. Mahan, J. Appl.Phys., 51, 2634 (1980)

34. E. O. Kane, Phys. Rev., 131, 79 (1963)

35. J. W. Slotboom, H. C. de Graaf, Measurement of Bandgap Narrowing in Si Bipolar Transistors, Solid-State-Electronics, 19, 857-862, (1976)

36. M. A. Shibib, F. A. Lindholm, F. Therez, *Heavily Doped Transparent-Emitter Regions in Junction Solar Cells, Diodes and Transistors*, IEEE Trans. El. Dev., Vol. 26, No. 6, (1979)

37. P. T. Landsberg, R. W. Mackay, A. D. McRonald, *The Parameters of Simple Excess Semiconductors*, Proc. Phys. Soc. A, p. 476, 1950

38. J. R. Hauser, Final Rep. on NSF Grant GK-1615, 1969

39. H. P. D. Lanyon, R. A. Tuft, unpublished work

40. C. S. Fuller, *Semiconductors*, Academic New York, (1975)

41. J. G. Fossum, D. S. Lee, 15th PVSC Conf. (1981)

42. P. C. Dhanasekaran, B. S. V. Gopalam, *The Physical Behaviour of an $n^+ p$ Silicon Solar Cell in Concentrated Sunlight, Solid-State-Electronics*, Vol. 25, No. 8, 719-722, 1982

43. H. K. Gummel, IEEE Trans. Electron. Dev., ED-11, 455 (1964)

44. A. De Mari, Solid-State-Electronics, 11, 33 (1968)

45. F. A. Lindholm, C.-T. Sah, *Fundamental Electronics Mechanisms Limiting the Performance of Solar Cells*, IEEE Trans. Electron. Dev., Vol. ED-24, No. 4, 1977

46. C.-T. Sah F. A. Lindholm, Carrier Generation, *Recombination, Trapping, and Transport in Semiconductors with Position-Dependent Composition*, IEEE Trans. Electron. Dev., Vol. ED-24, No. 4, 1977

47. D. M. Spederna, D. H. Navon, *Solar-Cell Operation Under Concentrated Illumination*, IEEE Trans. Electron. Dev., Vol. ED-25, No. 11, 1290, (1978)

48. J. G. Fossum, *Computer-Aided Numerical Analysis of Silicon Solar Cells*, Solid-State-Electronics, Vol. 19, 269-277, (1976)

49. J. G. Fossum, E. L. Burgees, F. A. Lindholm, *Silicon Solar Cell Designs Based on Physical Behavior in Concentrated Sunlight*, Solid-State-Electronics, Vol. 21, 729-737 (1978)

50. P. Norton, J. Brandt, *Temperature Coefficient of Resistance for p-type and n-type Silicon*, Solid-State-Electronics, Vol. 21, 969-974, 1978

51. S. E. Foss, B. R. Olaisen, E. S. Marstein, A. Holt, *A New 2.5D Distributed Spice Model of Solar Cells*, Proceedings of the 21th European Photovoltaic Solar Energy Conference, Dresden, Germany, 430-434, (2006)

52. B. Galiana, C. Algora, I. Rey-Stolle, I. Garcia Vara, *A 3-D Model for Concentrator Solar Cells based on Distributed Circuit Units*, IEEE Trans. Electron. Dev., Vol. 52, No. 12, 2005

53. A. Zekry, A. Y. Al-Mazroo, *A Distributed SPICE-Model of a Solar Cell*, IEEE Trans. Electron. Dev., Vol.43, No. 5, 1996

54. A. Antonini, *Contatti a Geometria Frattale su Celle Fotovoltaiche per l'Ottimizzazione delle Perdite Ohmiche,* Graduation Thesis

55. D. Vincenzi, M. Stefancich, S. Baricordi, M. Pasquini, F. Gualdi, G. Martinelli, A. Parretta, A. Antonini, Effects of Irradiance Distribution Unevenness on the Ohmic Losses of CPV Receivers, Proceeding of the 24th EUPVSEC, Hamburg, 2009

56. D. Buie, A.G. Monger, C.J. Dey, Solar Energy 74 (2003) 113–122.

57. M. Minnaert, *The Photosphere* in: *The Solar System,* Kuiper, G.P. (Ed.), University of Chicago Press (1962)

58. G. Johnston, Solar Energy 63 (2) 1998, 117–124

59. M.A. Green, *Silicon solar cells – operating principles, technology and system applications*, Prentice-Hall, Englewood, Cliffs (NY) 1982

60. A. Bhakta, S. Bandyopadhyay, *Constructal Optimization of Top Contact Metallization of a Photovoltaic Solar cell*, Int. J. of Tthermodynamics, Vol. 8, No. 4, 175-181, 2005

61. Devoney, *A first course in chaotic dynamical systems*, Addison Wesley

62. A. Bunde, S. Havlin, *Fractal and Disordered Systems*, Springer-Verlag
63. V. Balakrishanan, *Random Walks on Fractals*, Materials Science and Engineering, B32, 201-210 (1995)
64. M. Pasquini, D. Vincenzi, S. Baricordi, F. Gualdi, C. Malagù, A. Parretta, L. Pozzetti, *Analysis of Non-Conventional front Contact Patterns Impact on Concentrator Solar Cells Performances Through a 2.5-D Distributed Electrical Model*, Proceedings of the 26th EUPVSEC, Hamburg, 2011
65. A. S. Fleischer, Li-hsin Chang, B. Johnson, *The Effect of Die Attach Voiding on the Thermal resistance of Chip Level Packages*, Microelectronics Reliability, 46, 794-804, (2006)
66. L. Ciampolini, M. Ciappa, P. Malberti, P. Regli, W. Fichtner, *Modelling Thermal Effects of Large Contiguous Voids in Solder Joints*, Microelectronics Journal, 30, 1115-1123 (1999)
67. D. C. Katsis, *Thermal Characterization of Die-Attach Degradation in the Power MOSFET*, PhD Thesis